

# Analyzing Hydrodynamic Properties of the North Atlantic Right Whales with Computer Solutions

by

Chen-Yi Wu

Marine Science and Conservation

Duke University

Date: \_\_\_\_\_  
Approved: \_\_\_\_\_

\_\_\_\_\_  
Douglas P. Nowacek, Advisor

\_\_\_\_\_  
Laurens E. Howle

\_\_\_\_\_  
Frank E. Fish

\_\_\_\_\_  
Brian P. Mann

\_\_\_\_\_  
Julie M. van der Hoop

Dissertation submitted in partial fulfillment of the requirements for the degree of Doctor of Philosophy in Marine Science and Conservation of Duke University

2020

ABSTRACT

Analyzing Hydrodynamic Properties of the North  
Atlantic Right Whales with Computer Solutions

by

Chen-Yi Wu

Marine Science and Conservation

Duke University

Date: \_\_\_\_\_

Approved: \_\_\_\_\_

\_\_\_\_\_  
Douglas P. Nowacek, Advisor

\_\_\_\_\_  
Laurens E. Howle

\_\_\_\_\_  
Frank E. Fish

\_\_\_\_\_  
Brian P. Mann

\_\_\_\_\_  
Julie M. van der Hoop

An abstract of a dissertation submitted in partial fulfillment of the requirements for the  
degree of Doctor of Philosophy in Marine Science and Conservation of Duke University

2020

Copyright © 2020 by Chen-Yi Wu  
All rights reserved except the rights granted by the  
Creative Commons Attribution-Noncommercial License

## **Abstract**

Animals experience hydrodynamic forces (lift, drag, and side) and moments (pitching, yawing, and rolling) as a result of motion in an aqueous medium. Under selective pressure, most cetaceans, including porpoises, dolphins, and whales, developed a streamlined body shape and modified limbs, which delay the separation of flow, create lower drag when they swim, and therefore decrease their locomotor cost. In order to calculate the locomotor cost and propulsive efficiency of cetaceans, accurate estimates of drag on marine animals are required. However, extra momentum imparted into the fluid from lift and side forces as well as pitching, rolling, and yawing moments (here, the parasitic loads) results in extra drag force on the animal. Therefore, in addition to streamlining and delaying flow separation, animals must also minimize excess fluid momentum resulting from parasitic loads.

Given the endangered status of the North Atlantic right whale (*Eubalaena glacialis*; hereafter NARW), analyzing the hydrodynamic characteristics of the NARWs was the focus of this work. Additionally, previous studies showed that body shape of NARWs changes with life stages, reproduction status, nutritive conditions or prey abundance, and the effects of entanglement in fishing gear. Therefore, in this study, computational fluid dynamics (CFD) analysis was performed on multiple 10 m three-dimensional NARW models with different body shapes (e.g., normal condition, emaciated, and pregnant) to measure baseline

measurements of flow regimes and hydrodynamic loads on the animal. Swimming speeds covering known right whale speed range (0.125 m/s to 8 m/s) were simulated in most scenarios. In addition to the hydrodynamic effects of different body shapes, drag was also considered a function of parasitic loads. The NARW models were embedded with bone segments that allowed one to manipulate the body pose of the model via adjusting the flippers or the spine of the animal before measuring hydrodynamic drag. By doing so, momentum from parasitic loads was expected to be eliminated.

CFD simulations revealed that drag on NARWs is dictated by its irregular outline and that the drag coefficient (0.0071-0.0059; or dimensionless drag) of on NARWs is approximately twice that of many previous estimates for large cetaceans. It was also found that pregnant NARW model encounters the lowest drag coefficient due to delayed flow separation resulting from enlarged abdomen, whereas the emaciated NARW model experiences the highest drag coefficient possibly due to the concavity at the post-nuchal region. These results suggested that drag on NARWs and their thrust power requirements were indeed affected by its body shape but the differences between the three NARW models tested were small. Lastly, minimum drag, which corresponds to the elimination of the parasitic loads, can be obtained by adjusting the pose of the animal. Thus, minimum drag occurs at the neutral trim pose. For the static, normo-nourished NARW model, simulations revealed that by changing the angle of attack of the flippers by  $4.03^\circ$

(relative to the free-stream flow) and pitching the spine downward by  $5^\circ$  while maintaining fluke angle, the drag was lowered by approximately 11% across the flow speeds tested. This drag reduction was relative to the drag study conducted on the same animal model but without body pose adjustments.

Together the studies included in the present work explored and highlighted the capability of numerical methods in investigating the hydrodynamics and energetics of cetaceans. Future studies should address how computer solutions can be used to solve problems from a wider aspect. For instance, extra parasitic loads caused by attached gear as well as possible injuries due to the encounter with fishing gear should also be considered while evaluating the energy budget of the North Atlantic right whales.

KEYWORDS: computational fluid dynamics; energetics; *Eubalaena glacialis*; hydrodynamic efficiency; hydrodynamics; morphology; North Atlantic right whale; trim drag

To my family in Taiwan and my feline companion Winston

# Contents

Abstract .....	iv
List of Tables .....	xii
List of Figures.....	xiii
Acknowledgements .....	xv
Chapter 1 Introduction.....	1
1.1 The physics of underwater movement .....	1
1.1.1 Hydrodynamics .....	1
1.1.2 Energetic costs .....	1
1.2 Species background.....	2
1.2.1 The North Atlantic right whale.....	2
1.2.2 Anthropogenic disturbances and conservation .....	7
1.3 Energetics of the North Atlantic right whales .....	8
1.3.1 Foraging behavior of baleen whales .....	8
1.3.2 Energy budget of world’s largest predators .....	10
1.3.3 Applications of computational modeling.....	11
1.4 Dissertation overview.....	12
Chapter 2 Computational fluid dynamics of flow regimes and hydrodynamic forces generated by a gliding North Atlantic right whale ( <i>Eubalaena glacialis</i> ) .	13
2.1 Introduction .....	13
2.2 Methods .....	16
2.2.1 Three-dimensional right whale model.....	17
2.2.2 Hydrodynamic parameters.....	19

2.2.3 Numerical model .....	20
2.3 Results.....	22
2.3.1 CFD model performance .....	23
2.3.2 Fluid velocity and Reynolds number .....	23
2.3.3 Boundary layer thickness and type.....	26
2.3.4 Shear stress, drag, and pressure.....	27
2.4 Discussion.....	31
2.4.1 Body length, surface area, and enclosed volume for $Re$ and $C_D$ .....	32
2.4.2 Hydrodynamic performance of the NARW.....	33
2.4.3 Whale drag predictions.....	34
2.4.4 Limitations of drag estimation .....	39
2.5 Conclusion .....	40
Chapter 3 Computational fluid dynamic analysis of gliding North Atlantic right whale models with variable body shapes.....	41
3.1 Introduction .....	41
3.2 Methods .....	44
3.2.1 Three-dimensional NARW models .....	44
3.2.2 Hydrodynamic parameters.....	48
3.2.3 Energetic costs for NARW from hydrodynamic models.....	50
3.2.4 Numerical model .....	51
3.3 Results.....	52
3.3.1 Reynolds number and drag.....	52
3.3.2 Boundary layer thickness and type.....	53

3.3.3 Shear stress, drag, and total pressure .....	57
3.3.4 Locomotor cost of gliding NARWs .....	59
3.4 Discussion .....	62
3.4.1 Hydrodynamic performance of the three NARW models .....	62
3.4.2 Cost of locomotion of gliding NARWs.....	63
3.4.3 Physiological recover of NARWs .....	65
3.5 Conclusion .....	66
Chapter 4 Minimal drag on a three-dimensional North Atlantic right whale model via neutral trim pose .....	68
4.1 Introduction .....	68
4.2 Methods .....	72
4.2.1 Three-dimensional NARW model .....	72
4.2.2 Hydrodynamic properties.....	72
4.2.3 Animal model adjustments.....	77
4.2.4 Numerical model .....	80
4.3 Results.....	80
4.3.1 Adaptive animal body pose adjustments .....	81
4.3.2 Lift provided by the NARW model .....	81
4.3.3 Hydrodynamic drag on the NARW model .....	82
4.3.4 Pitching moment of the animal .....	83
4.3.5 Hydrodynamic efficiency of the NARW model .....	88
4.3.6 Neutral trim pose of the NARW model .....	88
4.4 Discussion.....	94

4.4.1 Lift, drag and pitching moment on the NARW model .....	94
4.4.2 Hydrodynamic efficiency of different body poses.....	95
4.4.3 Neutral trim pose of the NARW model .....	96
4.5 Conclusion .....	98
Chapter 5 Conclusion .....	100
Appendix .....	103
References .....	109
Biography .....	122

## List of Tables

Table 2.1 Drag coefficients across species from current and previous studies. ....	38
Table 3.1 Morphometric measurements of three NARW models tested. ....	50
Table 3.2 CFD simulation results in half and full domains.....	54
Table 3.3 Locomotor power requirements of gliding NARWs.....	60
Table 3.4 Results of Spearman correlation test.....	60
Table 4.1 NARW model position setup.....	76
Table 4.2 NARW model position setup for Scenario 4: minimal drag pose simulations.....	89
Table 4.3 Changes of hydrodynamic forces and moment across speeds. ....	90
Table 4.4 Body pose adjustments associated with minimal pitching moment.....	98

## List of Figures

Figure 1.1 A pair of North Atlantic right whale.....	5
Figure 1.2 Right whale habitats. ....	6
Figure 1.3 An entangled North Atlantic right whale.....	8
Figure 2.1 The three-dimensional NARW model. ....	18
Figure 2.2 Boundary layer type simulated in half domain. ....	22
Figure 2.3 Particle pathlines on the flipper and the fluke of the NARW model. ...	24
Figure 2.4 Drag and drag coefficient as a function of Reynolds number.....	25
Figure 2.5 Fluid velocity on the medial plane of the NARW model.....	26
Figure 2.6 Boundary layer thickness and type. ....	29
Figure 2.7 Shear stress and form drag on the NARW model. ....	30
Figure 2.8 Pressure gradient on the NARW model.....	31
Figure 2.9 Drag coefficients across species from current and previous studies as a function of Reynolds number. ....	37
Figure 3.1 Lateral view of the North Atlantic right whale models. ....	46
Figure 3.2 Constructing NARW models with different body shapes. ....	47
Figure 3.3 Drag and drag coefficient as a function of Reynolds number.....	55
Figure 3.4 Boundary layer thickness and type. ....	56
Figure 3.5 Shear stress, form drag, and total pressure on three models. ....	58
Figure 3.6 Thrust power requirement of NARWs with different body shapes. ....	61
Figure 4.1 Three-dimensional NARW model. ....	75
Figure 4.2 Animal pose adjustments. ....	78
Figure 4.3 Lift coefficient associated with modified animal body pose. ....	84

Figure 4.4 Drag coefficient associated with modified animal body pose.....	85
Figure 4.5 Pitching moment coefficient associated with modified animal body pose.....	86
Figure 4.6 Hydrodynamic efficiency of the model associated with modified animal body pose.....	87
Figure 4.7 Comparison between lift from previous work and current study.....	91
Figure 4.8 Comparison between drag from previous work and current study.....	92
Figure 4.9 Comparison between pitching moment from previous work and current study. ....	93
Figure 4.10 Differences in hydrodynamic efficiency between pre- and post-adjusted animal body position.....	94

## **Acknowledgements**

There are numerous people that I would like to thank for supporting me from the beginning toward the completion of my doctoral degree at Duke University Marine Lab.

First and most important of all, this inter-disciplinary study would not be carried out without the inspirations and support provided by my co-advisors Doug and Lars. Without them I would not be able to apply my background knowledge in the fields of engineering and biology to resolve marine conservation issues faced by the North Atlantic right whale. I am also grateful that Drs. Frank Fish, Brian Mann, and Julie van der Hoop agreed to serve on my dissertation committee, advised and evaluated my research, and guided me along the path.

Secondly, I have been receiving valuable feedback outside of Duke: from Drs. Scott Kraus, Will McLellan, Alex Werth, Jean Potvin, as well as Tim Werner, Heather Pettis, and many others, all of them generously shared their knowledge on right whales, entanglements, or fluid dynamics with me.

In addition to my own projects, my graduate school experience has been undoubtedly flourished by people who I have met during the time I spent at Duke. Duke Marine Lab has an amazing marine mammal research group: Superpod. Although members came from various fields and have diverse research subjects, through journal clubs, scientific conferences, fieldwork, and outreach activities, I am impressed and thrilled to see how we can make our voice heard and our science

available to a broader audience outside of academia. Among these people, I would like to shout out to Jillian Wisse, my cohort and counterpart since the first day of my graduate study. I am thankful for her consolation when I felt overwhelmed by the workload and her encouragement on my every achievement. I want to mention that Rachal Lo Piccolo is the most reliable person at Duke Marine Lab who takes care of all of us Ph.D. students and solves our problems whether they are work-related or not. I am also fortunate to work with or be helped by Rebecca Smith, Janil Miller, Liz DeMattia, and many others from the Duke Marine Lab Community.

To be honest, being an international student is hard in many ways, such as language, living in a foreign country, and the fact that I am thousands of miles away from home. However, with (mostly mental) support from my family and friends in Taiwan, as well as some Taiwanese students I met here at Duke, I was able to overcome loneliness and other difficulties and enjoy my life in the United States. Therefore, my last thanks are given to everyone who has pushed me toward achieving my goal of becoming a marine scientist.

# **Chapter 1 Introduction**

## ***1.1 The physics of underwater movement***

### **1.1.1 Hydrodynamics**

When an object travels through fluid, resistance is created by physical forces, such as a force exerted upwards known as lift and a force exerted against the direction of the object, known as drag (Webb 1975, Vogel 1994, Munson et al. 2010). Therefore, under selective pressure, the ancestors of modern cetaceans developed streamlined body shapes and transformed limbs to successfully return to aquatic environments (Gingerich et al. 1990, Uhen 2010). Their morphology delays separation of boundary layer and reduces drag while swimming (Fish 1993a, Vogel 1994, Goldbogen et al. 2006, Woodward et al. 2006a). To move forward, cetaceans and fish produce thrust with undulatory body movement (Lighthill 1969, Fish 1993a, Triantafyllou et al. 1993), suggesting that they use lift-based system to propel and compensate drag (Vogel 1994, Fish 1996). Additionally, observations at sea and locomotive data recorded by animal-borne tags indicate that cetaceans may adjust their behaviors to lower the energetic cost for swimming (Williams et al. 1992b, Nowacek et al. 2001, Miller et al. 2004, Goldbogen et al. 2006, Nousek-McGregor et al. 2014, van der Hoop et al. 2014a, Williams and Maresh 2015).

### **1.1.2 Energetic costs**

The total cost of transport (COT) is used to estimate the energetic expenditure of aquatic animals, which is sum of the maintenance cost, the rate of

oxygen consumed by the animal, and the locomotor cost, i.e., the energy cost for swimming (Fish 1993a, Williams 1999, Williams and Maresh 2015). Here, the COT is defined as the metabolic cost to move a body mass a given distance (J/kg/m) (Tucker 1975). Hence, optimal swimming efficiency can be associated with metabolic rate and drag of the animal (Miller et al. 2004). While direct measurements of metabolic cost of large cetaceans are difficult to obtain (Williams and Maresh 2015), the cost of locomotion and resistant drag in large marine mammals can be estimated with field observations and computer models (Miller et al. 2004, Goldbogen et al. 2007, Williams and Noren 2009, Nousek-McGregor 2010, Goldbogen et al. 2012, van der Hoop et al. 2017c).

## ***1.2 Species background***

### **1.2.1 The North Atlantic right whale**

The North Atlantic right whale (*Eubalaena glacialis*, Müller 1776, Figure 1.1; here after NARW) is a member of Family Balaenidae, which consists of three right whale species: North Atlantic right whale, North Pacific right whale (*E. japonica*), Southern right whale (*E. australis*), and bowhead whale (*Balaena mysticetus*). NARWs can grow up to approximately 14-15 m in length and up to 70 tons in weight. The NARW has a highly arched jawline, a narrow upper jaw, and a massive head which can be up to one-third of its body length (Kraus and Rolland 2007). Like other baleen whales, the NARW has long, elastic baleen plates growing down from its upper jaw, which allow it to capture food while it skims through the water surface or deep in the water column with mouth opened (Watkins and

Schevill 1976, Baumgartner and Mate 2003). Most NARWs are black with some white areas on the belly and chin, they have patches of roughened skin on their head, called “callosities”, that are commonly occupied by cyamid crustaceans (whale lice) and are usually yellow or white in color (Kraus and Rolland 2007). The individually distinctive patterns of callosities make it possible for scientists to identify individual whales throughout their lifespan, which can be up to 70 years (Kraus and Rolland 2007, Jefferson et al. 2008).

NARWs gather in their summer feeding grounds, including U.S. waters off New York and New England, Great South Channel, and in Canadian waters of the Bay of Fundy, Scotia Shelf, Roseway Basin, and as north as Gulf of St. Lawrence (Figure 1.2, image courtesy of the New England Aquarium). They forage on planktonic copepod (primarily *Calanus finmarchicus*), their primary food (Kenney et al. 1986, Mayo and Marx 1990, Clapham et al. 1999, Baumgartner and Mate 2003, Baumgartner et al. 2007). In winter, pregnant females travel to calving grounds in the coastal waters of southeastern United States (SEUS), including the waters off Georgia and Florida though as far north as N. Carolina, to give birth and raise their calves. The distribution of other demographic groups in winter is still unknown (Kraus and Rolland 2007, Jefferson et al. 2008, Waring et al. 2016, Davis et al. 2017, NMFS 2017). In recent years, changes in habitat use and animal distribution have been observed and led to a decrease in observation rate in their previously known habitats (Pettis et al. 2017a). For example, fewer individuals

have been detected in the Bay of Fundy and the Great South Channel, regions that used to be occupied by larger groups in summer (Waring et al. 2016).

Historically, NARWs were considered the ‘right’ whales to hunt by whalers because they have rich oil (blubber), they swim slowly and close to shore, and they were more likely than other species of whales to float after being killed (Reeves and Mitchell 1986a, b). Unsurprisingly, NARWs were nearly extinct due to commercial whaling in the nineteenth and early twentieth centuries (Kraus et al. 2005). NARW whaling can be dated back to the eleventh century in Basque, then American waters, Canadian waters, and Azores (Clapham et al. 1999, Reeves et al. 2007). With the invention of more efficient tools and whaling ships, right whaling was expanded from near-shore to the open ocean. Ultimately, it became a commercial ‘fishery’. Reeves et al. (2007) estimated 5500 NARWs were taken from the western North Atlantic between 1934 and 1951 based on written documents. However, the authors noted that this number is certainly underestimated and the pre-exploitation population size for NARWs is still unknown. The population size might have been as low as 100 individuals when the take of NARWs was banned in 1935 (Waring et al. 2016). NARW is currently one of the most endangered large whale species in the world. Even though the NARW population has recovered to approximately 409 individuals in past decades under international protection (Pettis et al. 2020), its growth rate has been considered to be in decline since 1980 (Caswell et al. 1999, Pace et al. 2017).



Figure 1.1 A pair of North Atlantic right whale. Photo courtesy of New England Aquarium, taken under NOAA Research Permit #655-1652-01.

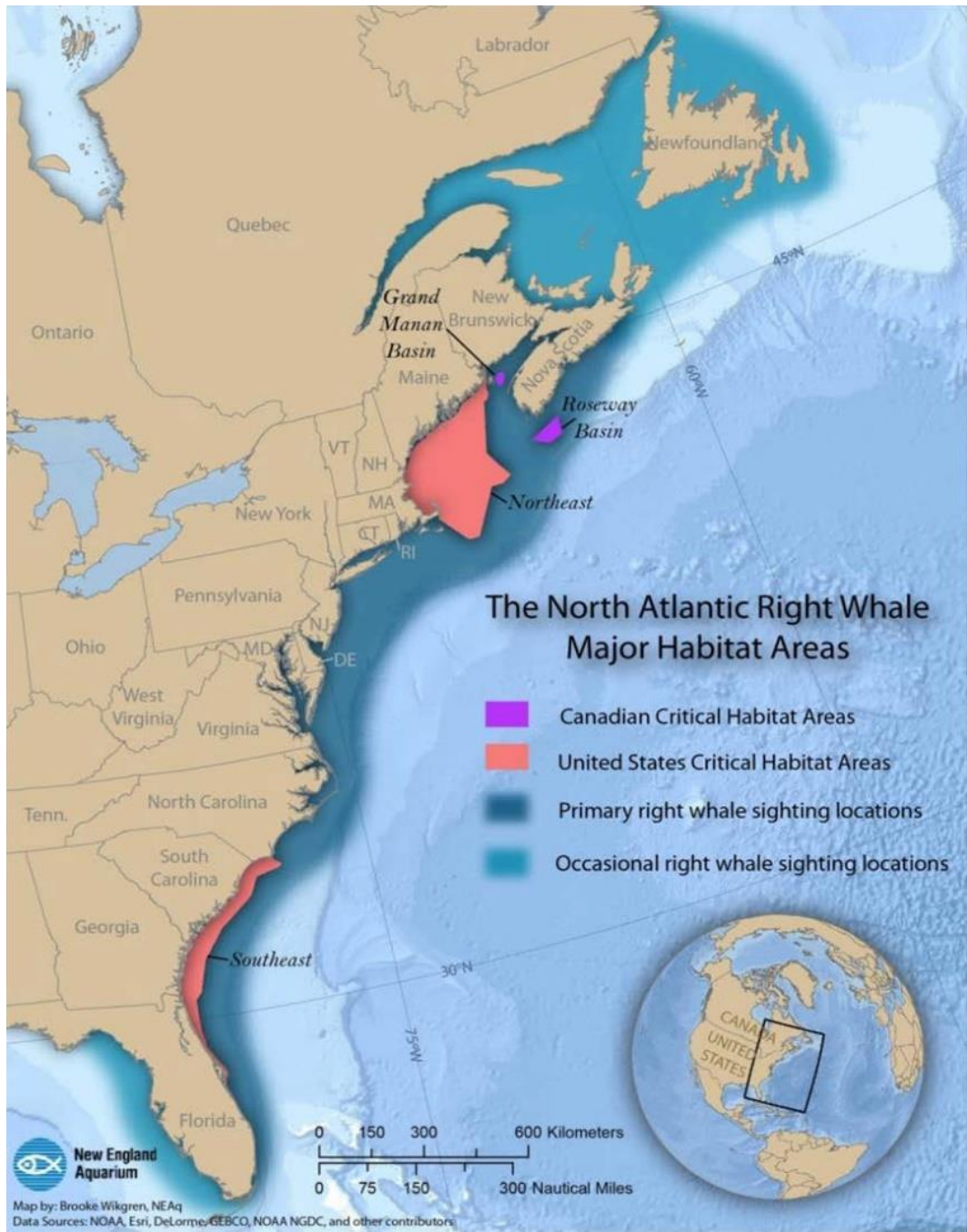


Figure 1.2 Right whale habitats. Image courtesy of the New England Aquarium.

### **1.2.2 Anthropogenic disturbances and conservation**

Because NARW habitats and migratory corridors overlap with fishing grounds and shipping lanes along the east coast of North America, two major anthropogenic causes of mortality are entanglement in fishing gear (Figure 1.3) and vessel strikes (Kraus et al. 2005, Knowlton et al. 2012, Moore 2014, Sharp et al. 2019). To avoid such unnatural mortalities, fishery regulations, dynamic area management, and seasonal area management have been issued by the Federal government, especially in northeastern and southeastern United States, the critical habitats of NARWs (Knowlton et al. 2012, Laist et al. 2014, Kraus et al. 2016). However, the human-related mortality rate is still high and is assumed to be increasing (Kraus et al. 2016, Pace et al. 2017). Due to an increased number of mortalities since the beginning of 2017, the National Oceanic and Atmospheric Administration declared an Unusual Mortality Event (UME) under the Marine Mammal Protection Act (NMFS 2017). Moreover, a recent publication using aerial photogrammetry revealed that the NARW population is in poor health when comparing to other right whale populations worldwide (Christiansen et al. 2020). These phenomena demonstrate an urgent need of understanding the mechanisms of human-animal interaction, as well as individual and population-level health.



Figure 1.3 An entangled North Atlantic right whale. Photo courtesy of the Florida Fish and Wildlife Conservation Commission, taken under NOAA Research Permit #15488.

### ***1.3 Energetics of the North Atlantic right whales***

#### **1.3.1 Foraging behavior of baleen whales**

Baleen whales (or Mysticeti) include the largest animals on earth. As their name implies, baleen whales have racks of baleen, instead of teeth, in their mouths. These keratinous plates grow downward from their upper jaw, lie between tongue and lip on both sides of the mouth, and filter prey from seawater when foraging (Clapham et al. 1999, Werth 2001). Both Balaenopterids (e.g., blue, fin, humpback, minke whales, etc.) and Balaenids (i.e., right and bowhead whales) use their baleen plates and fringes, filamentous tissues extended from the edge of baleen plates, to filter prey from water at the sea surface or deep in the water column (Clapham et al. 1999, Werth 2001). However, their foraging mechanisms are different (Werth

2004, Woodward et al. 2006a, Goldbogen et al. 2007). Balaenopterids forage with an strategy called lunge-feeding, in which the animal accelerates itself, opens its mouths, and then engulfs a considerable quantity of prey-laden water (Goldbogen et al. 2006, Goldbogen et al. 2007). The increased cross-section and surface areas of the animal due to mouth-opening, expansion of the buccal cavity, and drag of the baleen plates lead to extremely high drag condition when feeding and thus limit animal's dive durations (Goldbogen et al. 2006, Goldbogen et al. 2007). In contrast, Balaenids perform suspension feeding, or ram feeding, by swimming through prey-dense water at relatively constant speeds and continuously filtering waters with its mouth opened (Watkins and Schevill 1976, Werth 2001, 2004, Lambertsen et al. 2005). Differences between feeding mechanisms in both groups are associated with distinct morphological difference in body and appendage shapes (Woodward et al. 2006a). For instance, high aspect ratio flukes of Balaenids have been associated with skim feeding that requires continuous thrust production at a relatively slow speed (Woodward et al. 2006a). The length and number of baleen plates, as well as the stiffness and fineness of the mesh from fraying of the plates vary among species, reflecting their prey sources and strategies they use to feed (Clapham et al. 1999, Werth 2001). Filtration rate of an animal determines the time it needs to spend on foraging (Kenney et al. 1986, Baumgartner and Mate 2003, Goldbogen et al. 2007, Baumgartner et al. 2017, van der Hoop et al. 2019). A lower filtration rate implies that the animal performs fewer foraging attempts during each dive or that the prey availability is insufficient, so the total foraging

time required to search and intake enough food in order to meet its energy demands will be longer.

### **1.3.2 Energy budget of world's largest predators**

A positive energy balance (i.e., caloric intake of food is greater than the caloric expenditure for maintenance activities) is required by any individual to accomplish tasks other than survival. For example, female animals must store enough energy for pregnancy and lactation, and migratory species require adequate energy intake during feeding season (Williams and Maresh 2015). NARWs gather at their summer feeding grounds and forage on planktonic copepod (primarily *Calanus finmarchicus* stage 5) (Mayo and Marx 1990, Clapham et al. 1999, Baumgartner and Mate 2003, Baumgartner et al. 2007). Due to the high-drag nature of ram-feeding, NARWs require high-density prey patches for foraging to keep their energy consumption profitable. Baumgartner and Mate (2003) found that the prey density in NARW feeding grounds is enough to maintain the daily energy demand of an individual (i.e., metabolism and cost for foraging). However, a recent study suggests that most NARWs in their primary foraging grounds are just barely meeting their energy demands, especially lactating females (Nousek-McGregor et al. 2014). Hence, it is unclear whether the existing prey abundance is sufficient to support the whole population in terms of raising calves (Baumgartner and Mate 2003). Additionally, the specialized morphology of feeding apparatus and slow swimming speed of NARWs indicate that they are unlikely to switch to other prey (for example, herring) (Clapham et al. 1999, Mayo et al. 2001), and that

NARWs may spend more time searching for food as the distribution of copepods has changed.

### **1.3.3 Applications of computational modeling**

To investigate specific questions related to locomotor energetic (e.g., to calculate the thrust power generated by NARWs), the drag of a NARW needs to be determined first. Nousek-McGregor (2010) calculated the drag (131.81 N) on a NARW swimming at 0.97 m/s recorded with a digital tag attached on the animal, she also estimated the drag (114.67 N) when the animal swims at 0.51 m/s using a computational fluid dynamic (CFD) model. Working with an entangled whale during a disentanglement attempt, van der Hoop et al. (2014) empirically measured the drag on the entangled NARW prior to and after disentanglement. Their results suggested that the increased total power input due to added gear ranged from 4.1% to 120.9%, and the increased locomotive power requirements ranged from 60% to 164.6% under different gear configurations (van der Hoop et al. 2014b). A follow-up study compared the changes in locomotive patterns (e.g., fluke stroke rate) and kinematic parameters (e.g., thrust power and propulsion efficiency) of two entangled NARWs before and after disentanglement and concluded that entanglement had significant impacts on the locomotion in both cases (van der Hoop et al. 2017c). These studies estimated energetic expenditure of NARWs either numerically or empirically and provide an insight into the cost of locomotion for large marine mammals and the energetic liability due to entanglement.

## **1.4 Dissertation overview**

While there is an urgent need to protect the North Atlantic right whales, difficulties in understanding the hydrodynamics and energetics of this species are acknowledged. For instance, NARWs live in the open oceans and it is unlikely that their kinematics to be measured *in situ*, so to understand the true consequences (e.g., energetic costs) of events such as entanglement, one can turn to numerical methods informed by empirical data. Therefore, the broad objective of my dissertation is to use numerical methods to examine the hydrodynamic performance of the NARW from the standpoint of basic physics and energy.

## **Chapter 2 Computational fluid dynamics of flow regimes and hydrodynamic forces generated by a gliding North Atlantic right whale (*Eubalaena glacialis*)**

### ***2.1 Introduction***

Drag is the resistance to forward movement through a fluid(Vogel 1994). The drag is dependent on the viscosity and density of the fluid. The magnitude of drag is determined by physical properties such as fluid density, cross-section or wetted area of the object, and how fast it moves. This rule applies to living organisms, since they must overcome drag to move forward (Vogel 1994). Therefore, under selection pressure, ancestors of aquatic animals evolved streamlined body shapes to swim faster with a low energetic effort and increase their fitness in an aquatic environment (Fish 1993a, Vogel 1994, Woodward et al. 2006a). Namely, the smooth outline of these animals allows a thin layer of fluid (i.e., boundary layer) to attach to the surface of the animal. Within this layer, the flow remains laminar and incurs lower drag due to frictional forces within the boundary layer. In addition, the streamline body reduces the pressure differential around the body to minimize drag. To estimate the required energy output, one needs to measure the drag on these animals and, because the product of drag and velocity is power, the rate at which energy for propulsion is expended also requires an estimate of the drag (Vogel 1994). For that reason, the higher the drag, the more power, and therefore energy, is required by the animal to maintain a constant swimming speed.

The North Atlantic right whale, NARW, population declined dramatically and nearly to extinction due to commercial whaling in the nineteenth and twentieth centuries (Kraus et al. 2005). Currently, the NARW is one of the most endangered cetaceans worldwide with approximately 409 individuals remaining (Pettis et al. 2020). With few exceptions, hunting NARWs became illegal in 1935 and these animals have been protected in the U.S.A. by the Marine Mammal Protection Act and Endangered Species Act, which were enacted in the 1970s. However, NARWs are still on the edge of extinction due to two major anthropogenic causes of mortality: vessel strike and entanglement in fishing gear (Kraus et al. 2005, Sharp et al. 2019), and low reproductive output (Kraus et al. 2001, Pace et al. 2017, Corkeron et al. 2018).

Entanglement in fishing gear has been considered a central issue for the NARW population (Knowlton et al. 2016, Kraus et al. 2016). During entanglement events, these NARWs may end up having impaired physical functions (e.g., reduced feeding capability, emaciation, increased energy demands, inability to locomote effectively) for several months or years and eventually die due to drowning, starvation, or infections (Moore et al. 2010, Cassoff et al. 2011, Moore 2014, Knowlton et al. 2016, van der Hoop et al. 2017b, Sharp et al. 2019). Therefore, understanding the mechanisms and consequences of entanglement is crucial yet challenging, because *in situ* data collection is unlikely due to unpredictable location and timing of entanglements.

Although some entangled NARWs demonstrated behavioral differences from unencumbered individuals such as altered swimming patterns and diving depths (van der Hoop et al. 2014b, van der Hoop et al. 2017c), little is known about how these animals are affected by gear attachment in terms of energetic costs. Negative energy balance due to the additional costs of fishing gear drag can impact both individual and population health through decreasing body condition and inhibiting normal behavior, reproduction and migration for example (Williams and Maresh 2015). Therefore, estimating drag on NARWs is an essential approach to assess how energy demand has changed due to increased drag resulting from entanglement (Howle et al. 2018).

Several attempts have been made to estimate the drag or thrust power generated by aquatic animals. For example, fluid mechanical experiments in laboratories (Drucker and Lauder 2002), analyzing data collected by biologging tags in the field, or videotape recordings of captive animals have been conducted (Fish 1993b, 1998, Goldbogen et al. 2007, van der Hoop et al. 2017c). In addition, computational models have been shown as practical tools to calculate drag on marine mammals (Nousek-McGregor 2010, Shorter et al. 2014, Zhang et al. 2019).

With respect to the baseline drag estimates, computational fluid dynamics (CFD) models could be a solution when one tries to examine fluid mechanics of a fully-submerged marine animal (Shorter et al. 2014). Nousek-McGregor (2010) estimated drag on a NARW swimming at 0.514 m/s using a CFD model. Accurate estimates of drag on marine animals are required to investigate the overall

locomotive cost (Nousek-McGregor 2010), the propulsive efficiency (van der Hoop et al. 2017c), and the impacts of entanglement with respect to energy expenditure while the animal is carrying fishing gear (van der Hoop et al. 2017a, van der Hoop et al. 2017b). To my knowledge, no studies have systematically estimated hydrodynamic drag across the range of NARW's swimming speeds or analyzed flow regime on a gliding NARW using numerical methods.

Given the difficulties in measuring the drag on large whales in the field, I aimed to estimate the hydrodynamic forces using computer simulations in order to investigate the following questions: 1) how does the flow regime and boundary layer thickness change along the longitudinal axis of the NARW? and 2) how do various hydrodynamic forces, such as shear stress, drag, and pressure disperse on the NARW? The methodological approach taken in this study is a CFD analysis over a morphologically accurate 10 m NARW model using a commercial flow solver (SolidWorks Flow Simulation 2019) to obtain baseline measurements of drag and other hydrodynamic parameters on the NARW model. The research presented here provides one of the first investigations into the hydrodynamic properties of free-swimming, un-entangled NARWs and the only one to my knowledge that tests the range of swimming speeds observed for NARWs using CFD analysis.

## ***2.2 Methods***

In this study, CFD analysis was selected for providing detailed measurements of drag and other hydrodynamic parameters on a three-dimensional NARW model. Swimming speeds covering the known NARW range

were tested. Using the CFD simulations, I analyzed 1) boundary layer thicknesses, 2) flow regimes, 3) shear stress, 4) drag, and 5) pressure at a far-field flow speed of 2 m/s.

### **2.2.1 Three-dimensional right whale model**

Nousek-McGregor (2010) modified a three-dimensional NARW model in Blender 2.49 (Blender Foundation, 2010) based on geometric measurements of NARW from necropsy measurements and aerial photogrammetry. Aerial photographs of free-ranging animals were collected by the National Oceanic and Atmospheric Association (NOAA)'s Southeast Fisheries Science Center branch during the summers of 2000, 2001, and 2002 in the Bay of Fundy, Canada, following the methods of Perryman & Lynn (2002). This methodology enabled highly accurate 2D measurements to be taken from the dorsal view of individual animals, so measures of body length, body width, fineness ratio, fluke span, and fluke platform were collected (Perryman and Lynn 2002). Measurements collected from photogrammetry were then supplemented with measurements of necropsied animals to generate a three-dimensional model (Moore et al. 2005). Morphometric information obtained from a total of 165 adult NARWs were used to improve the fit of the three-dimensional NARW model.

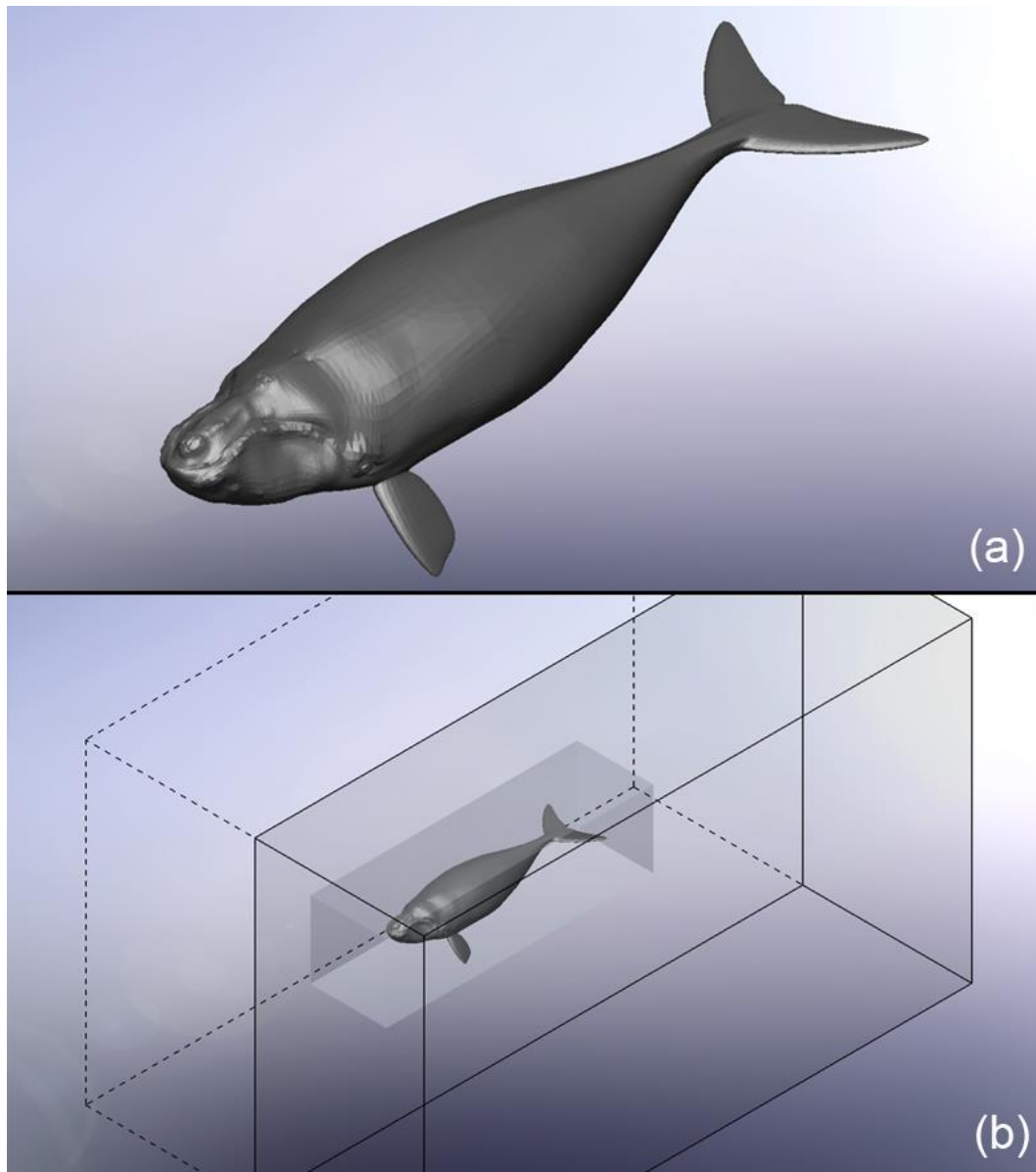


Figure 2.1 The three-dimensional NARW model. Note that the model (a) is displayed in its neutral gliding position in the computational domain (b) with flippers' midline perpendicular to the longitudinal axis of the animal and the dihedral angle of both flippers was 45 deg below horizontal platform. The fluke was displayed horizontally.

The static, morphologically accurate 10 m (length over all, LoA) NARW model was used for CFD simulations. The NARW model was displayed at a presumed neutral gliding position with flippers' midline perpendicular to the longitudinal axis of the animal and the dihedral angle of both flippers was 45 deg below the horizontal platform. The fluke is displayed in the simulated neutral orientation in (Figure 2.1a).

### **2.2.2 Hydrodynamic parameters**

#### Far-field flow speed

Hydrodynamic forces such as shear stress and drag are dependent on the relative speed between the surrounding fluid and the submerged object. To estimate the baseline forces on the NARW model, swimming speeds from 0.125 m/s to 8.0 m/s were simulated within the CFD study domain and the NARW model was assumed to remain static (non-articulating). The NARW model was centered at the frontal plane of the computational domain and placed somewhat closer to the front, because adequate distance is needed for turbulent flow trailing behind the animal to become stable.

#### Reynolds number

The dimensionless speed is given by the Reynolds number,  $Re$ , which expresses the ratio of inertial forces to viscous forces and is defined by

$$Re = \frac{UL}{\nu} \quad (2.1)$$

where  $U$ ,  $L$ , and  $\nu$  are, respectively, far-field flow speed, body length, and fluid kinematic viscosity. Reynolds number further characterizes the flow regimes: at a

lower Reynolds number below approximately 2000, the flow is laminar, whereas the flow becomes turbulent as the Reynolds number exceeds 2000 (Vogel 1994). For the present work, I used the overall length of the animal, 10 m, as the length scale in calculating the Reynolds number.

### Drag coefficient

For reporting the dimensionless drag, I use the drag coefficient,

$$C_D = \frac{D}{\frac{\rho}{2}U^2A} \quad (2.2)$$

where  $D$ ,  $\rho$ , and  $A$  are the drag force, fluid density, and drag area, respectively. For the drag area (discussed further in the Results section), I use the whale's exterior (wetted) surface area; 48.42 m<sup>2</sup> for the NARW model used in this study.

### **2.2.3 Numerical model**

The CFD simulations on the representative NARW model were conducted using the SolidWorks Flow Simulation 2019 software package (Dassault Systemes SolidWorks Corporation, Waltham, MA). The simulations were performed in a computational domain with dimensions of 14 m (wide) x 14 m (high) x 27 m (long) (Figure 2.1b). This computational domain was selected following a detailed domain size and mesh density convergence study (provided in the Supplemental Information). The simulations employed transport equations for turbulent kinetic energy and turbulent energy dissipation rate ( $k$ - $\varepsilon$  model). The default wall roughness and turbulence parameters were used as these gave reasonable results in previous work (Weber et al. 2011). The flow solver used a single system of equations to simulate laminar and turbulent flow with transition between these

flow regimes enabled. Laminar to turbulent transition is handled via the method of modified wall functions using Van Driest's profile instead of a logarithmic profile. Integral boundary layer theory is used if the local mesh size is smaller than the local boundary layer. Additional details of the simulation methods are available in the SolidWorks Flow Simulation technical documentation (Dassault Systemes SolidWorks Corporation, Waltham, MA). As inconsistent results were obtained with the automatic mesh refinement feature of the software in previous work (Weber et al. 2011), I manually specified the mesh geometry following a detail mesh convergence study with finite volume cells concentrating near the NARW model surface. For the full-domain simulations, I used a total of 11,517,423 finite volume cells. I ran 12 parallel flow speed simulations with the average solution time of approximately 4 h per simulation on an 80-processor workstation with 256 GB of RAM. When I undertook CFD simulations on the NARW model in its half-domain, I found discontinuous flow regimes on its midline (Figure 2.2), this issue was resolved when full-domain simulations were performed instead.

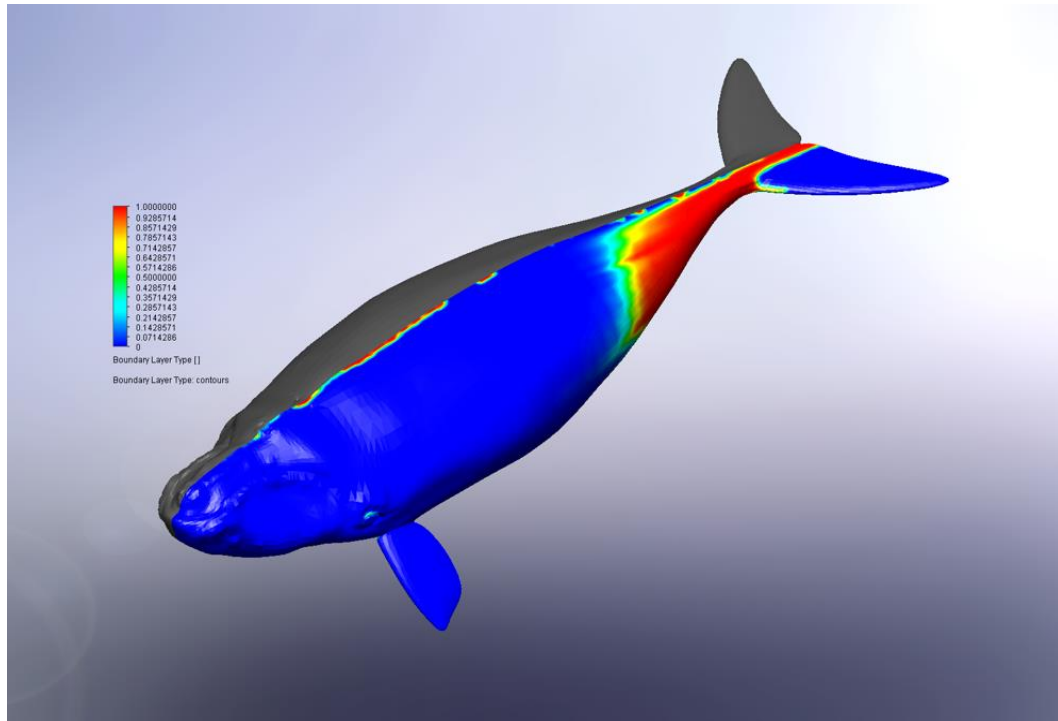


Figure 2.2 Boundary layer type simulated in half domain. Blue shows laminar flow while red shows turbulent flow. Intermediate colors indicate transitional flow. Turbulent flow anomalies are found at the midline of the NARW model when simulating in half-domain. This phenomenon is eliminated if the full domain model is used.

### **2.3 Results**

After CFD simulations were completed, I examined Reynolds numbers and drag coefficients for each tested flow speed and focused on hydrodynamic parameters measured at a far-field flow speed of 2 m/s. Particle pathlines simulated at a speed of 2 m/s around the left pectoral fin (Figure 2.3a) and the left fluke (Figure 2.3b) of the NARW model showed blue recirculating regions that indicate partial stall for the pectoral flipper and tip vortices that occur at the tip of

both the pectoral fin and the fluke (Figure 2.3, red arrows) indicating lift generation by these surfaces.

### **2.3.1 CFD model performance**

Because the issue of flow regimes near the midplane of the NARW model was resolved by undertaking full-domain simulations, the discontinuous flow regimes are considered artificial as results from a numerical interaction between the symmetry plane and the turbulence model. Other results, such as drag, shear stress, and pressure distribution, were not significantly affected by the symmetry plane – turbulence model interaction.

### **2.3.2 Fluid velocity and Reynolds number**

As shown in Figure 2.4, I found that the drag force vs. Reynolds number fit to a quadratic polynomial model ( $R^2=1$ ; Figure 2.4a, squares), whereas the drag coefficient was weakly dependent on Reynolds number (Figure 2.4a and 2.4b). Fluid velocity on the medial plane of the NARW model at a far-field flow speed of 2 m/s is shown in Figure 2.5. Higher fluid velocities on the animal appeared at mid-body regions (approximately 0.3 to 0.6 LoA) of the NARW, where the cross-sectional area of the animal was the greatest and above its blowholes (Figure 2.5, orange-red colors).

Lower fluid velocities appeared at regions before the rostrum and within the thin layer of water attaching to the NARW (i.e., the boundary layer; Figure 2.5, cyan-green colors). Lowest flow velocity was found at the tip of the rostrum at 0 m/s (Figure 2.5, blue color).

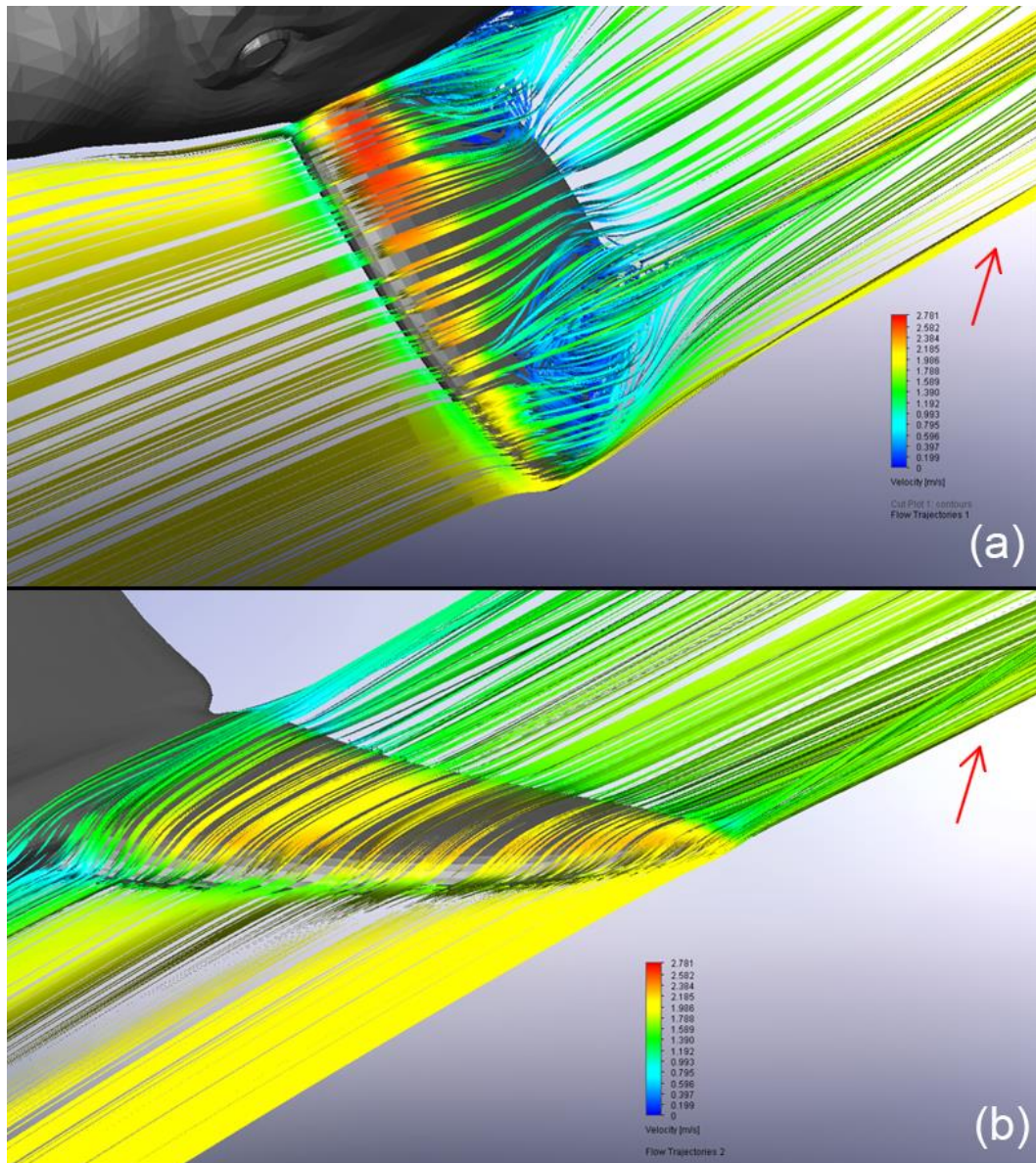


Figure 2.3 Particle pathlines on the flipper and the fluke of the NARW model. The far-field flow speed is 2 m/s. Warmer colors illustrate higher local flow speeds while cooler colors express lower speeds around the NARW. The blue recirculating regions on the left pectoral fin indicate partial stall. Tip vortices occurred at the tip of both the pectoral fin and the fluke (red arrows).

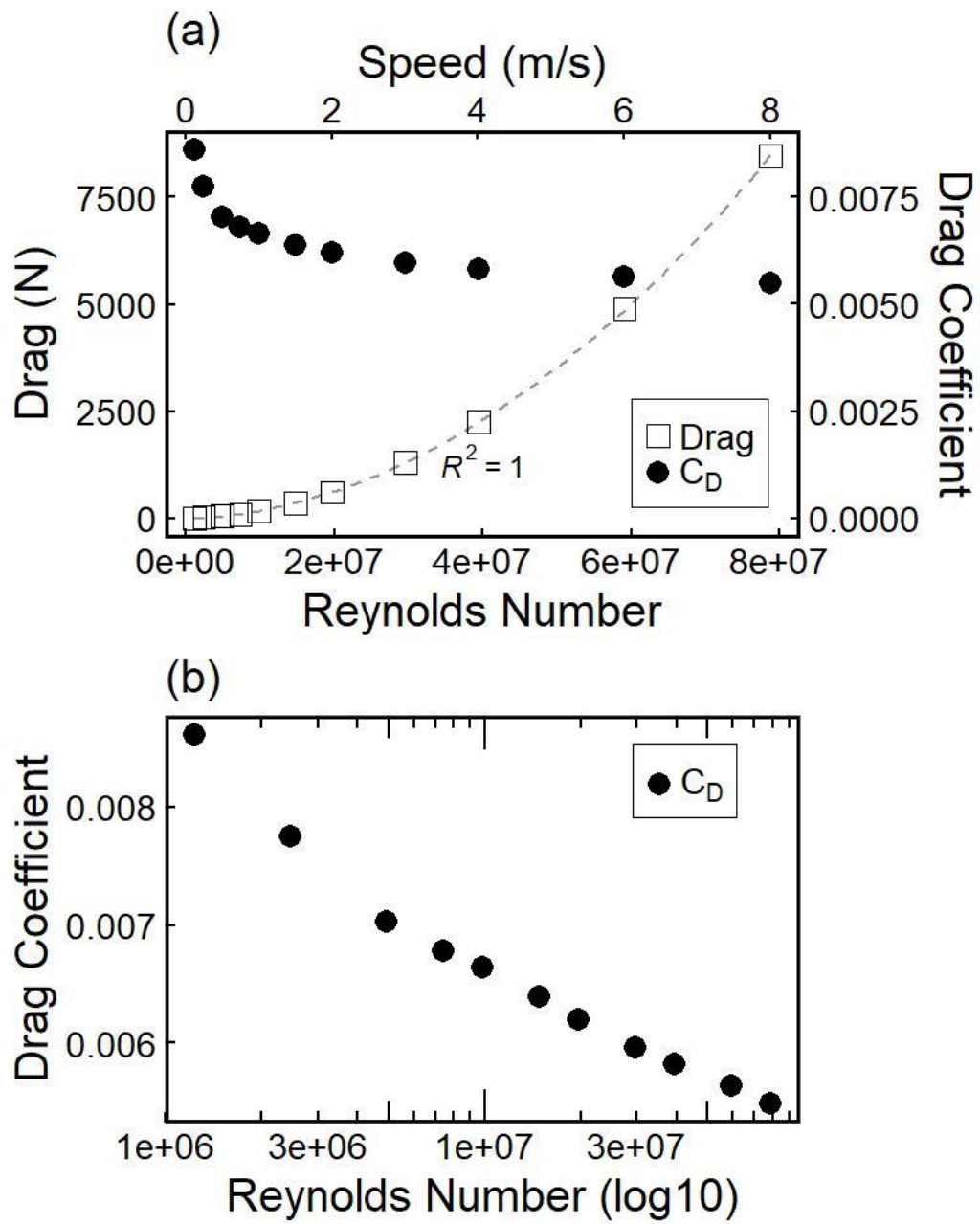


Figure 2.4 Drag and drag coefficient as a function of Reynolds number. Drag and Reynolds number fit to a quadratic polynomial model (a) whereas drag coefficient is weakly dependent on Reynolds number (a, b).

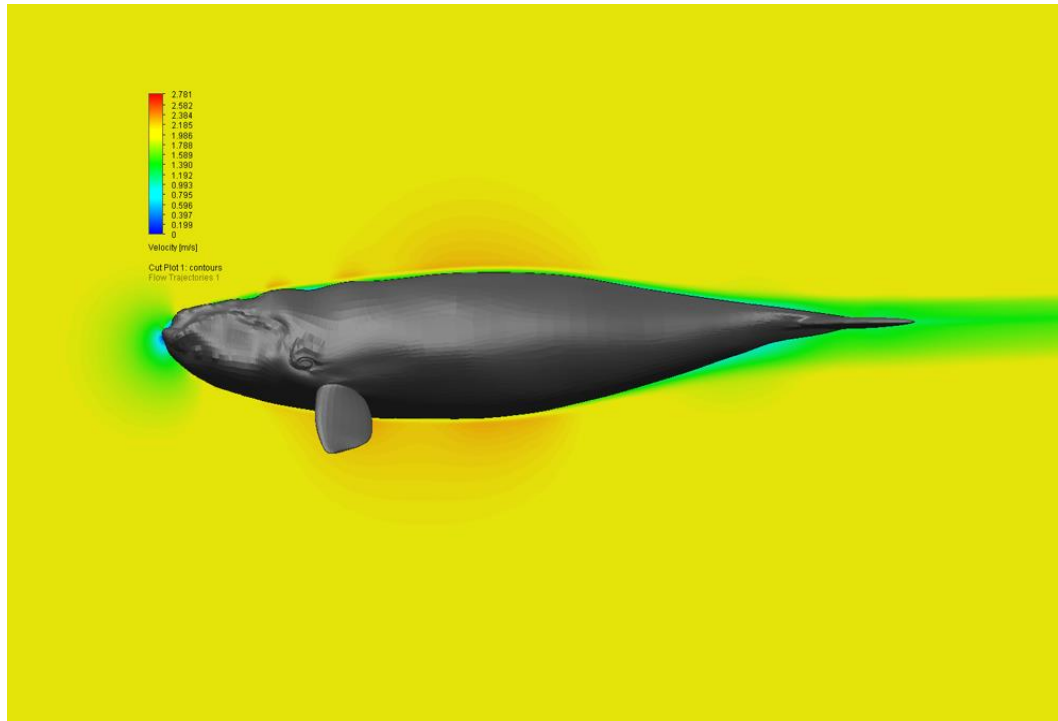


Figure 2.5 Fluid velocity on the medial plane of the NARW model. The flow speed is 2 m/s. Higher fluid velocities (orange-red colors) appeared at mid-body regions (approximately 0.3 to 0.6 LoA) of the NARW, where the cross-section area of the animal is the greatest, and above its blowholes. Lower fluid velocities (cyan-green colors) appeared at regions before the rostrum and within a thin layer of water attaching to the surface of the NARW (i.e., boundary layer). Lowest fluid velocity (blue color) was found at the tip of the rostrum (stagnation point) at a flow speed of 0 m/s.

### **2.3.3 Boundary layer thickness and type**

The boundary layer attaching to the NARW can be distinguished from the surroundings by the visualized flow speeds over the animal as shown in Figure 2.5: an overall thin boundary layer in regions of thickening animal cross-section (from the rostrum to approximately 0.6 LoA) and thickening boundary layer in regions

of diminishing cross-section (from approximately 0.6 LoA to fluke tips). The thickest boundary layer, over 23 cm, was found at the lateral sides of the peduncle, before the insertion point of the fluke (Figure 2.6a, regions in red), whereas the boundary layer over the outer parts of the fluke had a thickness less than 1.7 cm (Figure 2.6a, regions in blue on the flukes). The flow was laminar from the tip of the rostrum to approximately 0.6 LoA (Figure 2.6b, regions in blue) and was fully turbulent from approximately 0.8 LoA to the fluke notch (Figure 2.6b, regions in red). Furthermore, laminar flow occurred on the surface of the fluke outside of the body wake region (Figure 2.6b, regions in blue on the flukes).

#### **2.3.4 Shear stress, drag, and pressure**

In order to make some computations less expensive, the distributions of shear stress, form drag, and pressure on the NARW model were simulated in half domain as these quantities were unaffected by any symmetry plane – turbulence model interaction and are shown in Figure 2.7 and 2.8. The shear stress (Figure 2.7a) and its z component, the form drag (Figure 2.7b), were in opposite directions therefore the shading of the form drag was inverted (i.e., warmer colors indicate lower absolute values of drag force).

The shear stress and the form drag were higher in regions facing forward on the head, which correspond to the blunt shape and irregular outlines of the head. A few body parts also experienced higher form drag forces, e.g., the leading edge of the appendages (i.e., flippers and flukes). I found higher drag on the surface of the flippers and fluke close to the trailing edge.

The gradient of pressure force on the NARW model is presented in Figure 2.8. The highest pressure occurred at the tip of the rostrum, which is the stagnation point of the NARW, and the leading edge of the appendages (Figure 2.8, red color). Pressure in the head region and between approximately 0.6 LoA to the fluke notch was higher than in the mid-body regions (approximately 0.4 to 0.6 LoA), and the observed pressure distribution was comparable to the differences in fluid velocity shown in Figure 2.5. This phenomenon follows Bernoulli's principle (outside of the boundary layer): lower pressure is accompanied by higher flow speed and the fluid velocity is zero at the stagnation point.

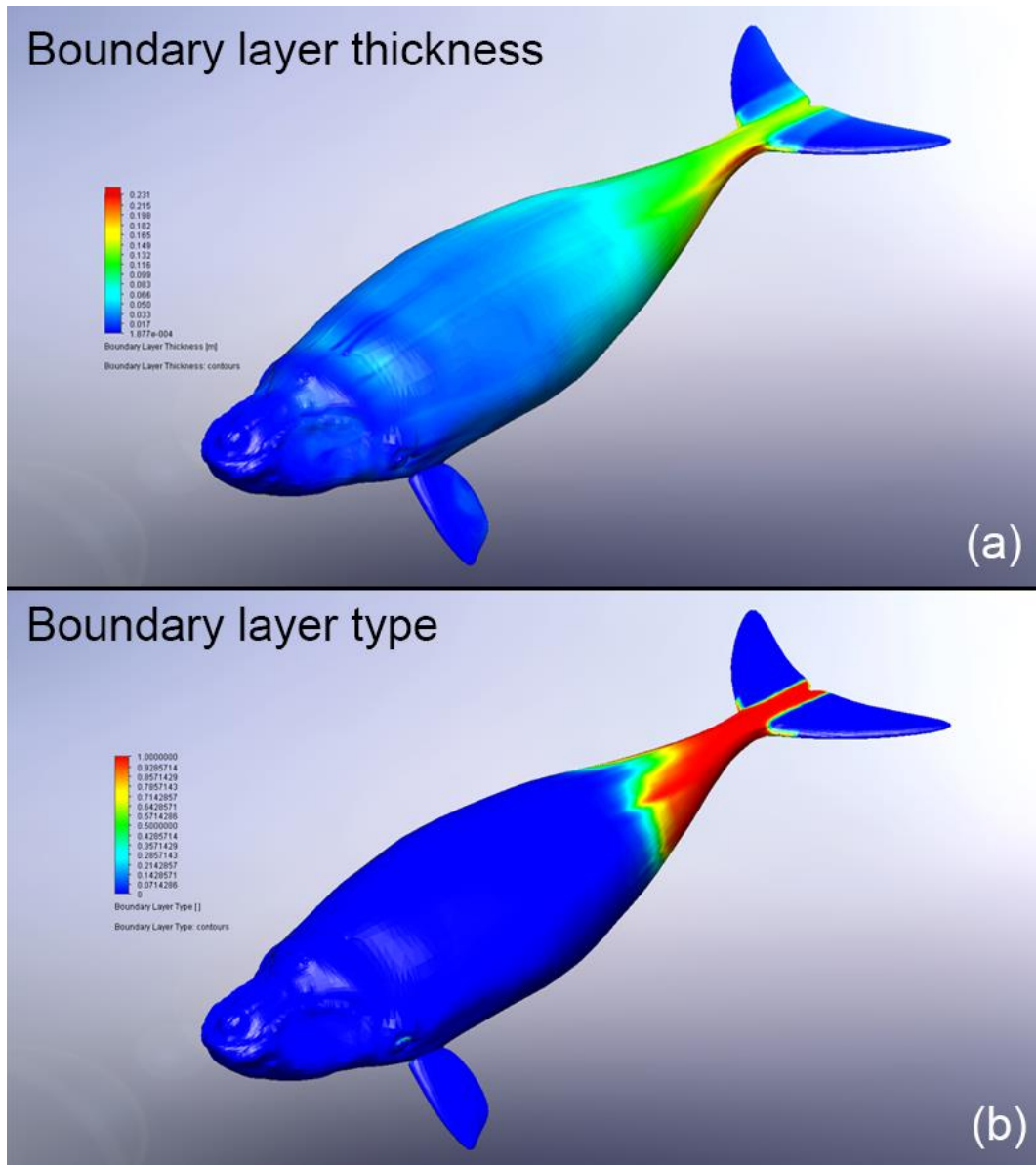


Figure 2.6 Boundary layer thickness and type. Overall thin boundary layer (cooler colors) in regions of thickening animal cross-section and thickening boundary layer (warmer colors) in regions of diminishing cross-section (a). The thickest boundary layer was found at the lateral sides of the peduncle, whereas the boundary layer over the outer part of the flukes was the thinnest. Flow is laminar (blue color) from the rostrum to approximately 0.6 LoA and is fully turbulent from approximately 0.8 LoA to the fluke notch (red color). Furthermore, laminar flow occurred on the surface of the flukes outside of the body wake region (b).

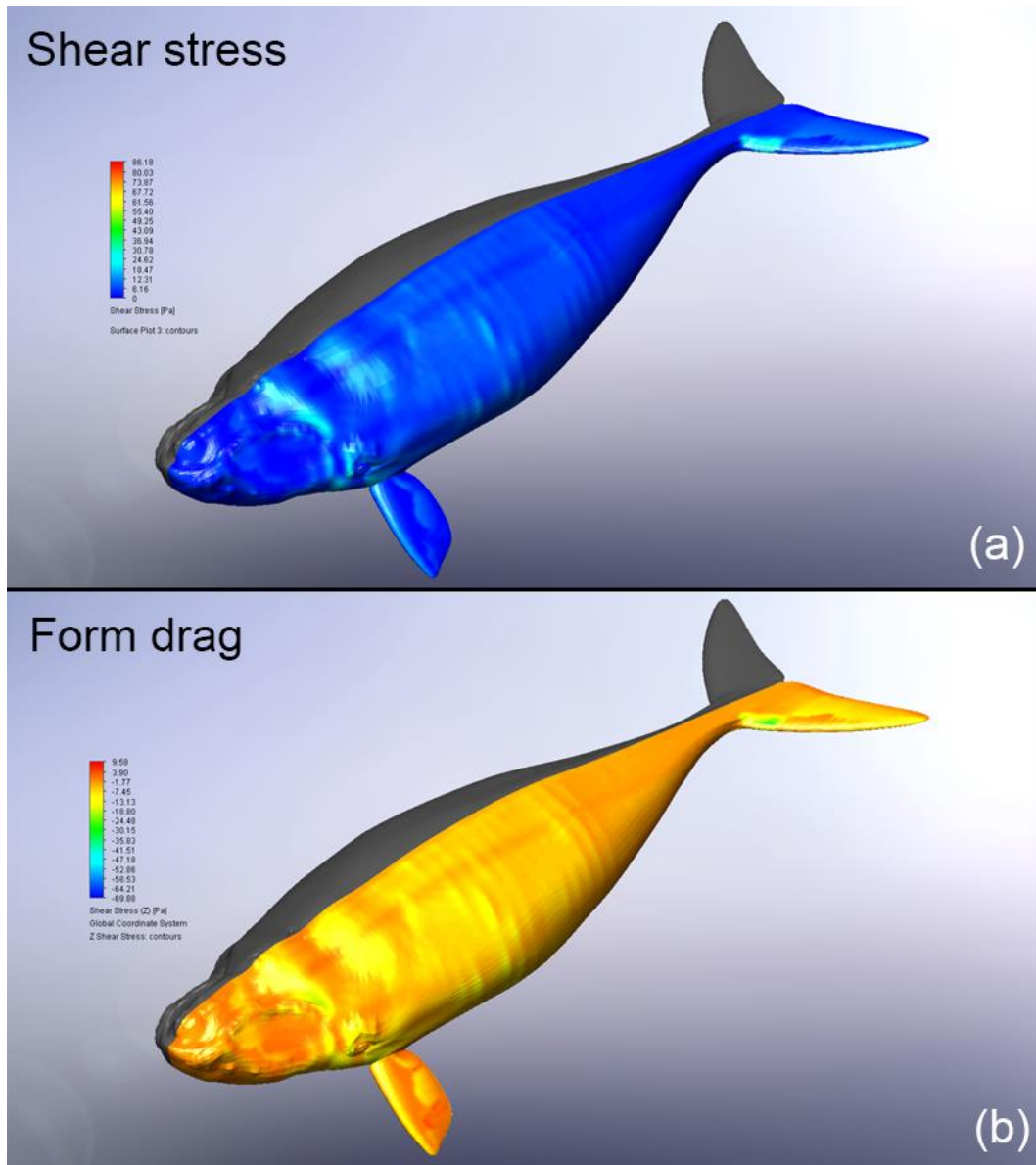


Figure 2.7 Shear stress and form drag on the NARW model. The form drag was in the opposite direction of the shear stress and therefore its shading was inverted (i.e., warmer colors indicate lower absolute values of drag force). The shear stress (a) and the form drag (b) were higher in regions faced forward on the head and the leading edge of the appendages. Drag on the surface of flippers and flukes close to the trailing edge was higher.

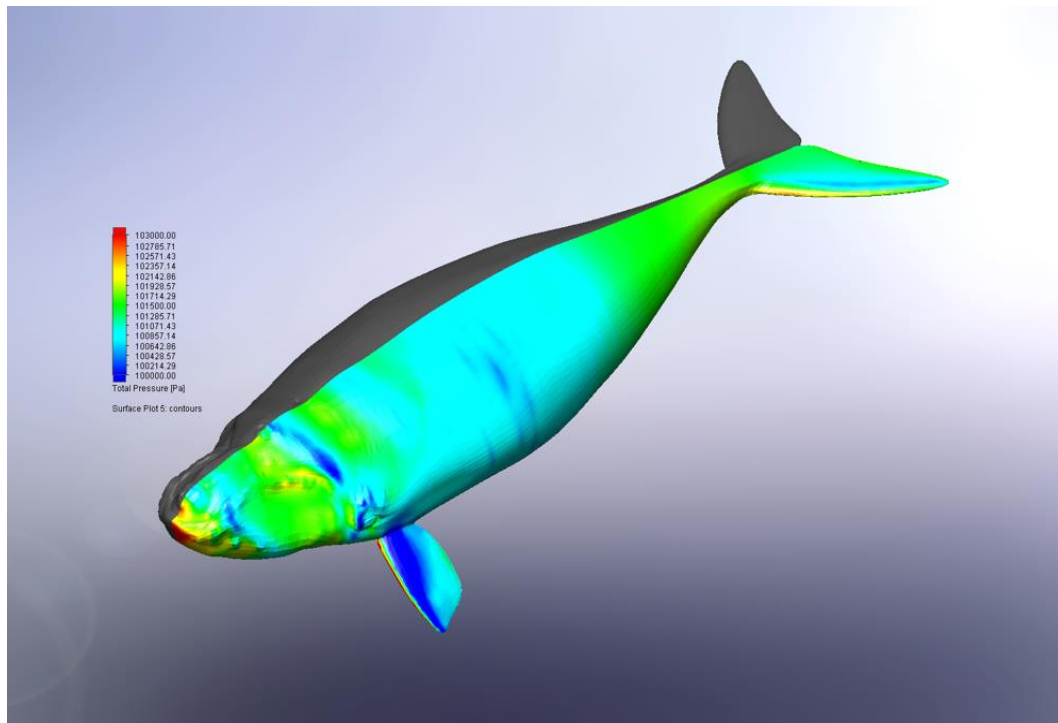


Figure 2.8 Pressure gradient on the NARW model. The highest pressure occurred at the tip of the rostrum and the leading edge of the appendages (red color). Pressure in head regions and approximately 0.6 LoA to the fluke notch was higher than the mid-body regions (approximately 0.4 to 0.6 LoA) of the NARW model.

## **2.4 Discussion**

Previous studies have shown the value in attempting to evaluate drag on free-swimming and entangled NARWs to understand the effects of entanglement in fishing gear on this species (Cassoff et al. 2011, Knowlton et al. 2012, Moore and van der Hoop 2012, van der Hoop et al. 2014b, Knowlton et al. 2016, van der Hoop et al. 2016, van der Hoop et al. 2017a, van der Hoop et al. 2017c). However, drag predictions under various circumstances are fragmentary: methodology and morphometric measurements of NARWs used by previous work were inconsistent.

Hence, the initial objective of this study was to obtain the baseline drag on a NARW across a range of swimming speeds via a computational approach.

### **2.4.1 Body length, surface area, and enclosed volume for $Re$ and $C_D$**

The similarity variables used for reporting dimensionless speed and drag, namely the Reynolds number and drag coefficient, require the input of length and area. For calculation of the Reynolds number, I used the whale's total overall length. For calculating the drag coefficient, the choice of drag area depends on the general drag-producing body and the dominant drag mechanics; for example, friction drag or pressure drag. Friction drag arises from fluid shearing force in a laminar or turbulent (or both) boundary layer and is typically the dominant drag mechanism for streamlined bodies in the absence of large regions of flow separation and in the absence of wave drag. Because the NARW model was placed at the central region of the cross section of the computational domain (i.e., the animal was not at or close to the surface as shown in Figure 2.1b), wave drag was not considered in this paper (Fish 2000). The drag area,  $A$ , is defined as

$$A \approx \frac{D}{q} \quad (2.3)$$

where  $D$  is the drag force and the dynamic pressure,  $q$ , is defined by

$$q = \frac{\rho}{2} U^2 \quad (2.4)$$

In equation 2.4,  $\rho$  is the fluid density and  $U$  is the far-field flow speed. In the absence of an informed choice of the appropriate area to use for calculation of the

drag coefficient, equation 2.2, the drag area given by equation 2.3 may be used (Hoerner 1965).

### **2.4.2 Hydrodynamic performance of the NARW**

The CFD model simulated local flow speeds and hydrodynamic forces on the NARW model (Figure 2.5, 2.7 and 2.8) and the gradient of such forces can be distinguished in regard to the contours of the model, especially in its head and post-nuchal regions. The results presented here may serve as a reference for future research that *inter alia* seeks for an ideal location to attach tags to NARWs. In addition, I found the frontal areas that face incoming flow endure higher drag, approximately two times the drag on adjacent areas. This finding is especially valuable when one investigates animals that are in poor body condition. Currently, researchers at the New England Aquarium (Boston, MA) have a protocol to assess NARW health. The body condition score is determined by the amount of fat in an individual's neck area (Pettis et al. 2004). Once an animal becomes emaciated, its body shape changes and usually concavities in the neck regions will be observed. Based on the model, I hypothesized that such concavities may 1) cause an animal suffer higher drag because the frontal areas are enlarged, and 2) destroy the boundary layer attached to the animal. Cetaceans, along with many other aquatic animals, have specialized morphology that delays separation of boundary layer and reduces drag while swimming (Vogel 1994). Therefore, shifts in body shape from a healthy body condition to a less-streamlined emaciated one could make flow separation on the animal occur earlier, ultimately causing higher drag. Emaciation

indicates that the animal cannot intake enough food to support its basal metabolism and locomotive cost while nonideal body shape makes this situation worse. For those NARWs that become emaciated due to entanglement in fishing gear (Knowlton and Kraus 2001), they may therefore still experience higher drag after they are freed and need a longer time to recover. If it is a reproductive female, its birth interval could be extended in order to physiologically recover after a combination of reproduction and entanglement. Pettis et al. (2017) showed that recovering from less-streamlined body shape to optimal body condition may take approximately a year for minor-to-moderate entangled individuals and resting females. Therefore, I recommend that energy expenditure associated with transformed body shape should serve as an additional factor when conducting animal and population health assessments.

### **2.4.3 Whale drag predictions**

By referring to the nondimensional drag coefficient of a submerged object, drag forces are comparable between objects of different shapes under various flow conditions as long as the dimensionless similitude parameters match. For that reason, measurements of drag coefficient as a function of Reynolds number from current and previous studies across cetacean species are shown in Figure 2.9 in order to compare drag coefficients across different body shapes, lengths, and swimming speeds (Lang and Daybell 1963, Bose and Lien 1989, Fish 1998, Miller et al. 2004, Nousek-McGregor 2010, van der Hoop et al. 2014b, van der Hoop et al. 2017c). The values of drag coefficients from the literature are listed in Table 2.1.

Nousek-McGregor (2010) undertook CFD simulations on a three-dimensional NARW model and calculated drag with a hydrodynamic model and data collected from NARWs in their habitats. van der Hoop *et al.* (2014) also calculated drag with a hydrodynamic model and data recorded by animal-borne tags attached to a NARW.

Lang and Daybell (1963) estimated drag with a hydrodynamic model and data collected from the literature, a blue whale (*Balaenoptera musculus*), and from video footage of a captive Pacific white side dolphin (*Lagenorhynchus obliquidens*). Miller *et al.* (2004) calculated drag on sperm whales (*Physeter macrocephalus*) with a hydrodynamic model and data recorded by animal-borne tags. Fish (1998) video-recorded captive cetaceans, including orcas (*Orcinus orca*), false killer whales (*Pseudorca crassidens*), belugas (*Delphinapterus leucas*), and bottlenose dolphins (*Tursiops truncatus*), and estimated drag based on decelerations of the video-recorded animals. Drag coefficients of a fin whale (*Balaenoptera physalus*) fluke calculated by Bose and Lien (1989) are included for comparing research methods. As shown in Figure 2.9, under similarity conditions, which are represented by Reynolds number here, these animals are affected by drag at different levels and I found that the drag estimation for NARW was higher than predicted by previous studies for other large whale species.

While there is no need to know exactly the values of each component of drag coefficients and Reynolds numbers for each species to undertake such

comparisons (Vogel 1994), one must acknowledge that 1) every drag coefficient and Reynolds number is calculated under particular conditions, regardless of which parameter has changed in the course of measurements, and 2) both experimental (e.g., video footage and tagging) and numerical (e.g., CFD simulation) approaches simplify the calculation. Possible explanations for such diverse results may be differences in the morphology of the animals, their swimming speeds and capabilities, and various methods used to calculate drag. For instance, when cruising at similar speeds, slender body shapes of orquals suggest that they encounter lower drag and have higher swimming efficiency than NARWs, sperm whales, and belugas (Fish 1998, Goldbogen et al. 2006, Woodward et al. 2006a), whereas the latter species have developed corresponding morphological or behavioral specializations to overcome inefficiency due to their body form.

Higher swimming speeds during foraging observed in *Delphinidae* such as orcas and bottlenose dolphins force them to endure higher drag since drag increases with the square of speed (Vogel 1994, Fish 1998). Lastly, advanced computer technology enhances the resolution of three-dimensional NARW models and CFD flow solvers, and therefore provides more precise drag estimations at the expense of being static representations of moving animals. The capabilities of modern computers and filming equipment are also crucial for analyzing video recordings of captive animals.

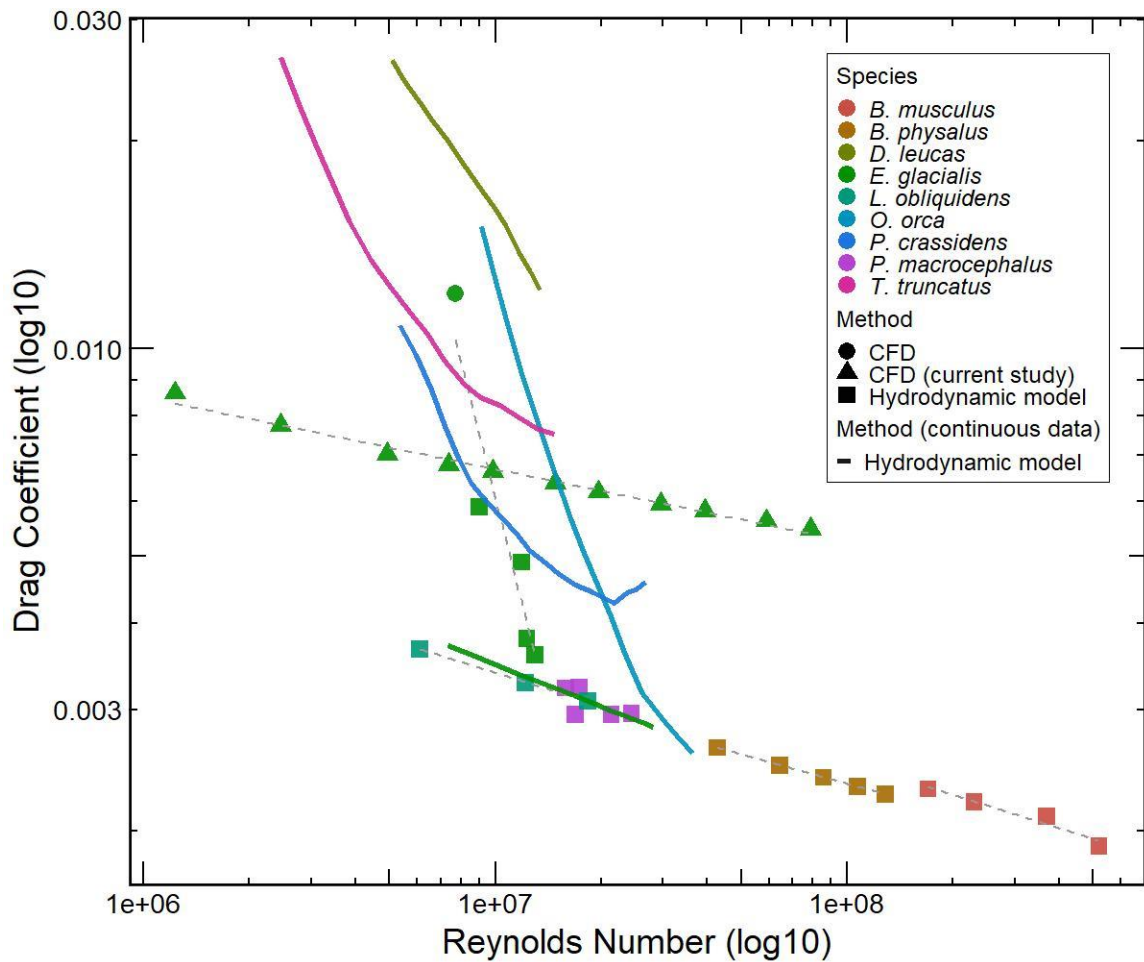


Figure 2.9 Drag coefficients across species from current and previous studies as a function of Reynolds number. Drag coefficients of large whales, including blue, fin, right, and sperm whales, are relatively smaller than orcas, false killer whales, belugas, bottlenose dolphins, and Pacific white side dolphins that have smaller body sizes under similar flow conditions, which are represented by Reynolds number. Drag coefficients from the current study of NARWs (solid dots) are relatively higher among large whale species. (Refer to Table 2.1 for data sources.)

Table 2.1 Drag coefficients across species from current and previous studies.

Species	LoA <sup>&amp;</sup> (m)	Re ( $\times 10^7$ )	C <sub>D</sub> ( $\times 10^{-3}$ )	Model	Reference
<i>Eubalaena glacialis</i>	10	1.24-7.96	7.7-5.3	CFD	Current study
<i>Eubalaena glacialis</i>	15	0.771 <sup>*</sup>	12	CFD	Nousek-McGregor (2010)
<i>Eubalaena glacialis</i>	10-13	0.90-1.30 <sup>*</sup>	5.9-3.6	SHM <sup>§</sup>	Nousek-McGregor (2010)
<i>Eubalaena glacialis</i>	9.45	0.73-2.81 <sup>*</sup>	3.7-2.9	SHM	van der Hoop <i>et al.</i> (2014)
<i>Balaenoptera musculus</i>	21.95	17-52	2.3-1.9	SHM	Lang and Daybell (1963)
<i>Balaenoptera physalus</i>	14.5	4.28-12.9	2.64-2.26 <sup>†</sup>	SHM	Bose and Lien (1989)
<sup>∞</sup> <i>Physeter macrocephalus</i>	10.0-13.4	1.92	3.06	SHM	Miller <i>et al.</i> (2004)
<i>Orcinus orca</i>	3.81-5.57	0.909-3.65	15.4-2.6	SHM	Fish (1998)
<i>Pseudorca crassidens</i>	3.55-3.99	0.535-2.71	10.8-4.7	SHM	Fish (1998)
<i>Delphinapterus leucas</i>	3.25-4.12	0.500-1.30	26.5-12.7	SHM	Fish (1998)
<i>Tursiops truncatus</i>	2.51-2.70	0.245-1.48	27-7.7	SHM	Fish (1998)
<i>Lagenorhynchus obliquidens</i>	2.04	0.61-1.83	3.67-3.08 <sup>‡</sup>	SHM	Lang and Daybell (1963)

<sup>&</sup>length of the animal  
<sup>§</sup>simplified hydrodynamic model  
<sup>\*</sup>Re values were calculated from swimming speed and animal length provided in the article while using kinematic viscosity for seawater =  $1 \times 10^{-6}$  m<sup>2</sup>/s  
<sup>†</sup>drag on the fluke  
<sup>‡</sup>drag on the body (appendages were excluded from calculation)

#### **2.4.4 Limitations of drag estimation**

It is important to bear in mind the simplified calculations utilized by both hydrodynamic and CFD models. For example, in the cases of estimating drag from animal-borne tags and video recordings (i.e., *in situ* measurements), the outcome forces comprise not only the small-scale flow circulating on the animal but also currents and waves (e.g., wave drag) if the animal is close enough to the surface (Vogel 1994). In other words, the hydrodynamic models have taken the environmental impacts into account while the CFD models assume that the incoming flow is turbulence-free and neither sea surface nor sea floor is included in the calculation. However, those physical factors experienced by animals in the real world are unlikely identical in any part of the water column, which implies that the drag estimations calculated from *in situ* data are correct under specific conditions but not other conditions. On the other hand, even though the discrete cells in the three-dimensional animal model and flow simulated in high resolution calculations provide more accurate drag estimations, CFD simulations assume the animal is a rigid body without flexibility and maneuverability. By doing so, CFD models generate a best-estimate of the baseline drag on the animal but overlook the impacts of trailing vortices induced by animal locomotion, fluke pitching and undulating of the whole body for example, which also known as the induced drag (Lighthill 1969, Hall and Hall 1996, Hall and Howle 2005). In addition, differences between skin texture or roughness of the three-dimensional model and real tissue suggest bias toward calculations of friction force (i.e., the skin is not completely

smooth on real animals, particularly the rough callosities on the heads of NARWs). Moreover, when calculating drag coefficient, most models simplify the outline of an animal by applying the equation derived for a flat plate or body of revolution (see above discussions on animal length, surface area, and enclosed volume), although the shape of cetaceans is to some extent between a flat plate and a blunt body, which is varied among species (Fish 2002).

## ***2.5 Conclusion***

This is the first comprehensive study of drag and other hydrodynamic characteristics of NARWs through a CFD approach. Results presented here show that drag on NARWs is higher than previous estimates on this species and measurements of other large whales. Since NARWs are frequently observed being entangled in fishing gear and consequently some individuals suffer from emaciation, investigations on potential increased energetic costs due to imperfect body shapes are required for animal health assessments. Given the capability of CFD models to provide detailed force distributions on a whale model as shown in the present study, it is practicable that this method can be applied to estimating hydrodynamic forces on animals with various body shapes.

# **Chapter 3 Computational fluid dynamic analysis of gliding North Atlantic right whale models with variable body shapes**

## ***3.1 Introduction***

Currently, there are approximately 409 North Atlantic right whales (hereafter NARW) living along the east coast of North America (Pettis et al. 2020). NARWs were historically considered the “right” whale to hunt by whalers because they are slow swimmers, inhabit coastal seas, have thick blubber and large baleen plates, and were more likely than other whales to float when killed (Reeves and Mitchell 1986a, b). Even though hunting of NARWs was banned in the 1930s, anthropogenic activities are still threatening this population today (Knowlton and Kraus 2001, Kraus et al. 2016, Corkeron et al. 2018). Entanglement in fishing gear is of primary concern in regard to population decline (Knowlton et al. 2012, Knowlton et al. 2016, Kraus et al. 2016). Once entangled, these animals may end up having impaired physical functions such as inhibited feeding ability (Johnson et al. 2005, Cassoff et al. 2011), injuries associated with fishing gear encounter (Woodward et al. 2006b, Cassoff et al. 2011, Moore et al. 2013, Daoust et al. 2017), stress responses (Rolland et al. 2017), and increased energy demands (van der Hoop et al. 2017c). Unlike other Balaenidae species, the NARWs show little sign of recovery (Kraus et al. 2016, Corkeron et al. 2018). On top of that, a recent study suggested that, compared to Southern right whale populations, the NARWs have an overall poorer body condition across reproductive classes except for calves (Christiansen et al. 2020).

In an aquatic environment, the streamlined body shapes and transformed limbs of cetaceans cause delayed flow separation, reduced drag during swim, and therefore decreased energetic costs (Fish 1993a, Vogel 1994, Woodward et al. 2006a). In effect, the more streamlined a NARW is, the more energetically-efficient the whale can swim. Additionally, observations at sea and locomotive data recorded by animal-borne tags indicated that cetaceans may adjust their behaviors to lower the energetic cost of swimming (Williams et al. 1992b, Nowacek et al. 2001, Miller et al. 2004, Goldbogen et al. 2006, Nousek-McGregor et al. 2014, van der Hoop et al. 2014a, Williams and Maresh 2015). The total cost of transport (COT) is used to estimate the energetic expenditure of aquatic animals, which is the sum of the maintenance cost, the rate of oxygen consumed by the animal, and the locomotor cost; it is the energetic cost of swimming (Fish 1993a, Williams 1999, Williams and Maresh 2015). While direct measurements of the metabolic cost of large cetaceans is unlikely (Williams and Maresh 2015), the cost of locomotion calculated from drag in large marine mammals can be estimated with field observations and computer models (Miller et al. 2004, Goldbogen et al. 2007, Williams and Noren 2009, Nousek-McGregor 2010, Goldbogen et al. 2012, van der Hoop et al. 2017c, Zhang et al. 2019). However, little is known about how important these hydrodynamic properties are at the population level.

It is known that, for marine mammals, the extent of energy reserves associated with critical life history events (e.g., reproduction, migration, foraging, etc.) will affect blubber thickness throughout the animal body at various level and

between animals in different demographic groups and life stages (Lockyer 1986, Reeves and Mitchell 1986b, Koopman 1998, Koopman et al. 2002, Pettis et al. 2004, Miller et al. 2011, Bradford et al. 2012, Miller et al. 2012, Pettis et al. 2017b, Solvang et al. 2017). Additionally, results from chapter 2 indicated that drag on NARWs varied with position due to the irregular outline of the animal body. Therefore, from a physical standpoint, I believed that estimating drag on NARWs with different body shapes is an essential approach to assess how energy demand has changed resulting from body deformation, as the hydrodynamic drag is the primary source of energy expenditure of animals moving in a fluid without actively propelling themselves (Tucker 1975). In this study, body deformation is referred to change in the body shape of the animal, primarily due to nutritive condition.

Some methods that have been used to investigate energetics of NARWs include calculating the volume of blubber loss through photogrammetry (van der Hoop et al. 2017b), analyzing kinematic data collected with digital tags during disentanglement (van der Hoop et al. 2014b, van der Hoop et al. 2017c), and estimating hydrodynamic forces with numerical methods (Nousek-McGregor 2010). After examining methods described in previous studies, I aimed to analyze hydrodynamic forces on NARWs with different body fitness by using highly refined numerical models and determine whether changes in body shape lead to variations in flow properties and hydrodynamic forces. I hypothesized that both emaciated and pregnant NARWs will encounter higher drag due to a less streamlined body

shape of the emaciated animal and increased surface area of the pregnant individual, respectively.

## **3.2 Methods**

### **3.2.1 Three-dimensional NARW models**

A morphologically-accurate three-dimensional NARW model was adopted from chapter 2 and used as the normo-nourished model in this study. Emaciated and pregnant NARW models were constructed in Blender v2.79 (Blender Foundation, 2017) for comparison (Figure 1). In order to create NARW models with variable body shapes, I examined NARW images archived in the North Atlantic Right Whale Catalog (North Atlantic Right Whale Consortium). I found only one individual (EG# 2145) had images taken from different angles with post-nuchal concavity displayed (Figure 2a and 2b, images were taken on 07 October 2017 by the New England Aquarium). Those images were imported into Blender and set as the background, and the normo-nourished model was sculpted into an emaciated model (Figure 2c). Given the limited number of archived images demonstrating body shapes of emaciated NARWs, my emaciated NARW model 1) was not a replica of any specific animal(s), and 2) only exhibited the post-nuchal concavity with additional though lesser circumferential losses of body fat. Exact changes in the contour of the ventral side, as well as in mid-body region and peduncle of an emaciated NARW were not the focus of this work. The relative body width of the emaciated NARW model at its 30-40% LOA is in agreement with lactating (hence, thinner) NARWs observed in the wild (Christiansen et al. 2020).

Likewise, I built a pregnant NARW model by using a pregnant NARW model described in Nousek-McGregor (2010) and then normalizing it to the 10 m length I have for the other two. The NARW model has its maximum body width around 40% LOA, which is similar to the measurements for pregnant NARWs in Miller *et al.* (2012). Hence, both emaciated and pregnant NARW models were expected to provide us an insight into the hydrodynamic forces encountered by the wild individuals.

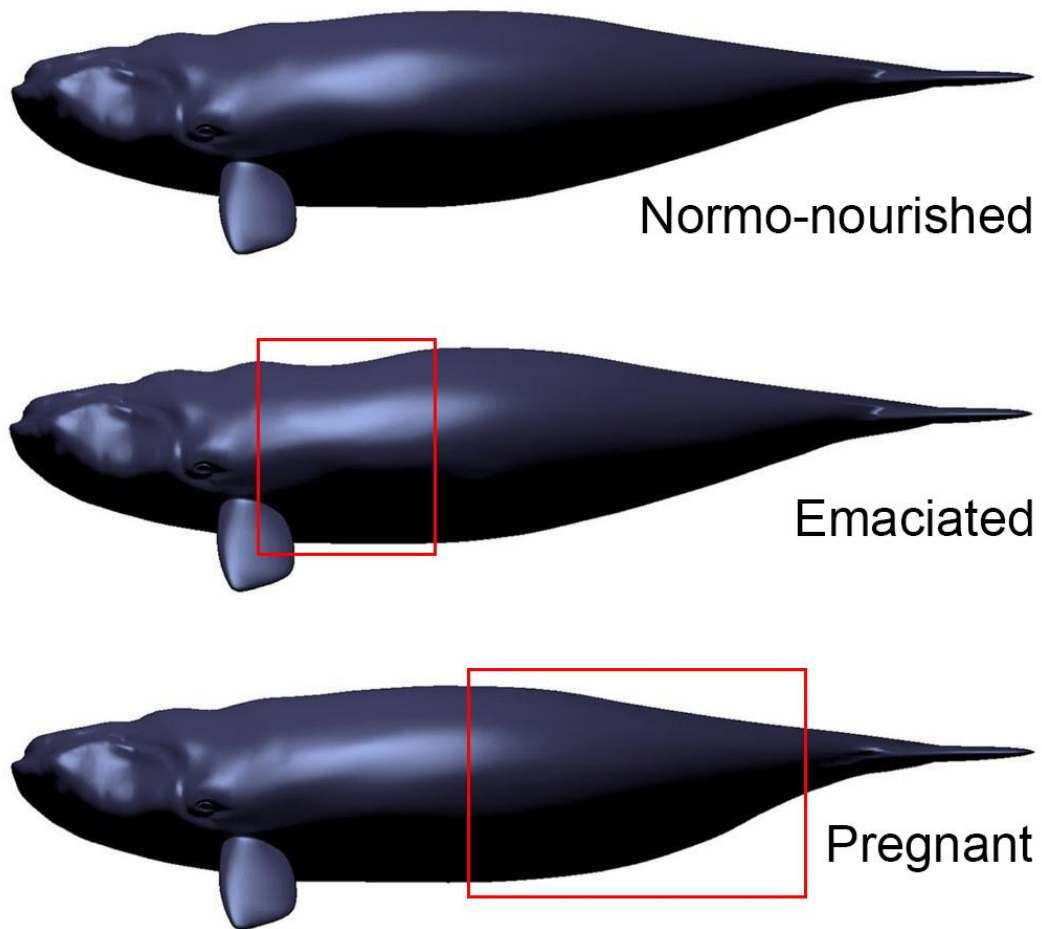


Figure 3.1 Lateral view of the North Atlantic right whale models. All models, including a normo-nourished NARW, an emaciated NARW, and a pregnant NARW (from top to bottom), were built in Blender v2.79. Highlighted in red boxes are the concavity of the emaciated NARW and the enlarged abdomen of the pregnant NARW.

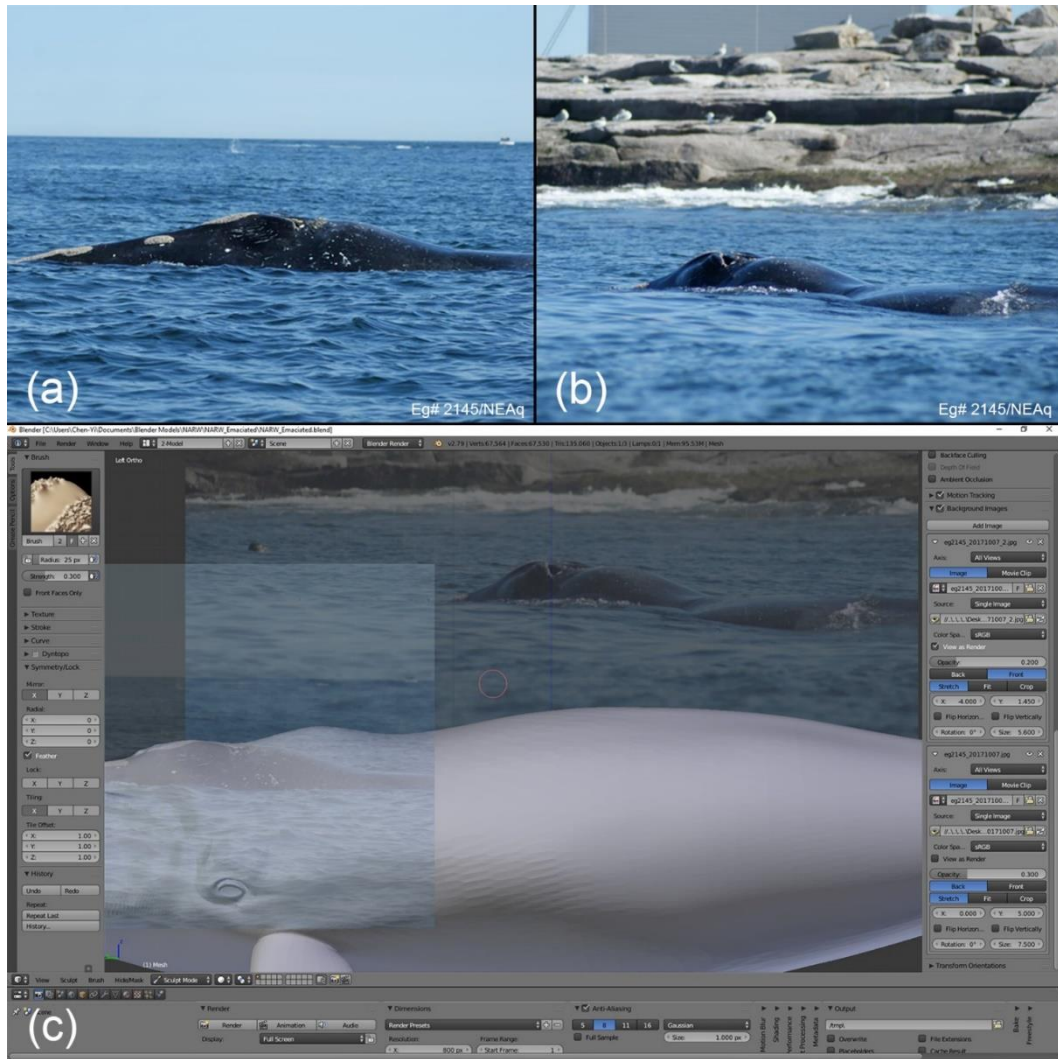


Figure 3.2 Constructing NARW models with different body shapes. Photographs of an emaciated NARW (a and b) were imported to Blender v2.79 (c) in order to build the NARW model with post-nuchal concavity. Photo courtesy of New England Aquarium.

### Morphometric parameters of the models

Morphometric measurements of three models are provided in Table 3.1. Among these parameters, overall length of the animal (LOA), surface area, and

volume of the NARW models were measured by the SolidWorks Flow Simulation 2019 software package. Maximum animal girth was manually measured in Blender software with the formula for the circumference of an oval applied:

$$girth_{max} = 2\pi \sqrt{\frac{a+b}{2}} \quad (3.5)$$

In equation 3.1,  $a$  and  $b$  are the major and minor axes of the cross-section of the animal, respectively. Maximum body diameter of the animal was given by

$$d_{max} = \frac{girth_{max}}{\pi} \quad (3.2)$$

Lastly, fineness ratio ( $FR$ ) of the models were calculated as

$$FR = \frac{LOA}{d_{max}} \quad (3.3)$$

With these measurements, I was able to quantify the body shapes of the three NARW models and associate them with the results generated by CFD simulations.

### **3.2.2 Hydrodynamic parameters**

#### Far-field flow speed

Fluid speeds from 0.125 m/s to 8.0 m/s were simulated within the CFD study and the NARW model was assumed to remain static (non-articulating). The flow speeds used here were inherited from previous work, as they covered known NARW speed range (Watkins and Schevill 1976, Mate et al. 1997, Woodward et al. 2006a, Nousek-McGregor 2010, Hain et al. 2013).

#### Reynolds number

To compare hydrodynamic forces between models with different shapes, the Reynolds number,  $Re$ , was selected for reporting dimensionless speed, which can be calculated as

$$Re = \frac{UL}{\nu} \quad (3.4)$$

In equation 3.4,  $U$ ,  $L$ , and  $\nu$  are, respectively, far-field flow speed, body length, and fluid kinematic viscosity. For the present work, I used the overall length of the animal as the length scale in calculating the Reynolds number.

#### Drag coefficient

Likewise, for comparing drag between models, I used the drag coefficient,

$$C_D = \frac{D}{\frac{\rho U^2 A}{2}} \quad (3.5)$$

where  $D$ ,  $\rho$ , and  $A$  are the drag force, fluid density, and drag area, respectively.

For the drag area, the whale's exterior surface area was used as measured by SolidWorks software (Table 3.1). Note that the drag area is different for the three models considered in this study. This last point has implications on the interpretation of the results I report. For example, it would be possible to have a situation where all three models experience the same dimensional drag, yet the drag coefficients could differ between the models as a result of the models' differing drag areas.

Table 3.1 Morphometric measurements of three NARW models tested.

Dimension	Normal-nourished	Emaciated	Pregnant
Body length (m)	9.89	9.98	9.89
Surface area (m <sup>2</sup> )	48.42	47.89	51.05
Volume (m <sup>3</sup> )	16.84	16.42	18.73
Number of grid cells	23,188,635	23,228,602	23,006,525
Girth (m)	7.04	6.84	7.12
Maximum body diameter (m)	2.24	2.18	2.27
Measurement site of the maximum body diameter (% LOA)	41.8	44.4	45.12
Fineness ratio, <i>FR</i>	4.41	4.59	4.36

### 3.2.3 Energetic costs for NARW from hydrodynamic models

In order to swim at a constant speed, animals must generate enough thrust to equal drag for the animal's movement through the fluid (Vogel 1994). The required thrust power of a gliding NARW is given by

$$P_T = D \times U \quad (3.6)$$

where  $D$  is hydrodynamic drag and  $U$  is the swimming speed of the animal. In this study, the NARW models remained static in the computational domain so the flow speeds were used as the swimming speed in equation 3.6. Total energetic cost of locomotion (i.e., the energy output associated with movement) at a given time period can be calculated by

$$E = P_T \times T \quad (3.7)$$

where  $T$  is elapsed time. The unit of total energetic cost is joules, which can be converted to calories by

$$E_{(\text{cal})} = \frac{E_{(\text{joule})}}{4.18} \quad (3.8)$$

### 3.2.4 Numerical model

In this study, the SolidWorks Flow Simulation 2019 software package was used to perform CFD simulations on 3-D NARW models with different body shapes (Dassault Systemes SolidWorks Corporation, Waltham, MA). The simulations employed transport equations for turbulent kinetic energy and turbulent energy dissipation rate ( $k$ - $\varepsilon$  model). However, while I acknowledged the differences between the NARW models and aimed to correlate such differences with their hydrodynamic performance, all three models have similar body size, length, and surface area due to how they were designed (refer to *Three-dimensional NARW models* in Method section and Table 3.1 for morphogeometric measurements). Therefore, I decided not to repeat the domain size convergence study but apply the dimensions of the computational domain from chapter 2 to the new models. Likewise, I specified the mesh geometry of the three NARW models based on a careful mesh density convergence study conducted previously, which can be found in the supplemental materials of chapter 2 (appendix A). All three computational fluid dynamics models consisted of approximately 23 million finite volume cells (Table 1). In order to obtain a comprehensive estimation of drag and other hydrodynamic forces for each NARW model, 12 flow speeds (0.125-8 m/s) were tested separately. In addition, I used a flow speed of 2 m/s for comparative

examination of the hydrodynamic properties of the three models. The average solution time was approximately 4 h per half-domain and 10 h per full-domain simulations on an 80-processor workstation with 256 GB of RAM.

### **3.3 Results**

Parallel simulations of 11 flow speeds for each NARW model were undertaken in a half domain with a symmetry condition applied at the midplane in order to reduce CFD computational expense, whereas an additional simulation of a flow velocity at 2 m/s was conducted in full domain with each of the three models. The difference in drag estimations between half- and full-domain simulations were less than 0.5% for all three models (Table 3.2) as would be expected due to lateral symmetry.

#### **3.3.1 Reynolds number and drag**

The results show that Reynolds number and drag fit to a quadratic polynomial model (Figure 3.3a, hollow squares;  $R^2=1$ ) for all three NARW models. I found the pregnant NARW model had the largest surface area (51.05 m<sup>2</sup>) and the highest drag under almost all flow speeds (Table 3.1 and Figure 3.3a, blue hollow squares), followed by the normo-nourished and the emaciated models (Figure 3.3a, green and red hollow squares, respectively). Nevertheless, the emaciated NARW model encountered the highest dimensionless drag, or drag coefficient, across the flow speeds (Figure 3.3a and 3.3b, red hollow circles). This seeming disparity in the results may be understood when one realizes the surface area of all

three animal models is different and the surface area is used to calculate the dimensionless drag coefficient.

### **3.3.2 Boundary layer thickness and type**

I found overall a thin boundary layer ( $< 0.115$  m) in regions of increasing animal cross-sectional area and thickening boundary layer ( $> 0.115$  m) around its peduncle (Figure 3.4, left panel). The thickest boundary layer was found at the side of the tail stock for all three models. Both normo-nourished and emaciated NARW models had their maximum boundary layer thickness at approximately 23 cm, while the pregnant model had its maximum boundary thickness measured at about 20 cm. Boundary layer close to the tip of rostrum, flippers, and flukes was the thinnest.

As shown in the right panel of Figure 3.4, laminar flow (blue) shifted to fully turbulent flow (red) after it passed the maximum body diameter of the animal. However, a delayed occurrence of turbulent flow was observed on the pregnant NARW model. On the pregnant NARW model, the transitional flow appeared at approximately 0.7 LOA and the fully turbulent flow occurred at 0.8 LOA. On the other hand, both normo-nourished and emaciated models had their transitional and fully turbulent flows developed at 0.6 and 0.7 LOA, respectively. Lastly, I found the boundary layer thickness slightly increased within the post-nuchal concavity of the emaciated NARW model. However, the flow remained laminar in the concavity.

It is important to note that both the boundary layer thickness and the boundary layer type vary with Reynolds number. The results reported in this section are for a far-field flow speed of 2 m/s which corresponds to a Reynolds number of  $1.97 \times 10^7$ . With increasing flow speed, it was expected the region of laminar – turbulent boundary layer transition to move forward and a thinning of the boundary layer. However, a detailed investigation of these effects was not undertaken in this study.

Table 3.2 CFD simulation results in half and full domains.

	CPU time		Drag <sup>‡</sup> (N)		
	Full domain	Half domain	Full domain	Half domain	Difference <sup>+</sup>
Normal-nourished	10:35:06	4:00:47	598.738	598.318	-0.07 %
Emaciated	10:43:06	4:19:31	599.791	599.352	-0.07 %
Pregnant	10:08:13	4:17:58	610.381	607.600	-0.46 %

\*simulated at a flow speed of 2 m/s  
<sup>‡</sup>calculated by:  $(\text{drag}_{\text{Full}} - \text{drag}_{\text{Half}}) / \text{drag}_{\text{Full}}$

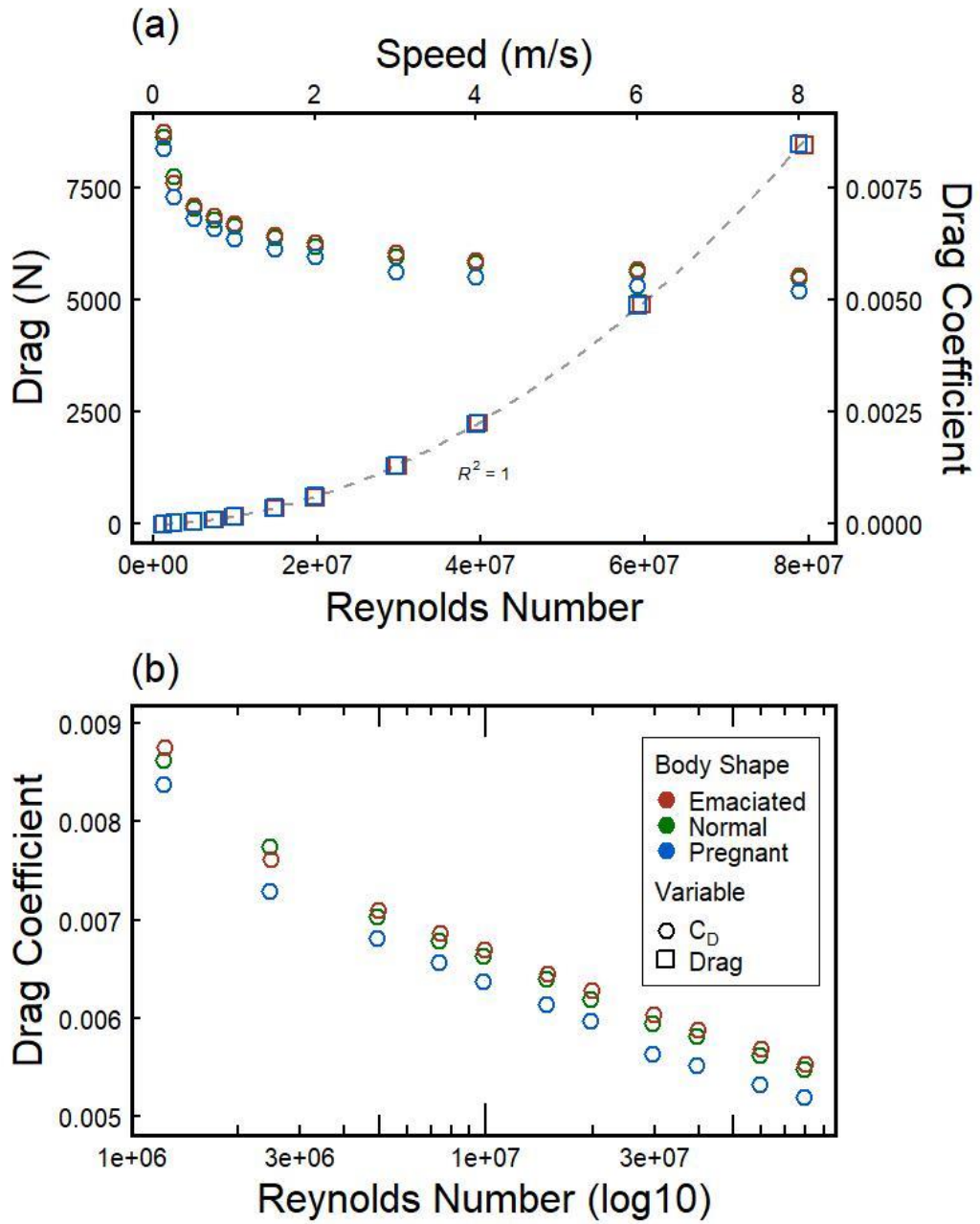


Figure 3.3 Drag and drag coefficient as a function of Reynolds number. The pregnant NARW had the largest surface area and drag but the emaciated NARW encountered the highest drag coefficient (a). Drag coefficient was found not strongly dependent on Reynolds number (b).

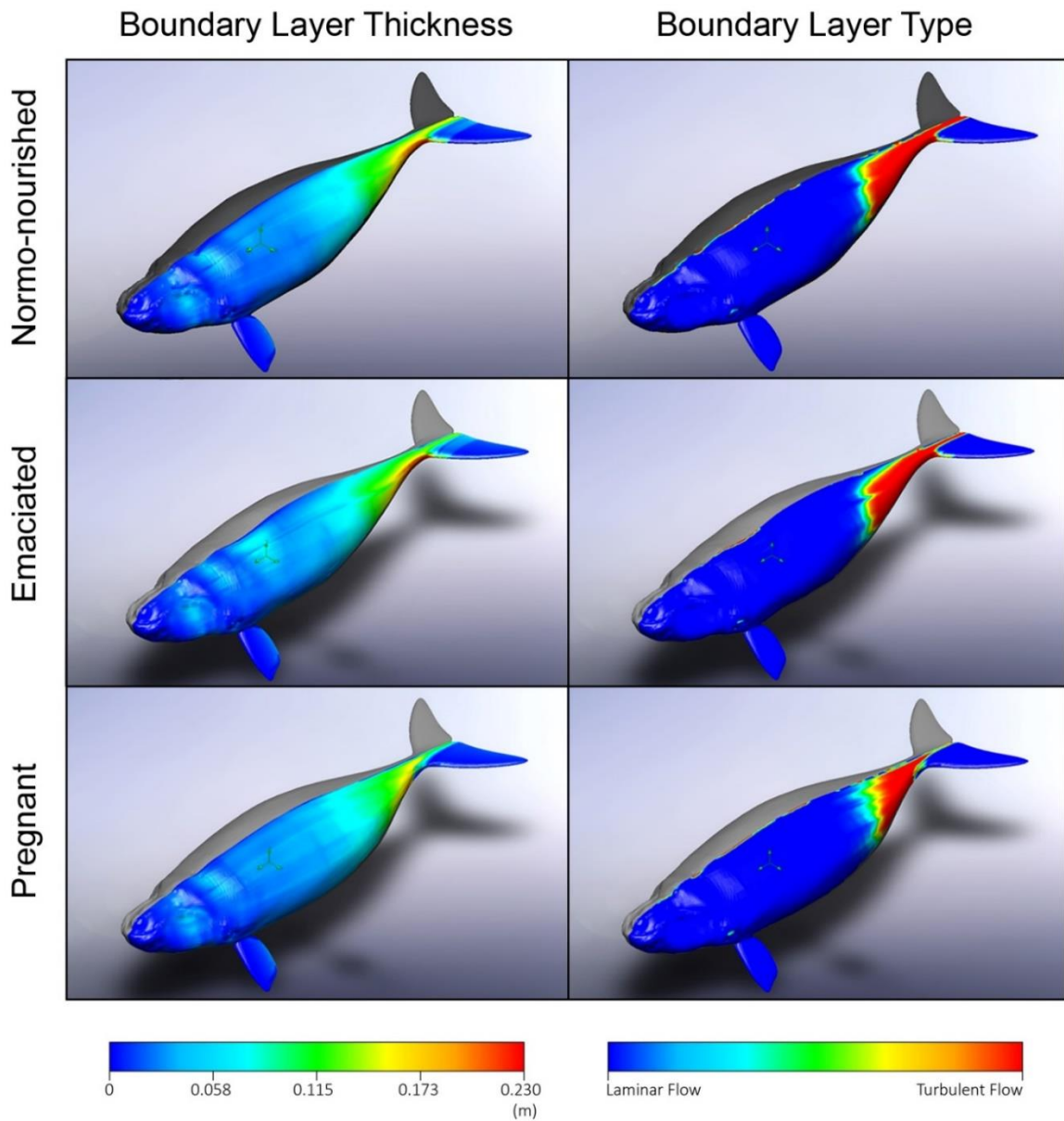


Figure 3.4 Boundary layer thickness and type. The thickest boundary layer, in red, appeared at the side of the tailstock for all cases. However, fully turbulent flow occurred at 0.8-0.9 LOA on the pregnant NARW, while it occurred at 0.7-0.8 LOA on the other two models.

### **3.3.3 Shear stress, drag, and total pressure**

Distributions of shear stress, form drag, and total pressure on different body shapes are shown in Figure 3.5a, respectively from left to right columns. Note that the shading is inverted for form drag because it is in the negative coordinate direction of the flow domain. Similar to the results of chapter 2, I found that 1) higher shear stress, form drag, and pressure appeared at the head and leading edge of appendages, 2) highest pressure occurred at the tip of the rostrum (i.e., the stagnation point), and 3) distributions of forces on the head corresponded to the irregular head shape of the NARWs.

Drag distribution of the emaciated NARW model is labelled with a yellow star and enlarged in Figure 3.5b. As shown in Figure 3.5b, drag per unit surface area within the concavity is approximately 10 Pa higher than the corresponding region on the other two NARW models. Namely, the post-nuchal concavity on a gliding NARW could have increased form drag by 10 N/m<sup>2</sup>.

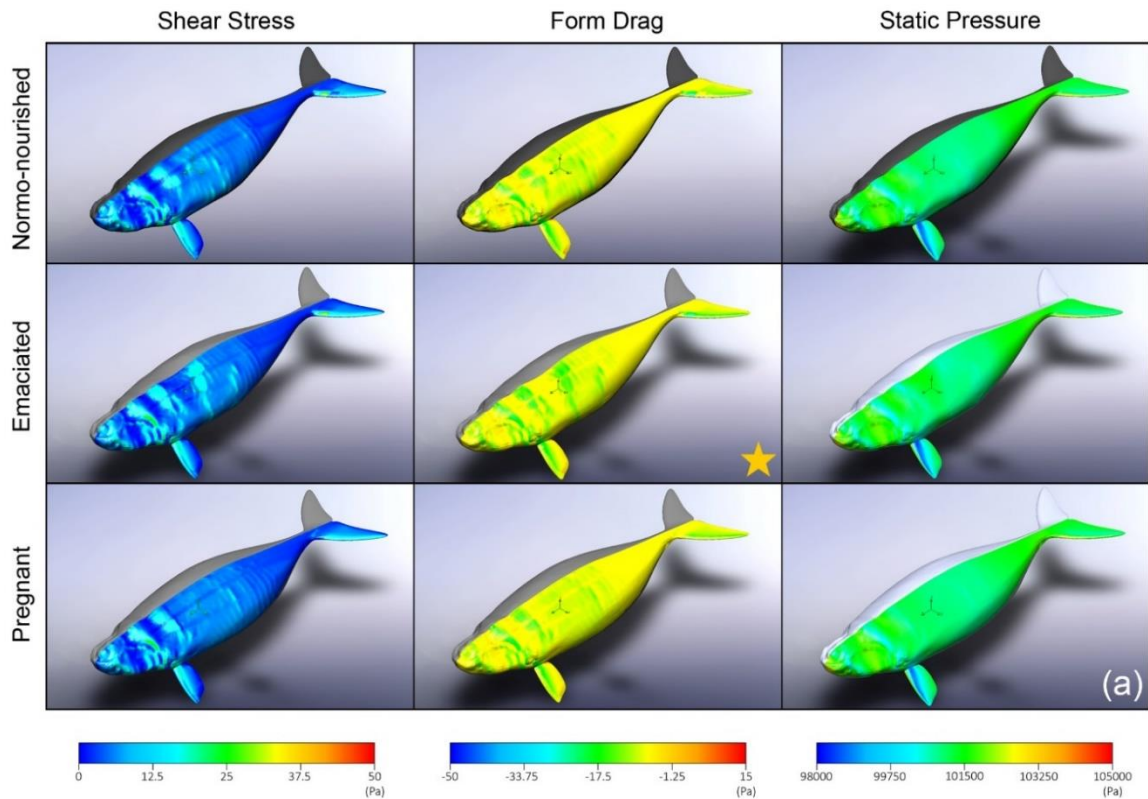
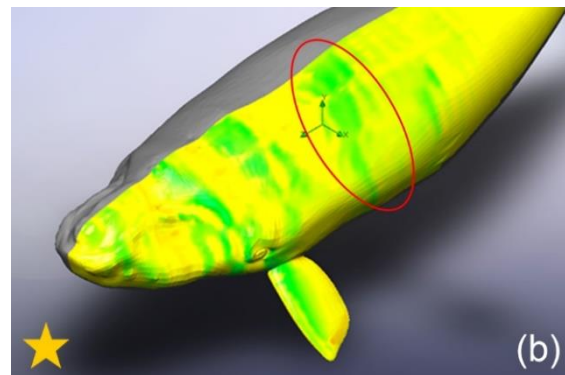


Figure 3.5 Shear stress, form drag, and total pressure on three models. Higher shear stress and form drag appeared at regions facing the incoming flow, whereas highest total pressure occurred at the tip of the rostrum and the leading edge of appendages (e.g., flippers and fluke). While the distribution of shear stress, form drag, and the total pressure were similar between three models (a), the emaciated NARW (labelled with a yellow star) had relatively higher form drag at its post-nuchal region (circled in Figure 3.5b).



### 3.3.4 Locomotor cost of gliding NARWs

Thrust power and locomotor cost of a gliding NARW can be estimated with equation 3.6 and 3.7, respectively. To be consistent with previous studies, the unit of locomotor cost estimated by present models was converted from joules to calories with equation 3.8. Based on the model, the thrust power required by gliding NARWs with various body shapes increased from  $8473 \pm 109$  cal/d to  $1.40 \times 10^9 \pm 2.24 \times 10^6$  cal/d across the flow speeds tested (Table 3.3 and Figure 3.6a). The association between thrust power requirement and speed is significant for all three NARW models (Spearman's  $\rho = 1$ ,  $p$ -value  $< 0.01$ , Table 3.4). By comparing the emaciated and the pregnant NARW models with the normo-nourished animal, I found that changes in required thrust power ranged from  $-2.78\%$  to  $0.42\%$  (mean =  $-0.23\% \pm 0.87\%$  *SD*;  $n = 11$ ) for the emaciated NARW model and from  $-0.86\%$  to  $2.44\%$  (mean =  $0.87\% \pm 1.17\%$  *SD*;  $n = 11$ ) for the pregnant NARW model (Figure 3.6b). Additionally, those changes, possibly due to deformed body shapes, are larger when the CFD models were simulated at lower flow velocities (Figure 3.6b).

Table 3.3 Locomotor power requirements of gliding NARWs.  $\overline{P_T}$  and  $\sigma_{P_T}$  are the mean and standard deviation of the power requirement of the three NARW models, respectively.

Speed (m/s)	Power (cal/day)				
	Normal-nourished	Emaciated	Pregnant	$\overline{P_T}$	$\sigma_{P_T}$
0.125	$8.39 \times 10^3$	$8.43 \times 10^3$	$8.60 \times 10^3$	$8.47 \times 10^3$	$1.09 \times 10^2$
0.25	$6.03 \times 10^4$	$5.87 \times 10^4$	$5.98 \times 10^4$	$5.96 \times 10^4$	$8.59 \times 10^2$
0.5	$4.38 \times 10^5$	$4.37 \times 10^5$	$4.48 \times 10^5$	$4.41 \times 10^5$	$5.78 \times 10^3$
0.75	$1.43 \times 10^6$	$1.43 \times 10^6$	$1.46 \times 10^6$	$1.44 \times 10^6$	$1.72 \times 10^4$
1.0	$3.31 \times 10^6$	$3.30 \times 10^6$	$3.35 \times 10^6$	$3.32 \times 10^6$	$2.47 \times 10^4$
1.5	$1.08 \times 10^7$	$1.07 \times 10^7$	$1.09 \times 10^7$	$1.08 \times 10^7$	$9.00 \times 10^4$
2.0	$2.47 \times 10^7$	$2.48 \times 10^7$	$2.51 \times 10^7$	$2.49 \times 10^7$	$2.10 \times 10^5$
3.0	$8.01 \times 10^7$	$8.04 \times 10^7$	$8.00 \times 10^7$	$8.01 \times 10^7$	$2.00 \times 10^5$
4.0	$1.86 \times 10^8$	$1.86 \times 10^8$	$1.85 \times 10^8$	$1.86 \times 10^8$	$1.12 \times 10^5$
6.0	$6.06 \times 10^8$	$6.05 \times 10^8$	$6.04 \times 10^8$	$6.05 \times 10^8$	$7.82 \times 10^5$
8.0	$1.40 \times 10^9$	$1.39 \times 10^9$	$1.40 \times 10^9$	$1.40 \times 10^9$	$2.24 \times 10^6$

Table 3.4 Results of Spearman correlation test. The monotonic relationship between flow velocity and locomotor power requirement was tested in R.

	Normal-nourished	Emaciated	Pregnant
Spearman's $\rho$	1	1	1
$p$ -value	< 0.01	< 0.01	< 0.01

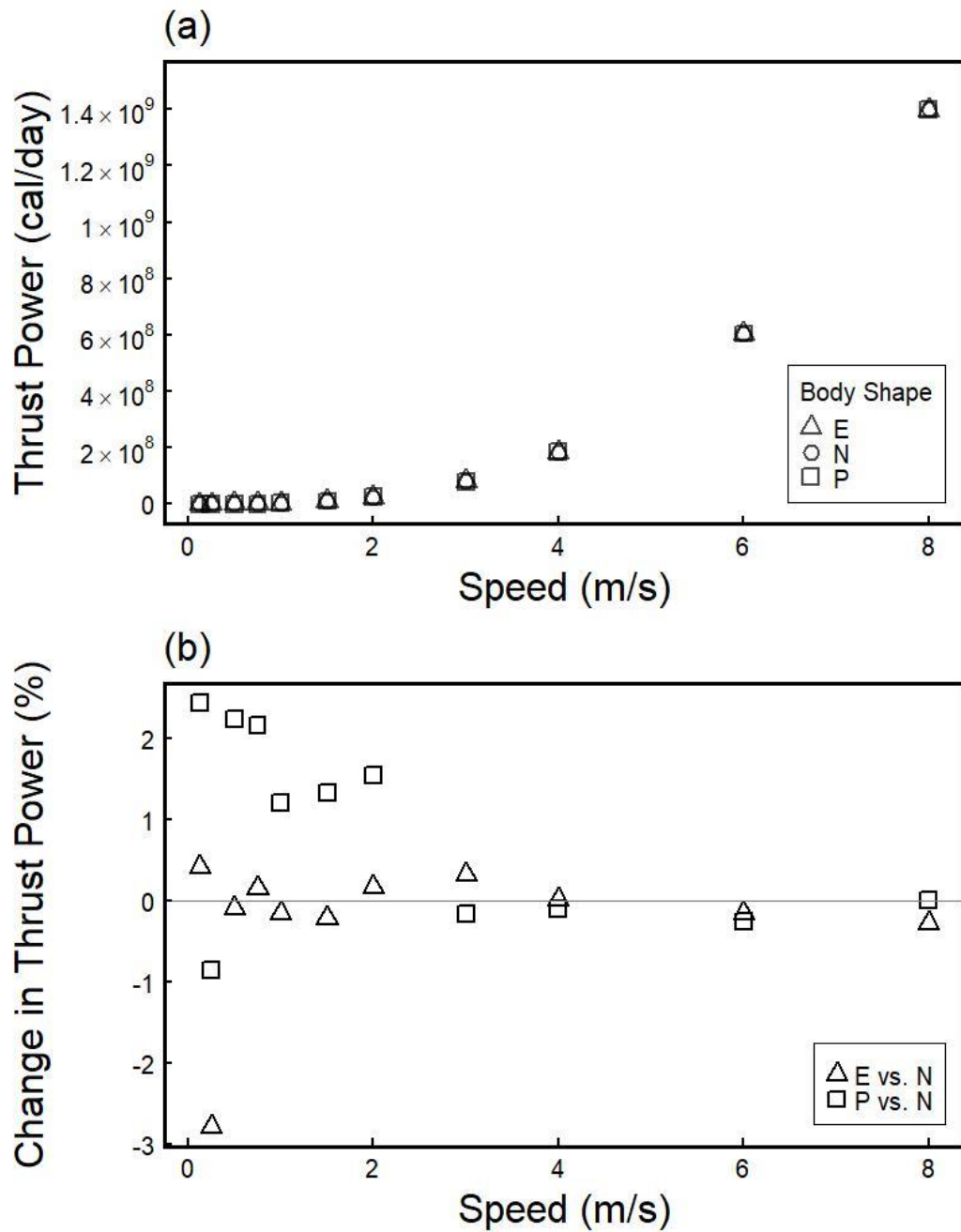


Figure 3.6 Thrust power requirement of NARWs with different body shapes. The thrust power required by three NARW models have similar trends (a). However, the power requirement is more divergent at flow speeds < 4 m/s (b).

### ***3.4 Discussion***

#### **3.4.1 Hydrodynamic performance of the three NARW models**

The three-dimensional NARW models included detailed outlines of a NARW's head (e.g., callosities and jaw lines) with a closed mouth. Through CFD simulations I found that those features affected not only the boundary layer thickness but also hydrodynamic forces on the animal models. The boundary layer thickness increased along the surface of callosities and blow holes, then decreased to the initial thickness after passing those elevated features. Despite having an irregular head shape, CFD results suggest that flow became laminar again along the body after being disturbed by the outlines of NARW's head.

In laminar flow, fluid elements move along smooth streamlines. Whereas in turbulent flow, fluid elements are circulating in chaotic directions and therefore create higher drag (Anderson 2010). The pregnant NARW model has its maximum body diameter measured farthest from the snout among all three models. In addition, the overall larger body width of the pregnant NARW model, especially its diminishing body part (40-80% LOA), suggests that it can maintain a favorable pressure gradient. In other words, the occurrence of the adverse pressure gradient that trips flow separation on the surface was delayed (Anderson 2010). On the other hand, with a more slender body shape at 40-80% LOA, both normo-nourished and emaciated NARW models create unfavorable pressure gradient and thus the boundary layer is relatively unstable. Therefore, turbulent flow on the

pregnant animal requires longer time to develop owing to its enlarged girth of the abdomen when in comparison to the other two body shapes. This phenomenon may explain why the pregnant NARW encountered lowest drag coefficient. Besides, the post-nuchal concavity on the emaciated NARW model made it less streamlined and suffered additional drag. Our findings indicate that drag on NARWs does vary with body shapes. However, the differences between the three NARW models tested were small, which may be because they all have similar fineness ratio. All of the fineness ratios are close to the optimum of 4.5 for providing minimal drag while moving in fluid (Webb 1975).

The dimensional drag of the pregnant NARW model calculated by the CFD simulations suggests that additional drag related to pregnancy could be as high as 2.44 % in comparison to the normo-nourished model. This value is in agreement with increased hydrodynamic drag of pregnant NARW estimated by Nousek-McGregor (3-4 %; Nousek-McGregor 2010). Inconsistency between previous and current studies may come from 1) differences in LOA and grid size of the NARW models tested or 2) different regime (e.g., turbulent or non-turbulent model) used by CFD solutions, or both.

### **3.4.2 Cost of locomotion of gliding NARWs**

Even though it is nearly impossible to measure the basal metabolic rate of the NARWs *in situ*, Nousek-McGregor (2010) calculated the overall energy expenditure of a NARW during a 4-month foraging season is approximately  $6.98 \times 10^7$  cal/d) with kinematic data recorded by animal-borne tags. Results from van

der Hoop *et al.* (2014) indicate that the total power requirements of a nonentangled NARW can vary from  $5.76 \times 10^7$  to  $1.20 \times 10^8$  cal/d as the swimming speed increased from 0.75-2.9 m/s. In addition, van der Hoop *et al.* estimated that a NARW may expend  $7.89 \times 10^7$  cal/d of energy during a 22-day, one-way migration with an average speed of 1.5 m/s (van der Hoop *et al.* 2014b). Assuming a NARW swims at 1 m/s during foraging dives (Baumgartner and Mate 2003), the CFD simulations suggest that this animal has to increase the thrust power from approximately  $3.30 \times 10^6$  cal/d (normo-nourished and emaciated animals) to  $3.35 \times 10^6$  cal/d (pregnant animal) to overcome drag and keep itself at a steady speed. This implies that the inflated abdomen of a pregnant NARW may lead to a 1.21 % increase in its thrust power requirement, which equals 0.068 % daily energy budget as estimated by Nousek-McGregor (2010). However, given the lengthy gestation period and the timeframe of calving season of NARWs (Lockyer 1984, Kraus *et al.* 1986), it is unlikely that pregnant NARWs will be bearing a fully inflated abdomen during the summer foraging season. Accordingly, the effects of decreased body fitness on the hydrodynamic performance of NARWs may not be as high as estimations presented here. Similarly, for a female NARW swimming at 1.5 m/s during migration, the models reveal that there could be a 1.33% increase in required thrust power, which is equivalent to 0.18 % increase in total energy output estimated by van der Hoop *et al.* (2014b). Given that the estimated energy consumption rates of NARWs are  $1.74$ - $3.13 \times 10^8$  cal/d in Cape Cod Bay and  $3.42$ - $6.12 \times 10^8$  cal/d in Bay of Fundy (Fortune *et al.* 2013), the present model estimated

that thrust power variations due to altered body shapes prompt little difference in required foraging time (mean =  $-0.09\% \pm 0.32\%$  *SD*;  $n = 44$ ). Nonetheless, despite only minor increases in total energetic cost and required foraging time were predicted by CFD simulations, I would like to bring up that swimming kinematics are much more complicated in real situations (Lighthill 1969, Webb 1975, Fish 1993a, b, Drucker and Lauder 2002, Goldbogen et al. 2006, Liao 2007, Vogel 2008). For example, except for gliding, animals will also propel themselves by undulating and fluking, or adjust their appendages for maneuvering, etc. Accordingly, drag estimations for a gliding three-dimensional NARW model presented in this work should serve as a lower bound of increased drag when including body deformation.

### **3.4.3 Physiological recover of NARWs**

It is well documented that migratory large whale species show variations in body shape due to concurring foraging and fasting periods, reproductive status, and food abundance, etc. (Lockyer 1986, Reeves and Mitchell 1986b, Pettis et al. 2004, Bradford et al. 2012, Miller et al. 2012, Pettis et al. 2017b, Solvang et al. 2017). Pettis *et al.* (2004) used the relative amount of subcutaneous fat in the post-nuchal region of a NARW as an indicator for evaluating body condition of the NARWs. In a follow-up study, Pettis *et al.* (2017) evaluated changes in body condition of NARWs and found that the amount of time required by resting females and severely entangled individuals to recover from “fair” to “good” body conditions is comparable. Despite the fact that changes in body condition were

examined manually, which may incur bias when carrying out the task, their findings suggest that previously entangled NARWs might be able to naturally recover from non-desirable body fitness. However, variable body shapes of NARWs may not appear alone: effects of body deformation are possibly coupled with other factors such as health condition of the animal, injuries, and carrying fishing gear (Cassoff *et al.* 2011, Knowlton *et al.* 2012, Robbins *et al.* 2015). All of which may lead to decreased energy intake (e.g., inhibited foraging attempts, Cassoff *et al.* 2011) and lower its hydrodynamic performance (e.g., altered swimming behavior or increased drag, van der Hoop *et al.* (2017a, 2017b).

### **3.5 Conclusion**

This is the first study to provide insight in the effects of variable body shapes on hydrodynamic properties of the NARWs. My findings reveal that drag generated by a gliding NARW is influenced by its body shape, but the changes are minor. The emaciated NARW model encountered the highest drag coefficient, possibly due to the concavity at its post-nuchal region, whereas the pregnant NARW model experienced the lowest drag coefficient, possibly due to the delayed onset of turbulent flow. Furthermore, locomotor power estimated for the three NARW models show little variations, especially in comparison to the total energetic expenditure calculated for foraging and migrating NARWs by previous studies. Therefore, combining these results with findings from Pettis *et al.* (2017), deformed body shape may not serve as a major or single concern when one wants to investigate the energy budget of cetaceans. In other words, solely losing a

portion of subcutaneous fat or becoming pregnant, in which both lead to a modified body shape, will not substantially increase locomotor costs for NARWs. Other incidents which jeopardize the energy budget of NARWs, such as becoming entangled in fishing gear, should be considered while evaluating NARW population health.

# **Chapter 4 Minimal drag on a three-dimensional North Atlantic right whale model via neutral trim pose**

## ***4.1 Introduction***

Animals encounter hydrodynamic forces (lift, drag, side) and moments (pitching, yawing, rolling) while they move underwater (Webb 1975, 1988, Vogel 1994). In order to live in an aqueous medium with high density and viscosity, streamlining is a key advantage that helps aquatic animals to minimize energy expenditure through reducing drag, delaying flow separation, and minimizing excess fluid momentum from parasitic loads (Lighthill 1969, Webb 1984, Fish and Hui 1991, Fish 1993a, Vogel 1994). Aside from morphological evolution, it has been well-documented that animals develop a variety of strategies to reduce energy expenditure, in both terrestrial and aquatic environments. Some behaviors to minimize drag include formation flight in some bird species (Lissaman and Shollenberger 1970, Cutts and Speakman 1994, Weimerskirch et al. 2001), echelon formation associated with foraging in large whales (Fish et al. 2012), fish schooling (Liao 2007, Weihs and Farhi 2017), drafting, porpoising, and bow-riding of dolphins (Williams et al. 1992a, Weihs 2004, Weihs and Farhi 2017), stroke-and-glide swimming gait observed in marine mammals (Williams et al. 2000, Nousek-McGregor et al. 2014), and keeping a relatively stable Strouhal number while cruising (Taylor et al. 2003, Rohr and Fish 2004, Gazzola et al. 2014, Floryana et al. 2018). These behavioral adaptations have been linked with stability and energy expenditure minimization during flight or swimming.

Drag on the animal, which is a key variable when calculating cost of transport (COT), has various forms. In addition to pressure and viscous drag that are associated with the shape and surface area of the animal and fluid properties, extra momentum imparted into the fluid from lift and side forces as well as pitching, yawing, and rolling moments (here, the parasitic loads) results in extra drag on the animal (Webb 1988). Aquatic animals utilize their control surfaces such as fins, flippers, and flukes to generate lift as well as propel, glide, and maneuver in the surrounding fluids (Webb 1984, Triantafyllou et al. 2000, Webb and Weihs 2015, Payne et al. 2016, Fish and Lauder 2017), which also promote stabilization and maneuverability as necessary (Fish 2002, Webb 2004, Fish and Lauder 2006, Fish et al. 2008, Triantafyllou 2017). Although control surfaces of the animals enhance their swimming performance, such platforms also create additional fluid momentum imparted to the wake and thereby increase COT if animals are not in their neutral trim pose (Webb 1988, 2002).

To explore the increased energetic costs associated with moving through water, various studies have assessed the energetics (e.g., metabolic cost, COT, body condition, etc.) and swimming performance of aquatic animals through different approaches, including analyzing video footage of trained animals (Lang and Daybell 1963, Lang and Pryor 1966, Feldkamp 1987, Fish 1993b, 1998, van der Hoop et al. 2018, Zhang et al. 2019) or animals that were retained in a flow tank (Lauder and Drucker 2002), recording the kinematics of marine mammals through digital tags (Miller et al. 2004, Goldbogen et al. 2006, Goldbogen et al.

2007, van der Hoop et al. 2014a, van der Hoop et al. 2014b, van der Hoop et al. 2018) or animal-borne cameras (Williams et al. 2000), estimating the locomotor cost via visual observation (Sumich 1983, Williams and Noren 2009), and measuring the oxygen consumption rate of studied animals with pneumotachometer or respirometry (Williams et al. 2004, van der Hoop et al. 2018). Together these studies highlighted a broad interest in understanding the hydrodynamics of underwater movement. However, unlike fish, pinnipeds, and small cetaceans that can be measured in laboratories or captive environments for more accurate energetic costs (Lang and Pryor 1966, Feldkamp 1987, Fish et al. 1988, Fish 1993b, 1998, Drucker and Lauder 2000, Fish et al. 2014, van der Hoop et al. 2014a), it is exceptionally difficult to access large whales due to their body size and remote habitats. Therefore, what is known about the metabolic and locomotor costs of large whales are mostly estimates from values established for smaller marine mammal species. Therefore, I chose a computational fluid dynamic (CFD) approach for investigating the hydrodynamic properties of one large whale species. One advantage of using numerical method is that the morphometric parameters of the three-dimensional animal model can be precisely measured, those measurements are essential while calculating hydrodynamic forces on the animal (Lauder 2011). Another advantage of using computer solutions for hydrodynamic analysis is that it allows us to run parallel simulations under a controlled circumstance such as modifying one variable at a time (Shorter et al.

2014). By doing so, I was able to focus on the outcomes influenced by each parameter.

Analyzing hydrodynamic properties of the North Atlantic right whale (NARW) is of interest because there is an urgent need to protect this species. The abundance and health of the NARW is declining and this population could become functionally extinct in decades if they continued to be unintentionally injured and/or killed by anthropogenic activities such as vessel collision and fishing gear entanglement (Caswell et al. 1999, Knowlton and Kraus 2001, Knowlton et al. 2012, Knowlton et al. 2016, Kraus et al. 2016, Daoust et al. 2017, Pace et al. 2017, Corkeron et al. 2018, Christiansen et al. 2020). Research has also shown that the NARW are switching their habitats in order to adapt to the changing ocean environment (Davis et al. 2017, Davies et al. 2019, Record et al. 2019), and these movements can make them more vulnerable as they move to areas that do not carry protections for them.

In chapter 2 and 3, I found that drag on NARWs is higher than any other measured large whale species. Although one needs to be cautious when comparing hydrodynamic forces measured with different approaches, this finding drove me to contemplate how I could increase the accuracy of drag estimations while using numerical solutions. Here, I considered drag to be not only a function of body shape and flow regime but also a function of parasitic loads. Therefore, the goal of the present study was to find the neutral trim pose of the NARW model by eliminating parasitic loads.

## **4.2 Methods**

### **4.2.1 Three-dimensional NARW model**

A three-dimensional NARW model was adapted from chapter 2, though for those studies it was positioned at its presumed gliding/resting pose. However, the prescribed body position may not necessarily provide the minimal drag on the animal model. For example, in chapter 2 and 3 the flipper was aligned parallel with the far field flow vector. It seems a reasonable assumption that this orientation would minimize the drag of this appendage and thus contribute to minimization of the drag on the animal as a whole. However, the modification of the local fluid velocity vector (both flow speed and direction) caused the distortion of streamlines as a result of flow around the body modifies the local flow conditions experienced by the flipper. So, the minimum drag orientation might not necessarily correspond to alignment with the far field flow vector but instead correspond with alignment with the *local* flow vector. Therefore, it is important to identify the optimum body pose that creates minimal drag and moments. In order to execute different body poses, the mesh model was embedded with multiple bone segments that allow us to rotate its joints in certain dimensions. A detailed description on how the whale geometry was manipulated can be found in Howle et al. (2018)

### **4.2.2 Hydrodynamic properties**

For reporting dimensionless lift and drag, I used lift coefficient ( $C_L$ ) and drag coefficient ( $C_D$ ), which can be calculated by

$$C_L = \frac{L}{qS} \quad (4.13)$$

$$C_D = \frac{D}{qA} \quad (4.2)$$

where  $L$  is lift,  $D$  is drag,  $q$  is the dynamic pressure,  $S$  and  $A$  are the surface area and surface area of the NARW model, respectively. The dynamic pressure is given by

$$q = \frac{\rho U^2}{2} \quad (4.3)$$

where  $\rho$  is the fluid density and  $U$  is the flow speed. Additionally, the lift-to-drag ratio ( $C_L/C_D$ ) was used to report hydrodynamic efficiency of the animal model (Anderson 2010).

Figure 4.1 shows the NARW model positioned at the initial body pose with circular arrows indicating the direction of pitching, rolling, and yawing moments. The model will be forced to rotate about three axes if at least one of the moments is non-zero. The pitching moment coefficient ( $C_M$ ) was used to estimate pitching moment provided by the NARW model, which can be calculated by

$$C_M = \frac{M}{qSc} \quad (4.4)$$

where  $M$  is the pitching moment,  $q$  is the dynamic pressure,  $S$  is the projected area (body shape projected onto the horizontal plane) of the NARW model, and  $c$  is the length of the animal.

In this work, the fluid density is 997 kg/m<sup>3</sup>, the projected area of the animal model is 16.88 m<sup>2</sup>, the surface area of the animal model is 48.42 m<sup>2</sup>, and the length of the animal is 9.89 m. The projected area, surface area, and the length of the

animal were measured by the SolidWorks package. Calculating those dimensionless parameters allowed me to compare between each simulation and also allowed for easy conversion between fluid properties for freshwater (used for convenience in this calculation) and seawater.

In these studies, all moments were calculated about the center of gravity of the animal which was placed at the origin of the computational domain. Slight changes in the location of the center of gravity for the small changes in pose considered in this study result from changes in the whale's pose. For each simulation, the center of gravity was moved to the global origin of the computational domain and moments were calculated from the global coordinate system.

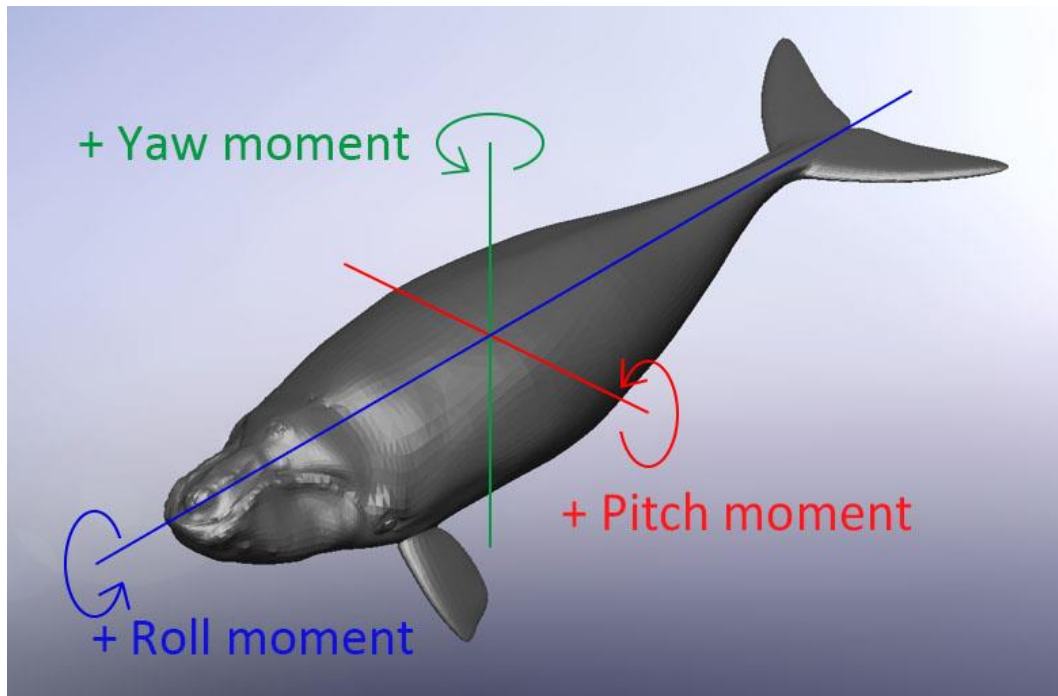


Figure 4.1 Three-dimensional NARW model. The pitching, rolling, and yawing directions about the three axes were labelled on the model.

Table 4.1 NARW model position setup. A list of adjusted parameters for CFD simulations on different animal body poses.

Scenario	Angle adjustment			Total # of simulation
	Flipper pitch angle*	Flipper dihedral angle <sup>‡</sup>	Spine position <sup>+</sup>	
Flipper pitch	-10° to 10° at every 2-degree interval	0°	0°	11
Total spine pitch	Result from <i>flipper pitch</i> scenario	0°	0° to 10° at every 1-degree interval	11
Flipper dihedral and pitch	-12° to 24° at every 4-degree interval	20°	Result from <i>total spine pitch</i> scenario	10

\*the angle of attack facing incoming flow  
<sup>‡</sup>adjusted from the resting position (45°)  
<sup>+</sup>adjusted from the resting position (0° = horizontal tailstock)

### **4.2.3 Animal model adjustments**

Three scenarios, including 1) adjusted flipper pitch angle, 2) adjusted total spine pitch angle, and 3) adjusted flipper dihedral and pitch angles were tested (Table 4.1). At the end of each scenario, I analyzed the results and applied the optimum position of the body part(s) to the subsequent simulations. By doing so, I aimed to diminish the effect of each variables and obtain the minimal drag and pitching moment estimations. However, due to the computational complexity and expense of each simulation, only one variable was adjusted at a time and it was assumed that changes in one of these scenarios did not affect the other. In other words, after optimizing one of the scenarios (scenario 1, flipper pitch angle, for example), and then using that input to optimize the next scenario (scenario 2, total spine pitch angle in this example), I did not go back and then reoptimize the first scenario. This is equivalent to making the assumption that the Hessian matrix of the optimization hyper surface has orthogonal or nearly orthogonal eigenvectors. This assumption is only approximately appropriate in this case. As shown below, by changing the pitch angle of the flippers in order to eliminate lift, the pitching moment of the whale is affected due to the flipper's location forward of the center of mass. Conversely, changing the total angle has only a weak influence on the lift.

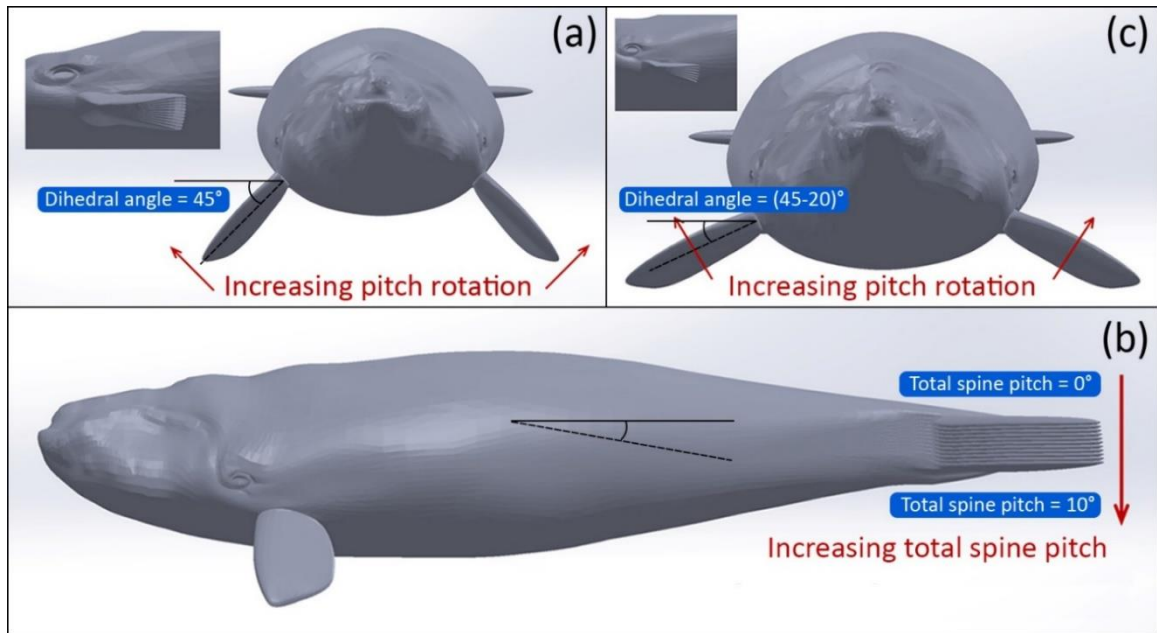


Figure 4.2 Animal pose adjustments. Flipper pitch angle (a), total spine pitch angle (b), and flipper dihedral and pitch angles (c) were adjusted accordingly to identify the minimal drag pose of the 3-D NARW model.

### Scenario 1: Flipper pitch study

The flipper pitch angle of the NARW model, or the angle of attack of the whale flippers ( $\alpha$ ), was modified from  $-10^\circ$  to  $10^\circ$  at every 2-degree interval (Figure 4.2a). The initial flipper pitch angle was  $0^\circ$ . By increasing the flipper pitch angle, the left and the right flippers rotated simultaneously and were symmetrical about the animal's midline.

### Scenario 2: Total spine pitch study

Prior to performing CFD simulations on the NARW model with variable spine pitch angles, its flipper pitch angle was adjusted accordingly based on the results from scenario 1. The total spine pitch angle, which stands for the sum of the

pitch angle of four spine segments, was modified from  $0^\circ$  to  $10^\circ$  at every 1-degree interval (Figure 4.2b). In my initial model setup, both the tailstock and the fluke platform of the NARW model were oriented parallel to the far field flow vector (i.e., the total spine pitch angle was  $0^\circ$ ). Increasing total spine pitch created a bending tailstock while the fluke platform remained unchanged. That is, with a total spine pitch angle changed by  $X$  degrees, the peduncle pitch (i.e., the fluke platform) was changed by  $-X$  degrees assuring the angle between the plane of the flukes and the far-field flow vector remained constant.

#### Scenario 3: Flipper dihedral and pitch study

In order to evaluate the effect of different flipper positions on drag, the flipper dihedral angle of the NARW model was decreased by  $20^\circ$  (i.e., the flippers became more horizontal; Figure 4.2c). In addition, I included the best estimate of the total spine pitch angle from scenario 2 to deminish pitching moment that may trigger drag panelty on the animal model. Similar to scenario 1, CFD simulations were conducted with the flipper pitch angle of the NARW model modified from  $-12^\circ$  to  $24^\circ$  at every 4-degree interval.

#### Scenario 4: Minimal drag pose speed sweep simulation

After CFD simulations on the NARW model with adjusted body positions (i.e., scenario 1-3) were completed, the optimum body pose that theoretically creates lowest drag and pitching moment was known. Per the test results, the flipper pitch angle, flipper dihedral angle, and total spine pitch angle of the NARW

model were manipulated correspondingly and a detailed CFD study was undertaken with the amended NARW model at 11 flow speeds.

#### **4.2.4 Numerical model**

The CFD simulations were performed with the SolidWorks Flow Simulation software package (Dassault Systemes SolidWorks Corporation, Waltham, MA) on an 80-processor workstation with 256 GB of RAM. The grid size of the NARW model and flow domain were determined after conducting a grid convergence study (refer to chapter 3 for the details.) Scenarios 1, 2, and 3 were simulated at a flow speed of 2 m/s, whereas the comprehensive minimal drag pose simulation was conducted at velocities covering known NARW swimming speeds from 0.125-8.0 m/s; consistent with my previous study. By using a consistent method, I was able to compare results between chapter 2 and current work. The flow speed of 2 m/s was selected as the speed was employed in tank experiment results in Weber et al. (2014) on forces created by varying pitch angle across a number of species and was also used in chapter 3 of this dissertation when comparing hydrodynamic forces experienced by NARWs with different body conditions (normo-nourished, emaciated, and pregnant).

### **4.3 Results**

Lift as well as five parasitic loads, including side force, drag, pitching moment, rolling moment, and yawing moment, were measured by the Solidworks software package for each scenario. Although the goal of this work is to eliminate the parasitic loads in order to find the neutral trim pose of the NARW model, side

force, rolling moment, and yawing moment remained zero due to symmetry in the animal model. Therefore, only the CFD results of lift, drag, and pitching moment are shown here.

### **4.3.1 Adaptive animal body pose adjustments**

I found that decreasing the flipper pitch angle of the NARW model by  $4.03^\circ$  creates the minimal drag on the animal and that increasing the spine pitch angle by  $5^\circ$  (i.e., making the spine slightly downswept thereby lowering the fluke) produced the minimal pitching moment on the animal. Therefore, in order to avoid overestimating hydrodynamic forces and moments, I used an updated flipper pitch angle of  $-4.03^\circ$  and an updated spine pitch angle of  $5^\circ$  for subsequent scenarios whenever applicable. Meanwhile, CFD simulations revealed that decreasing the flipper dihedral angle of the NARW model fails to lower drag on the animal. Therefore, the initial flipper dihedral angle was used for simulating hydrodynamic properties on the NARW model with the minimal drag pose (see descriptions below).

### **4.3.2 Lift provided by the NARW model**

The NARW model generated lift from  $-249.74$  N to  $1165.69$  N as flipper pitch angle increased from  $-10^\circ$  to  $10^\circ$ . I found that lift the coefficient is dependent on flipper pitch angle and their relationship is linear ( $R^2 = 0.97$ ; Figure 4.3a). While the NARW model generated lift from  $14.94$  N to  $107.55$  N (mean =  $139.93 \pm 54.66$  N,  $n = 11$ ) as total spine pitch increased from  $0^\circ$  to  $10^\circ$ , the lift coefficient is not dependent to total spine pitch angle ( $R^2 = 0.025$ ; Figure 4.3b). This finding implied

that fluking (i.e., actively swimming) is unlikely to alter the overall lift produced by the animal. Meanwhile, lift generated by the NARW model with decreased flipper dihedral angle ranged between  $\pm 1500.0$  N and it appears to have a slope similar to lift generated by animal without flipper dihedral angle adjustment ( $R^2 = 0.97$ ; Figure 4.3a), suggesting that the influence of reduced flipper dihedral angle on the lift production was minor. Within the range of pitch angles tested, no stall was observed.

### **4.3.3 Hydrodynamic drag on the NARW model**

As flipper pitch angle increased from  $-10^\circ$  to  $10^\circ$ , the NARW model created drag from 527.48 N to 1031.34 N. I found that drag coefficient on the NARW model and its flipper pitch angle fit to a quadratic equation ( $R^2 = 1$ ; Figure 4.4a) and the minimal drag appeared at a flipper pitch angle of  $-4.03^\circ$ . Similar to lift generated by the NARW model with a downswept tailstock, drag on such body pose remained relatively the same (mean =  $527.44 \pm 3.71$  N;  $n = 11$ ) and I found that drag coefficient is weakly dependent to spine pitch angle ( $R^2 = 0.63$ ; Figure 4.4b). For the NARW model with decreased flipper dihedral angle, drag provided by the model ranged from 548.37 N to 1058.38 N. The simulation results revealed that drag coefficient on the animal is dependent on its flipper pitch angle and the two variables fit to a quadratic equation ( $R^2 = 0.99$ ; Figure 4.4a). Within the range of flipper pitch angle tested, the NARW model with a decreased flipper dihedral angle generated the minimal drag at a flipper pitch angle of  $7.07^\circ$  in negative direction. However, because the minimal drag provided by the model with adjusted flipper

dihedral angle (scenario 3) was higher than the model without such adjustments (scenario 1), the latter body pose was considered in the neutral trim pose study (scenario 4).

#### **4.3.4 Pitching moment of the animal**

Because pitching moment induces the object to rotate clockwise or counterclockwise about the x-axis, the magnitude of pitching moment (i.e., its absolute value) was used for comparing pitching moment in either direction. For the NARW model with flipper pitch angle adjustment only, I found that pitching moment of the model is dependent on its flipper pitch angle in both directions ( $R^2 = 0.98$ ; Figure 4.5a) and the minimal pitching moment (65.25 Nm) appeared when the flipper pitch angle was increased by  $2^\circ$ . Therefore, as the flipper pitch angle increased from  $0^\circ$  to either direction (relative to free stream), the NARW model generated more pitching moment and tended to pitch up or down about its central of gravity. With a fixed flipper pitch angle, pitching moment generated by the animal in either direction is dependent to its total spine pitch angle ( $R^2 = 0.85$ ; Figure 4.5b) and the minimal pitching moment (25.33 Nm) appeared while the total spine pitch angle was increased by  $5^\circ$ . Likewise, pitching moment created by the NARW model with a decreased flipper dihedral angle is dependent to the flipper pitch angle ( $R^2 = 0.98$ ; Figure 4.5a). In this case, the minimal pitching moment (119.08 Nm) appeared at a flipper pitch angle of  $4^\circ$  in negative direction.

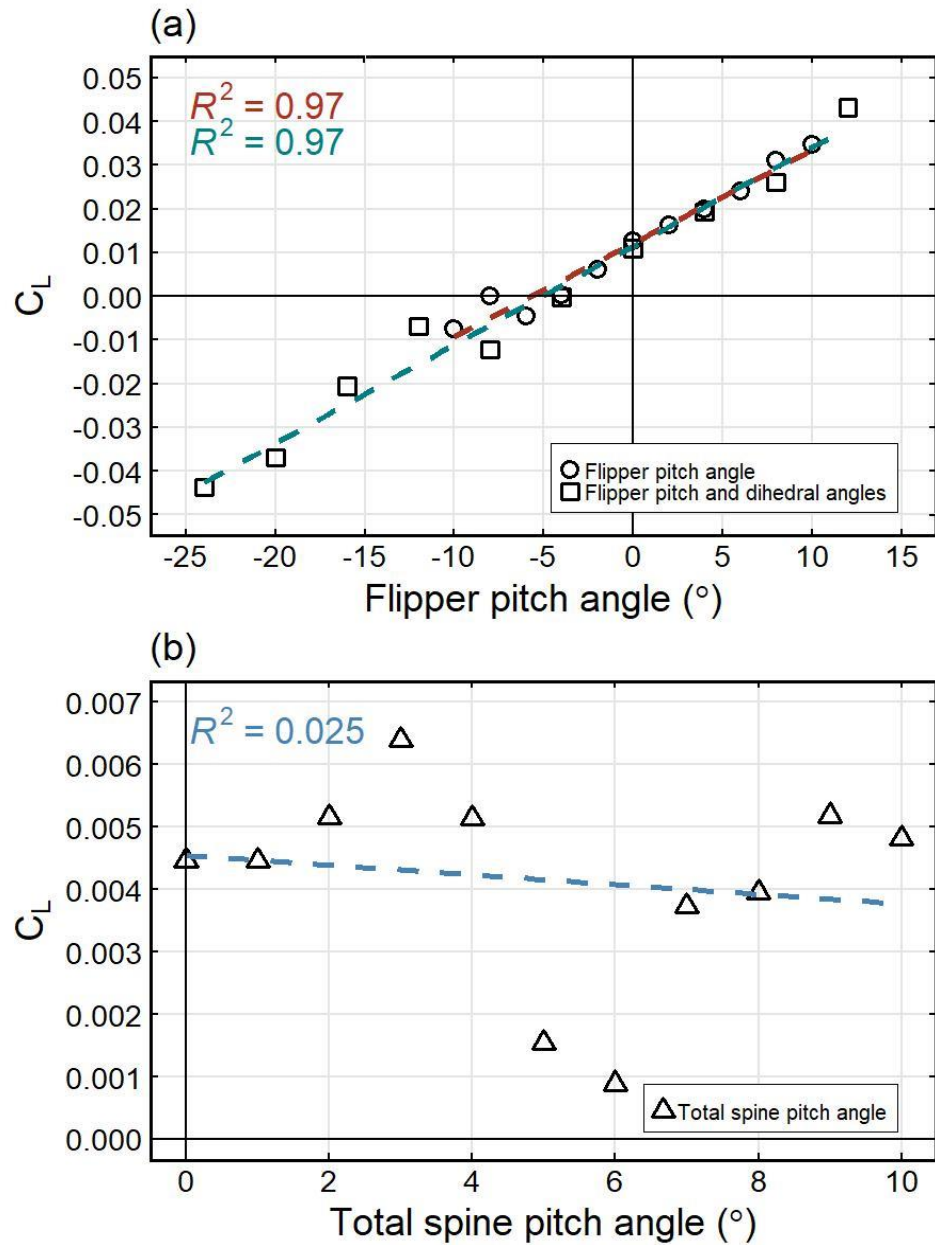


Figure 4.3 Lift coefficient associated with modified animal body pose. I found that  $C_L$  is correlated to the adjusted flipper pitch angle (a) but not spine pitch angle (b), and that lift produced by the NARW model was merely affected by the flipper dihedral angle (scenario 3).

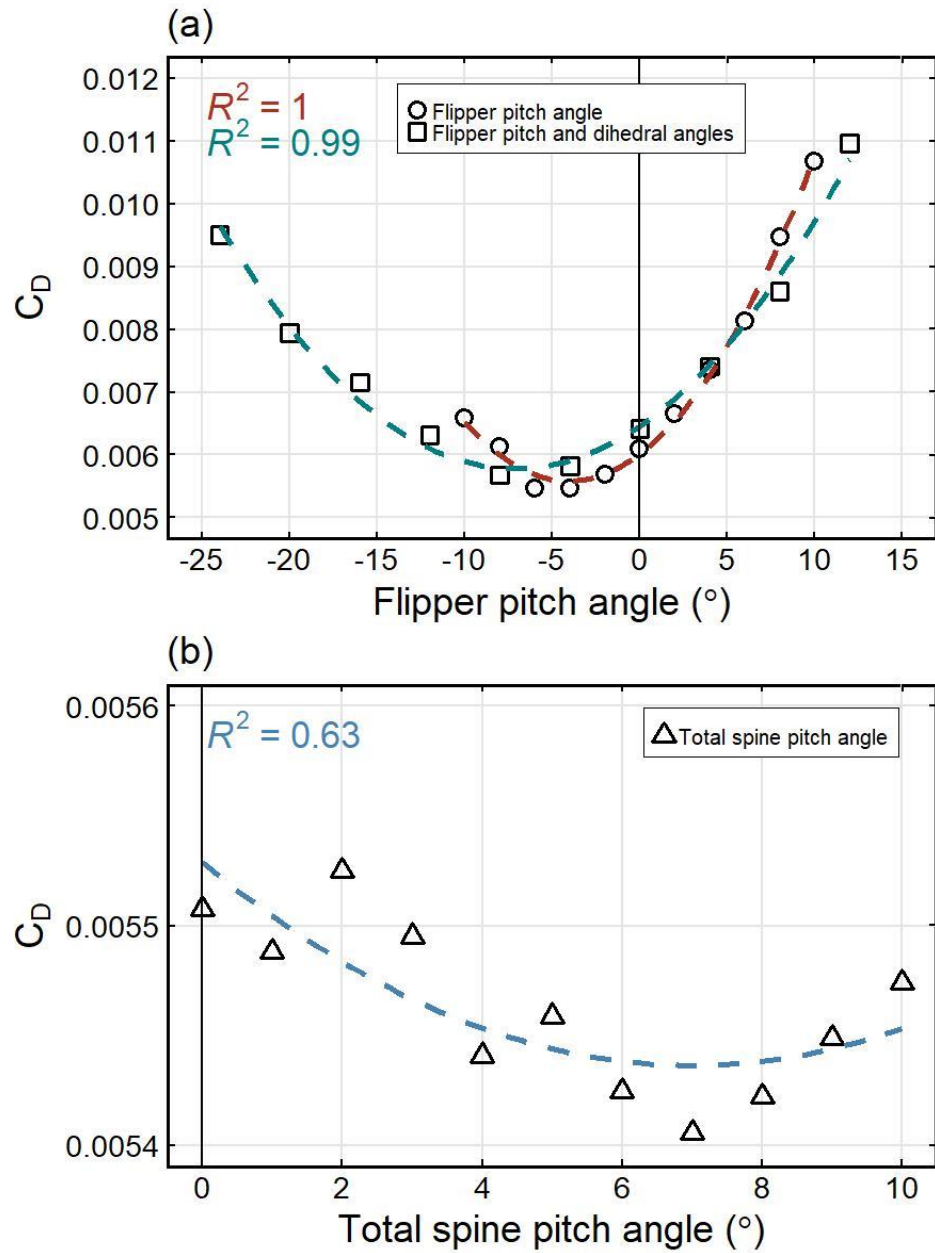


Figure 4.4 Drag coefficient associated with modified animal body pose. Minimal drag appeared when the flipper pitch angle was decreased by  $4.0315^\circ$  and the flipper dihedral angle remained  $45^\circ$  (a). I found that drag is not dependent to the total spine pitch angle (b).

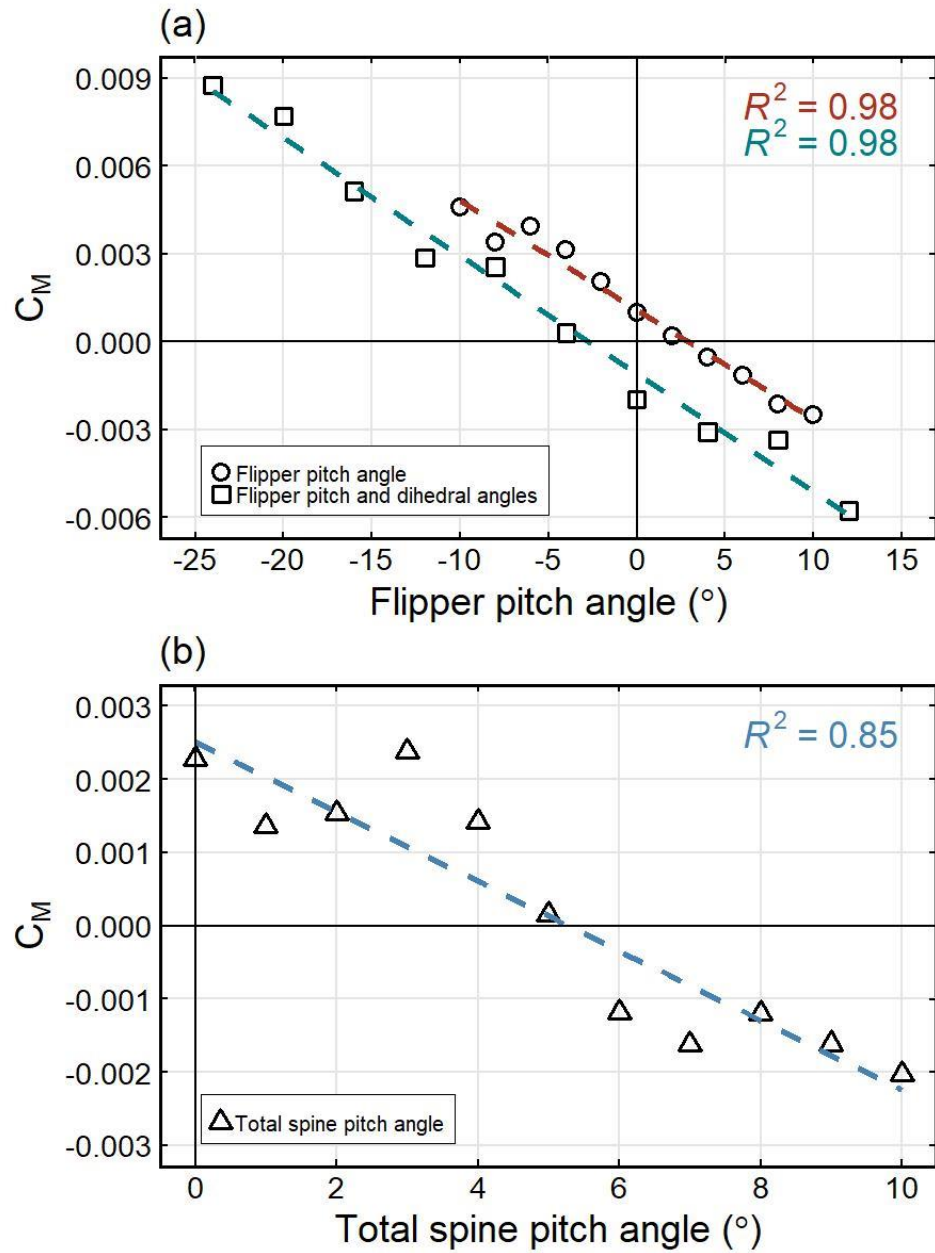


Figure 4.5 Pitching moment coefficient associated with modified animal body pose. Pitching moment of the model is dependent to its flipper pitch angle in either directions regardless the dihedral angle of the flippers (a) as well as the total spine pitch angle of the animal (b).

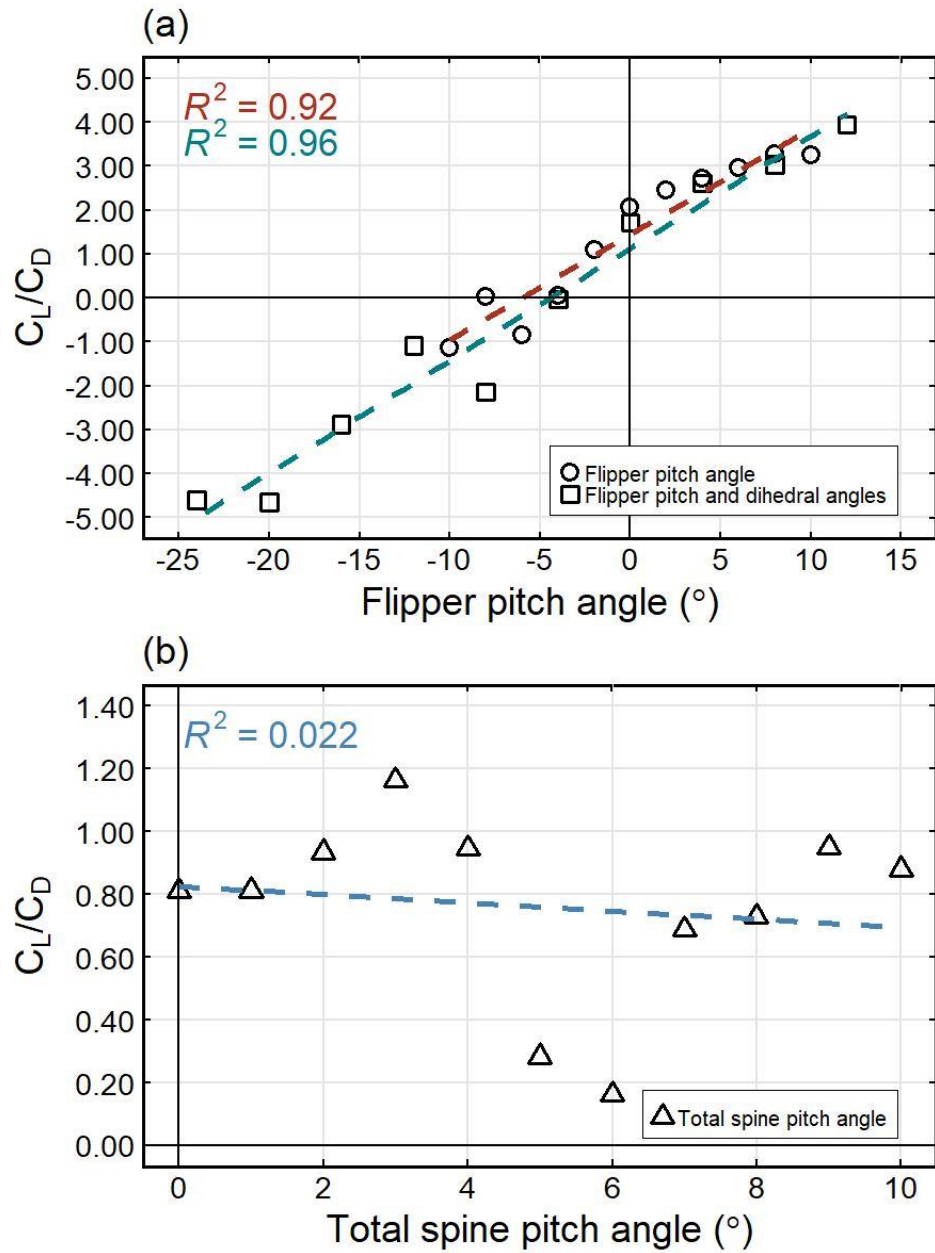


Figure 4.6 Hydrodynamic efficiency of the model associated with modified animal body pose. Hydrodynamic efficiency of the NARW model is dependent to its flipper pitch angle (a) but not the total spine pitch angle (b).

### **4.3.5 Hydrodynamic efficiency of the NARW model**

The hydrodynamic efficiency ( $C_L/C_D$ ) of the NARW model ranged from -4.60 to 3.94 under various body pose adjustments (Figure 4.6). I found that  $C_L/C_D$  is dependent to flipper pitch angle (Figure 4.6a) but not total spine pitch (Figure 4.6b). The NARW model with decreased flipper dihedral angle had an overall lower  $C_L/C_D$  from a flipper pitch angles of  $-4^\circ$  to  $8^\circ$  due to higher drag it produced in this angle range (Figure 4.4a).

### **4.3.6 Neutral trim pose of the NARW model**

Based on the best estimations, I adjusted the flipper pitch and total spine pitch angles that provide minimal drag and pitching moment on the NARW model (Table 4.2). Results from *scenario 3: flipper dihedral and pitch study* showed that drag was higher if the dihedral angle was decreased to  $20^\circ$  (relative to the horizontal plane). Hence, the initial flipper dihedral angle ( $45^\circ$ ) was used. In order to compare drag on NARW models with different body poses, I undertook CFD simulations at the same flow velocities as in chapter 2 (0.125-8.0 m/s). I found that lift generated by the NARW model with body pose adjustments is lower than the initial lift estimations across speeds tested (Figure 4.7a and Table 4.3). Differences in decreased lift production ranged from 50.66-86.89% at flow velocities  $\geq 1.5$  m/s. Whereas at flow velocities  $\leq 1$  m/s, the animal model was generating a small amount of negative lift ranged from 0.09 to 5.83 N. The dimensionless lift coefficient of different body poses as a function of flow speed is shown in Figure 4.7b. Hydrodynamic drag encountered by the animal with adjusted body pose is

9.95-12.34% lower than the original drag estimated in chapter 2 (Figure 4.8a and Table 3). Drag coefficient of different body poses as a function of flow speed is shown in Figure 4.8b. For the magnitude of pitching moment of the NARW model, adjusted body pose created 61.65-89.65% lower pitching moment on the animal across speeds tested (Figure 4.9a and Table 4.3). Here I considered the tendency of pitching so the direction of pitching moment was not included in the discussion. Pitching moment coefficient of different body poses as a function of flow speed was shown in Figure 9b. Differences of produced pitching moment between original and adjusted animal poses were found larger at lower flow speeds. Lastly, the hydrodynamic efficiency of original and adjusted body poses is shown in Figure 4.10. CFD results revealed that after the body pose adjustments, the NARW model was less hydrodynamically efficient due to reduced lift production, suggesting that there are tradeoffs between eliminating parasitic loads and keeping a body pose that provide higher hydrodynamic efficiency.

Table 4.2 NARW model position setup for Scenario 4: minimal drag pose simulations. A list of adjusted parameters for simulating the best estimation of animal body pose that creates minimal drag.

Flipper pitch angle*	Flipper dihedral angle‡	Spine pitch angle <sup>+</sup>	Total # of speed tested
-4.03°	0°	5°	11

\*the angle of attack facing incoming flow  
‡adjusted from the resting position (45°)  
<sup>+</sup>adjusted from the resting position (0° = horizontal tailstock)

Table 4.3 Changes of hydrodynamic forces and moment across speeds. Differences in lift, drag, and pitching moment generated by original and adjusted body poses are shown in percentage.

Speed (m/s)	Percentage changed (%)		
	Lift	Drag	Pitching moment*
0.125	-160.57	-9.95	-71.40
0.25	-151.07	-11.50	-80.68
0.5	-120.89	-10.08	-87.91
0.75	-111.38	-10.75	-82.75
1.0	-102.52	-11.34	-83.07
1.5	-86.89	-11.84	-89.65
2.0	-89.33	-11.95	-88.64
3.0	-69.70	-12.07	-80.22
4.0	-62.20	-12.34	-61.15
6.0	-51.39	-11.68	-77.73
8.0	-50.66	-11.50	-23.64

\*since pitching moment drives the model to rotate about the x-axis in either directions, only the magnitude (i.e., absolute values) of pitching moment was considered

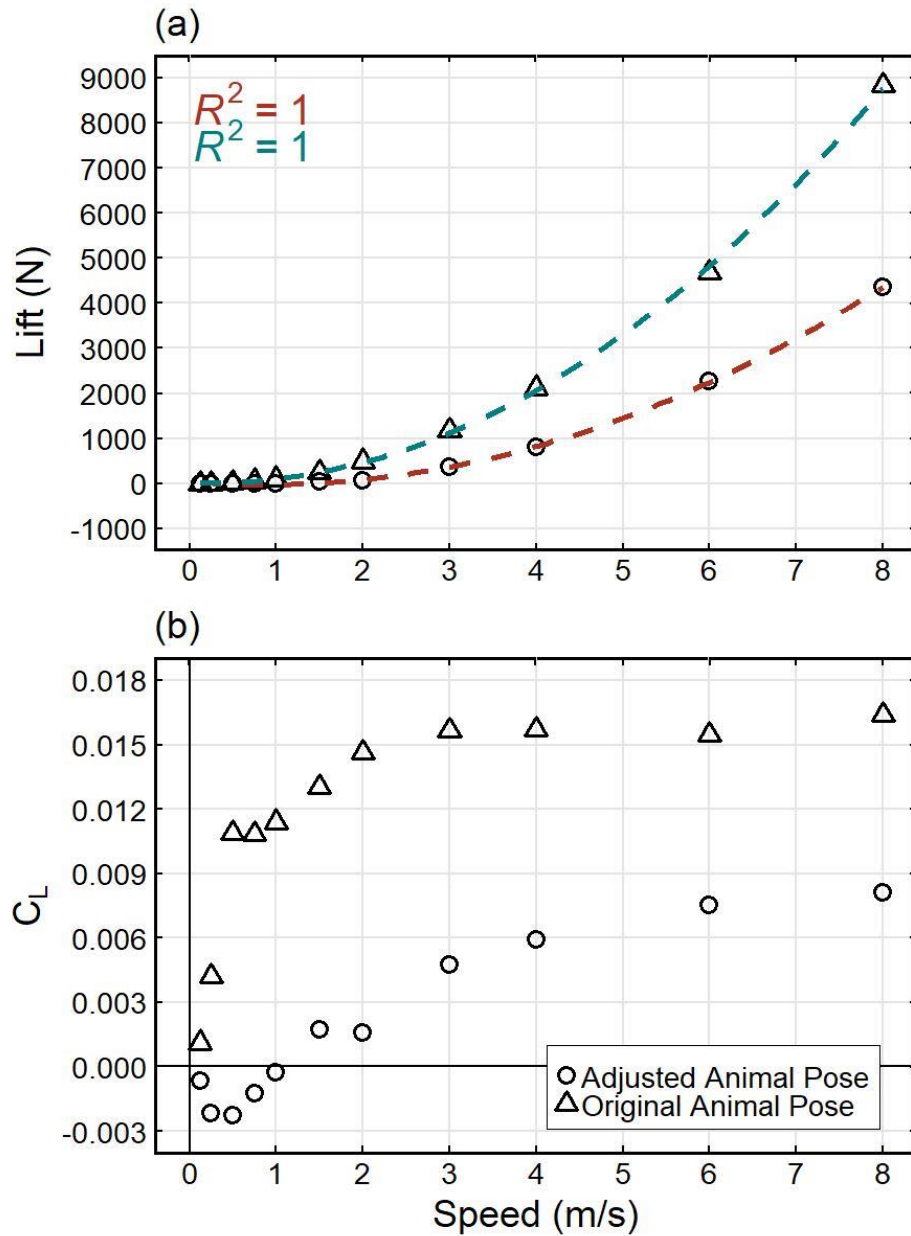


Figure 4.7 Comparison between lift from previous work and current study. Initial lift estimations were higher than lift measured with animal pose adjustments (a). At flow speeds  $\geq 1.5$  m/s, the amount of decreased lift ranged from 50.66-89.33%. Whereas at flow speeds  $\leq 1$  m/s, the model was creating negative lift. Lift differences across speeds tested are shown in Table 4.3.

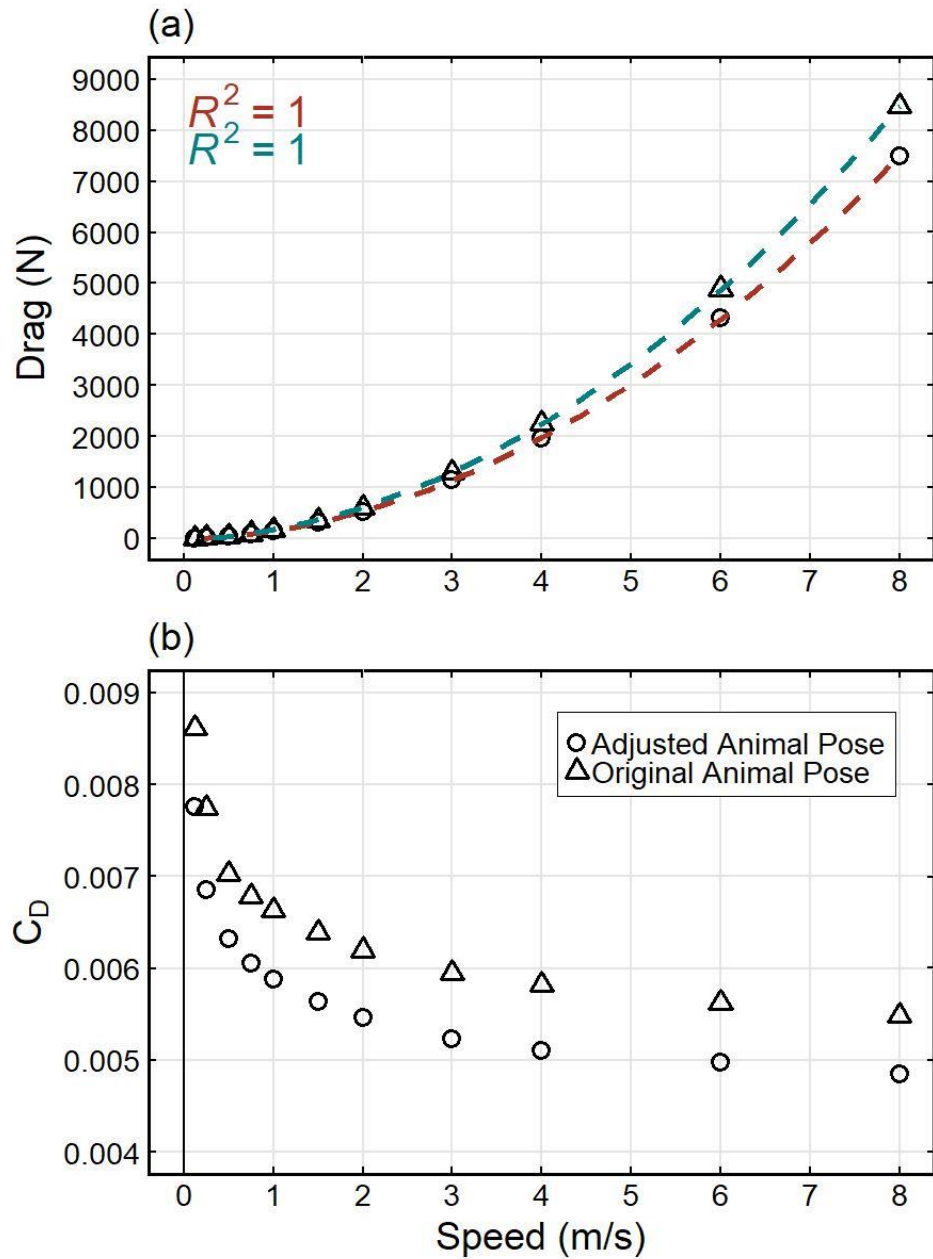


Figure 4.8 Comparison between drag from previous work and current study. Initial drag estimations were 9.95-12.34 % higher than drag measured with animal pose adjustments (a). Drag differences across speeds tested are shown in Table 4.3.

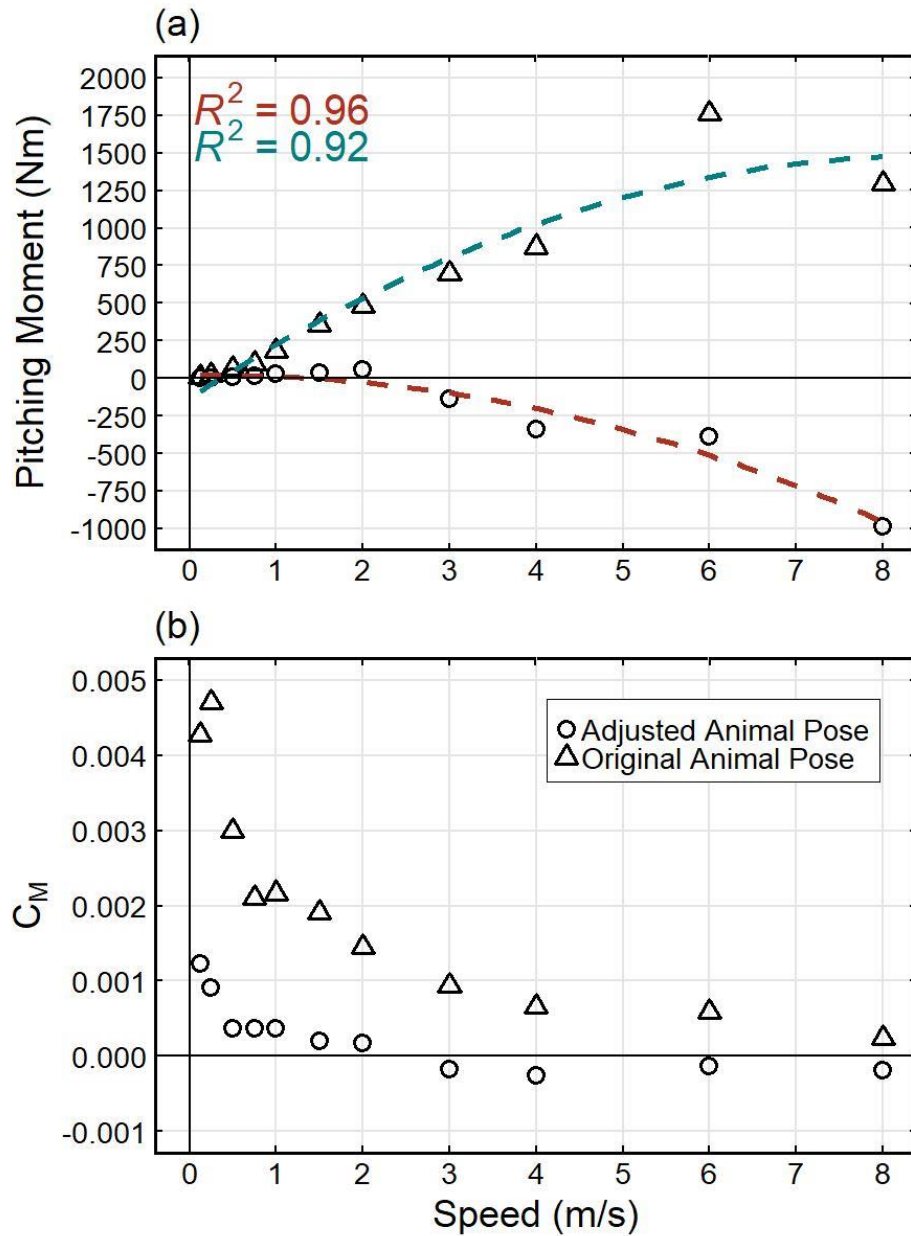


Figure 4.9 Comparison between pitching moment from previous work and current study. The magnitude of pitching moment (i.e., the absolute values of pitching moment were used here) created by adjusted animal pose ranged from 61.15-89.65% in either direction (a). Differences in pitching moment across speeds tested are shown in Table 4.3.

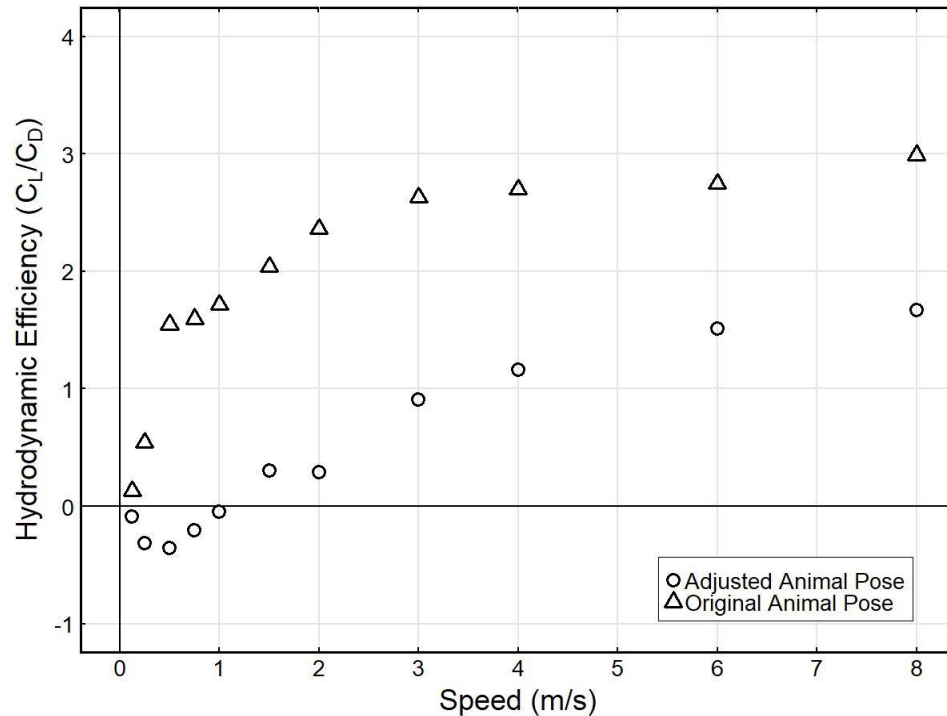


Figure 4.10 Differences in hydrodynamic efficiency between pre- and post-adjusted animal body position. Hydrodynamic efficiency of the NARW models decreased when simulated in its trim pose, which primary due to reduced lift production associated with the flipper pitch angle of the model (Figure 4.7).

## 4.4 Discussion

### 4.4.1 Lift, drag and pitching moment on the NARW model

As the angle of attack of both flippers was increased or decreased from  $0^\circ$ , the projected area of the flippers, which is perpendicular to the direction of incoming flow, also changed. In addition, altering the angle of attack of the appendages suggests that flow may be disturbed and result in variation in hydrodynamic forces. Therefore, drag on the NARW model was expected to increase as the flipper pitch angle was modified in either direction. However, I

found that drag increases while flipper pitch angles increased from  $0^\circ$  (i.e., the leading edge of both flippers was adjusted upward) and decreases as flipper pitch angles gained in negative direction, from  $0^\circ$  to  $-4.03^\circ$ . At a flipper pitch angle of  $-4.03^\circ$ , drag was minimal. At angles smaller than  $-4.03^\circ$ , drag increased as flipper pitch angle increased in negative direction. Although this value agrees with results from a previous study that flippers of cetaceans create minimum drag at an angle of attack between  $-4^\circ$  and  $2^\circ$  while tested at a flow speed of 2 m/s (Weber et al. 2009, Weber et al. 2014), differences between this study and the present one should be highlighted: I utilized numerical method to measure hydrodynamic properties of the entire animal, whereas Weber et al. (2009, 2014) conducted flow tank experiments on downscaled whale flipper physical models. Accordingly, while it sounds reasonable that no stall occurred within the range of angle of attack tested for all scenarios in present study, this could also be because the hydrodynamic effect of flippers was nullified by the entire animal body, which remained horizontal at an angle of attack of  $0^\circ$ . It is possible that hydrodynamic stall encountered by whale flippers was not detectable in the results because the overall lift on the animal is much higher.

#### **4.4.2 Hydrodynamic efficiency of different body poses**

The simulation results suggest that increasing the flipper pitch angle enhances the hydrodynamic efficiency of the NARW model, and the highest efficiency was measured at the maximum flipper pitch angle tested at  $15^\circ$ . Even though I did not cover a wider range of pitch angle, this finding is still consistent

with the results from flow tank experiments conducted by Weber *et al.* (2014), who found that the maximum hydrodynamic efficiency of cetacean flippers appears at approximately  $10^\circ$  in either positive or negative directions. Because there were little differences in lift production regardless of which flipper dihedral angles was used (Figure 3), lower efficiency associated with NARW model with decreased flipper dihedral angle resulted from an overall higher hydrodynamic drag on the animal. Modifying the total spine pitch angle slightly alters lift and drag production as well as the hydrodynamic efficiency of the model. However, no clear relationships between spine position and outcome forces was observed, which may be because the majority of the animal body and its fluke platform remained horizontal (i.e., the angle of attack of these body parts was  $0^\circ$ ) so the influences of re-positioned spine segments were not substantial.

#### **4.4.3 Neutral trim pose of the NARW model**

Results from CFD simulation suggest that cetaceans are able to balance pitching moment by adjusting their appendages accordingly. For example, decreasing the flipper pitch angle of the NARW model from  $2^\circ$  to  $-4.03^\circ$  (relative to the free-stream flow) must be accompanied by a  $5^\circ$  increase in the total spine pitch angle (i.e., pitching the spine downward) while maintaining fluke angle. By doing so, the animal can balance extra pitching moment generated by flippers positioned at different angle of attack (Table 4.4) and minimize additional drag (Fish and Shannahan 2000, Webb 2004, Payne et al. 2016). Being able to adjust body pose is likewise essential to stabilize recoil, overcome external perturbations,

and therefore reduce extra energy output while the animal is actively swimming (Webb 1988, 2002, Lauder 2011, Webb and Weihs 2015). Although flipper pitch angle and total spine pitch angle required to provide minimal pitching moment are similar for scenario 2 and 3 (Table 4), outcomes from scenario 3 were not considered because the overall drag on the NARW model was higher after the flipper dihedral angle of the animal was adjusted.

For the specific model used in this work, drag on the animal in trim was lowered by approximately 11% across the speeds tested. This drag reduction was relative to chapter 2 of this work on the same animal model but without body pose adjustments. Furthermore, measuring hydrodynamic forces and moments on animals in their trim pose eliminates artificial perturbances such as digital tags or data transmitters attached on the animals (Watson and Granger 1998, Shorter et al. 2014). Although there are an increasing number of publications addressing the hydrodynamic impacts of bio-logging tags on aquatic vertebrates (Jones et al. 2013, McIntyre 2015), most studies did not utilize an animal model in trim pose while measuring drag numerically (Shorter et al. 2014). Given that animals may balance parasitic loads by modifying their swimming behavior and thereby minimize drag due to tag attachment (van der Hoop et al. 2014a, van der Hoop et al. 2018, Zhang et al. 2019), neutral trim pose of the animal should be considered if one wants to calculate hydrodynamic drag with computer solutions. However, tradeoffs of minimizing drag appeared as I reduced the angle of attack of the

flippers (Figure 4.10); this is especially important if the research subject is negatively buoyant like sharks (Fish and Shannahan 2000).

Table 4.4 Body pose adjustments associated with minimal pitching moment. Direction of pitching moment is shown in parentheses.

Parameter	Scenario 1	Scenario 2	Scenario 3
Flipper pitch angle	2° (-)	-4.03° (+)	-4° (+)
Spine pitch angle	0° (+)	5° (-)	5° (-)
Flipper dihedral angle	45°	45°	25°

## **4.5 Conclusion**

This is the first study that uses a numerical approach to investigate ways to minimize drag on cetaceans. Although a static condition was considered in present work given the complexity of animal locomotion in nature, I found that minimum drag, which corresponds to the elimination of the parasitic loads, can be obtained by adjusting the pose of the animal; minimum drag occurs at the neutral trim pose. In the present study, drag on animals in trim pose was decreased by approximately 10% comparing to its original body pose where its flippers and spine are positioned at an angle of 0° relative to the free-stream flow. This finding underscores the need to find the model's neutral trim pose for baseline drag simulations. Therefore, I suggest that, in order to avoid over-estimating hydrodynamic drag due to unbalanced loads on the model, a preliminary study to identify parasitic loads is necessary. For research that estimate the hydrodynamic effects of animal-borne

devices, this approach is crucial. Those devices not only create drag resulting from increased frontal area and surface area, and less streamlining of the animal, etc., but also provide extra pitching moment and thereby additional drag.

## Chapter 5 Conclusion

It has been over half a century that scientists tried to study the hydrodynamics of aquatic vertebrates qualitatively (e.g., categorizing swimming gaits) or quantitatively (e.g., using physics theory to identify the dynamics of animal locomotion). Numerous approaches, including analyzing video recordings of underwater movements of captive animals, visualizing flow field with pioneered technology (e.g., digital particle image velocimetry, DPIV), and capturing the kinematics of aquatic vertebrates by animal-borne tags or drones, etc. have been widely used in this field of study. However, unlike fish, pinnipeds, and small odontocetes that can be investigated in a controlled environment (e.g., a flow tank or an oceanarium), large whales are less accessible due to their remote habitats and large size. Accordingly, data for large whales are relatively deficient.

In the present work, I explored and examined the capability of computational fluid dynamics modeling with a focus on the hydrodynamic characteristics of the North Atlantic right whale. The major findings of this dissertation include 1) CFD modeling is a practical approach to study the hydrodynamic performance of cetaceans, 2) change in body fitness will slightly affect the cost of locomotion of the right whale, and 3) it is necessary to find the neutral trim pose of any given animal model before measuring the parasitic forces (e.g., lift and drag) and loads (e.g., pitch, roll, and yaw moments) on the animal.

The first component of my work was to measure hydrodynamic drag on a gliding three-dimensional right whale model via CFD simulations (chapter 2). It

was found that drag on right whale is higher than previous estimations for this species and other large whales. Although various methods were used in literature and each of them had their strengths and weaknesses, data presented in current work should be considered as the baseline drag estimations for right whales because the model remained static (i.e., not undulating) during all tests and the flow field in the computational domain is more stable than the dynamic oceans (i.e., real condition). Therefore, once the animal starts to perform complex behavior such as undulating, streamlines around the animal will be “stirred”, become unstable, and ultimately cause higher drag on the animal. Given the capability of CFD models to provide detailed force distributions on a whale model as shown in chapter 2, two additional right whale models were built to represent an emaciated and a pregnant animal. A comparative study (chapter 3) was undertaken and CFD results showed that the emaciated animal encountered the highest dimensionless drag, whereas the pregnant individual experienced the minimal dimensionless drag among all three models. Possible explanations include that the post-nuchal concavity on the emaciated animal create extra surface area that facing incoming flow and increase pressure drag, and that the body shape of the pregnant animal allowed it to maintain favorable pressure gradient which delays the flow separation. In addition, differences in drag estimations between literature and the drag estimated in chapter 2 prompted a follow-up study (chapter 4) that investigated how the accuracy of drag estimated by CFD model can be improved. It was found that drag on the right whale model

can be decreased by approximately 10% across right whale speed range by adjusting the body pose of the animal. By doing so, the parasitic loads (i.e., unwanted hydrodynamic moments) and associated drag penalty will be eliminated.

Research conducted by this dissertation suggested that CFD modeling can serve as an alternative approach to elucidate the hydrodynamic characteristics of large whales. However, given the restrictions identified in present work (e.g., the animal model was static), future studies should address the kinematics of underwater movement (e.g., actively swimming or maneuvering, etc.) while measuring the cost of locomotion. In terms of the energetics of the North Atlantic right whale, I demonstrated that losing a portion of subcutaneous fat in post-nuchal region or becoming pregnant will not lead to an extensive increase in locomotor costs. This finding can be supported by the well-described feasting and fasting periods in capital breeders such as large whales. However, recent studies have shown that changes in body fitness of right whales are frequently accompanied by other incidents such as entanglement in fishing gear. Extra parasitic loads caused by attached gear as well as possible injuries due to the encounter should also be considered while evaluating the energy budget and population health of the North Atlantic right whales.

## **Appendix Chapter 2 Supplemental Information**

### **Introduction**

A grid convergence study and a domain convergence study were conducted to acquire essential parameters for computational fluid dynamics (CFD) simulations. Each simulation was tested separately at a flow speed of 2 m/s in half-domain on an 80-processor workstation with 256 GB of RAM. Drag results were converted to full-domain drag estimations by multiplying a factor of 2 in order to be comparable with the cross-section area of the 3-dimensional model and the computational domain size.

#### Grid Convergence Study

I performed a detailed grid convergence in order to obtain the reasonable mesh size and number of grid cells for the CFD simulations. I tested six different mesh sizes, from a total of 218,525 finite volume cells to 53,249,135 finite volume cells (Table S2.1).

The required solution time varied from approximately 4 minutes to 20 h for minimum and maximum mesh resolutions, respectively. It was found that drag converges to approximately 520 N with a total number of cells above  $10^7$  (Figure S2.1). Therefore, undertaking CFD simulations with approximately 12 million cells should suffice to provide robust drag estimations for my 3-dimensional right whale model with a reasonable CPU time of 4 h per simulation.

Table S2.1 Resolution tested in the grid convergence study.

Factor	Control plane resolution										Number of cells	Drag* (N)	Change regarding Factor 1.0 (%)
	X <sub>1</sub>	X <sub>2</sub>	Y <sub>1</sub>	Y <sub>2</sub>	Y <sub>3</sub>	Y <sub>4</sub>	Z <sub>1</sub>	Z <sub>2</sub>	Z <sub>3</sub>	Z <sub>4</sub>			
0.25	8	8	8	6	6	8	8	16	12	6	218,525	1057.29	100.71
0.50	16	16	16	12	12	16	16	32	24	12	1,666,739	695.09	31.95
0.75	24	24	24	18	18	24	24	48	36	18	5,426,525	569.19	8.05
1.00	32	32	32	24	24	32	32	64	48	24	12,821,590	526.78	0.00
1.25	40	40	40	30	30	40	40	80	60	30	24,993,674	521.60	-0.98
1.50	48	48	48	36	36	48	48	120	90	45	53,249,135	490.71	-6.85

\*Full-model drag in negative Z direction

Table S2.2 Dimensions tested in the domain convergence study.

Factor	Width (m)	Height (m)	Length (m)	Blockage Rate# (%)	Drag* (N)	Change regarding Factor 1.0 (%)
0.750	13.31	12.37	21.56	2.51	621.10	8.45
0.875	15.52	14.43	25.15	1.84	597.38	4.31
1.000	17.74	16.50	28.74	1.41	572.68	0.00
1.250	22.18	20.62	35.93	0.90	563.05	-1.68
1.500	26.61	24.74	43.11	0.63	579.36	1.17
2.000	35.48	32.99	57.49	0.35	579.92	1.26

#The projected area of the animal model is 4.13 m<sup>2</sup>  
\*Full-model drag in negative Z direction

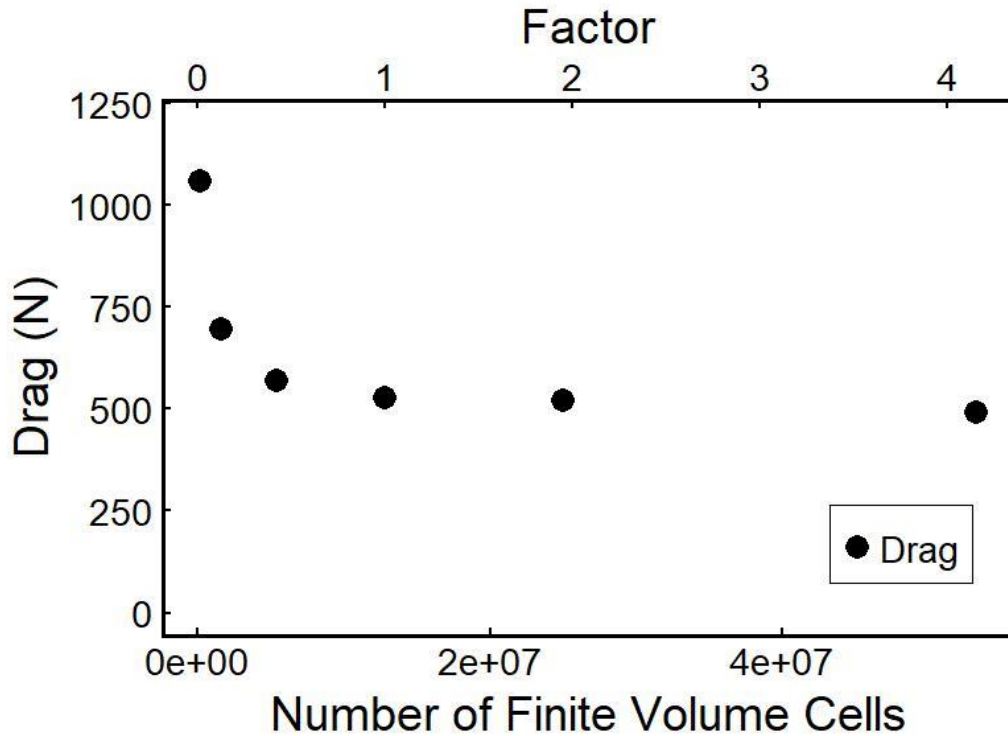


Figure S2.1 Drag and drag change as a function of number of cells tested. Full-model drag converges to approximately 520 N with a total number of cells above  $10^7$ .

Domain convergence study

In addition to defining the required mesh size, a domain convergence study was conducted to obtain the practical computational domain size to ensure that there are no wall effects and that the trailing vortices can be fully developed in downstream of the animal model. A total of six domain sizes with their dimensions ranged from approximately 13 m (wide) x 12 m (high) x 21.5 m (long) to 35 m (wide) x 33 m (high) x 57.5 m (long) were tested (Table S2.2). Center of gravity of the 3-dimensional model was placed at the middle of the cross-section plane and

at approximately 40% in the longitudinal (flow-wise) direction of the domain. I found that drag converges to approximately 580 N with a blockage ratio below 2% (Figure S2.2 and Figure S2.3). Therefore, a computational domain with 14 m (wide) x 14 m (high) x 27 m (long) dimensions was selected to provide drag estimations with a reasonable CPU time.

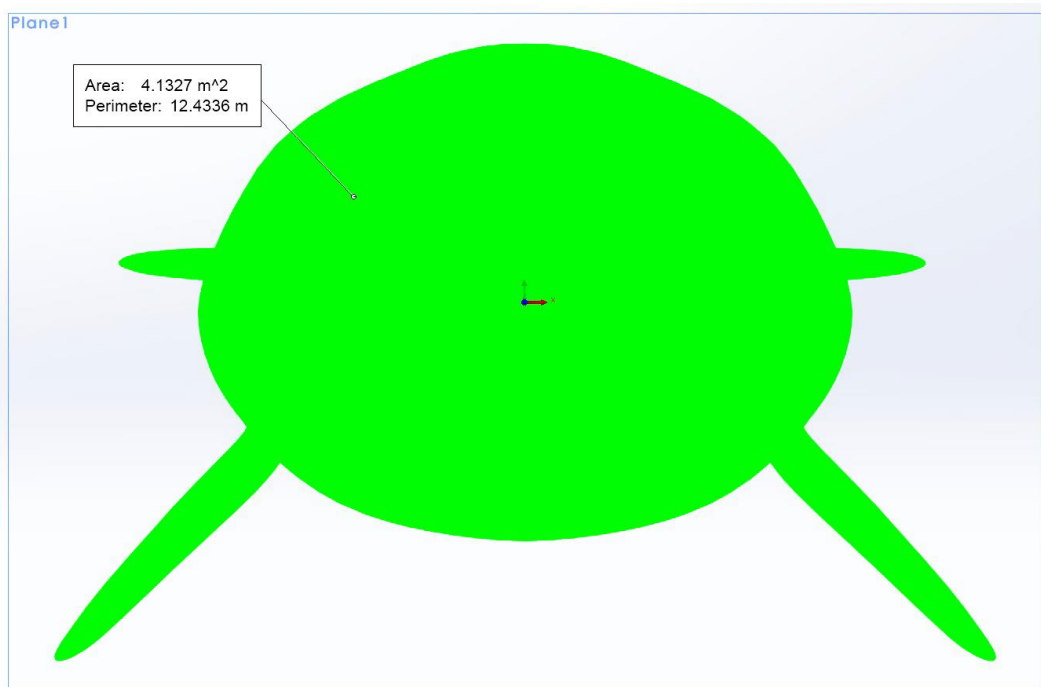


Figure S2.2 Blockage area of the three-dimensional model. The projected area of the 3-dimentional model is 4.13 m<sup>2</sup> and its perimeter is 12.43 m.

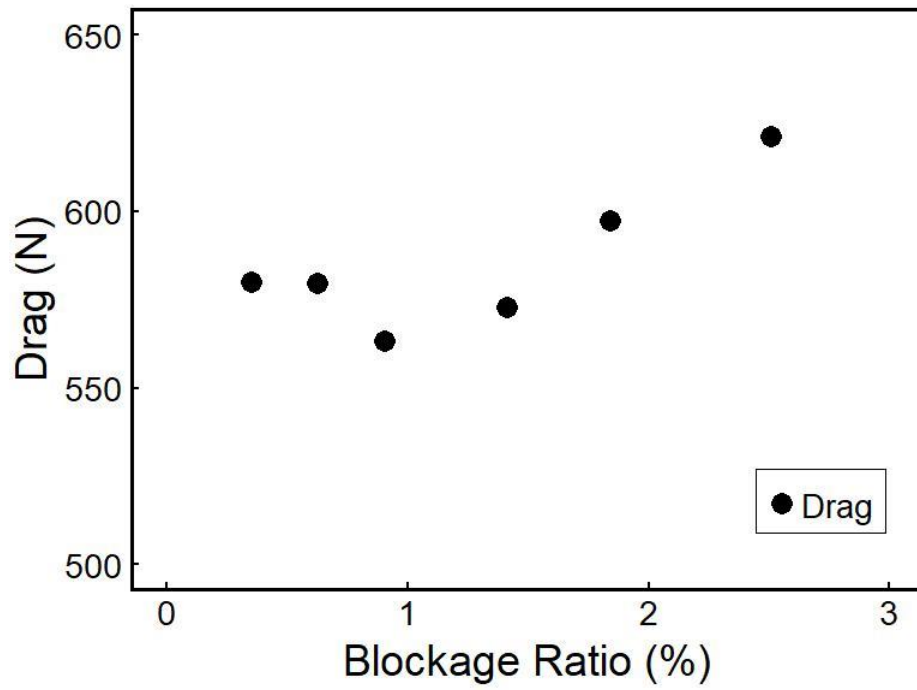


Figure S2.3 Drag as a function of blockage ratio. Full-model drag converges to approximately 580 N with a blockage ratio below 2%.

## References

- Anderson, J. D. 2010. Fundamentals of Aerodynamics. Fifth edition. McGraw-Hill, New York, NY.
- Baumgartner, M. F., and B. R. Mate. 2003. Summertime foraging ecology of North Atlantic right whales. *Marine Ecology Progress Series* **264**:123-135.
- Baumgartner, M. F., C. A. Mayo, and R. D. Kenney. 2007. Enormous carnivores, microscopic food, and a restaurant that's hard to find. Pages 138-171 in S. D. Kraus and R. M. Rolland, editors. *The Urban Whale: North Atlantic Right Whales at the Crossroads*. Harvard University Press, Cambridge, MA.
- Baumgartner, M. F., F. W. Wenzel, N. S. J. Lysiak, and M. R. Patrician. 2017. North Atlantic right whale foraging ecology and its role in human-caused mortality. *Marine Ecology Progress Series* **581**:165-181.
- Bose, N., and J. Lien. 1989. Propulsion of a fin whale (*Balaenoptera physalus*): why the fin whale is a fast swimmer. *Proceedings of the Royal Society Series B-Biological Sciences* **237**:175-200.
- Bradford, A. L., D. W. Weller, A. E. Punt, Y. V. Ivashchenko, A. M. Burdin, G. R. VanBlaricom, and J. Brownell, R. 2012. Leaner leviathans: body condition variation in a critically endangered whale population. *Journal of Mammalogy* **93**:251-266.
- Cassoff, R. M., K. M. Moore, W. A. McLellan, S. G. Barco, D. S. Rotstein, and M. J. Moore. 2011. Lethal entanglement in baleen whales. *Diseases of Aquatic Organisms* **96**:175-185.
- Caswell, H., M. Fujiwara, and S. Brault. 1999. Declining survival probability threatens the North Atlantic right whale. *Proceedings of the National Academy of Sciences of the United States of America* **96**:3308-3313.
- Christiansen, F., S. M. Dawson, J. W. Durban, H. Fearnbach, C. A. Miller, L. Bejder, M. Uhart, M. Sironi, P. Corkeron, W. Rayment, E. Leunissen, E. Haria, R. Ward, H. A. Warick, I. Kerr, M. S. Lynn, H. M. Pettis, and M. J. Moore. 2020. Population comparison of right whale body condition reveals poor state of the North Atlantic right whale. *Marine Ecology Progress Series* **640**:1-16.
- Clapham, P., S. Young, and J. Brownell, R. 1999. Baleen whales: conservation issues and the status of the most endangered populations. *Mammal Review* **29**:37 - 62.

- Corkeron, P., P. Hamilton, J. Bannister, P. Best, C. Charlton, K. R. Groch, K. Findlay, V. Rowntree, E. Vermeulen, and R. M. Pace. 2018. The recovery of North Atlantic right whales, *Eubalaena glacialis*, has been constrained by human-caused mortality. *Royal Society Open Science* **5**.
- Cutts, C., and J. Speakman. 1994. Energy savings in formation flight of pink-footed geese. *Journal of Experimental Biology* **189**:251-261.
- Daoust, P.-Y., E. L. Couture, T. Wimmer, and L. Bourque. 2017. Incident report: North Atlantic right whale mortality event in the Gulf of St. Lawrence, 2017. Collaborative Report Produced by: Canadian Wildlife Health Cooperative, Marine Animal Response Society, and Fisheries and Oceans Canada:256pp.
- Davies, K. T. A., M. W. Brown, P. K. Hamilton, A. R. Knowlton, C. T. Taggart, and A. S. M. Vanderlaan. 2019. Variation in North Atlantic right whale *Eubalaena glacialis* occurrence in the Bay of Fundy, Canada, over three decades. *Endangered Species Research* **39**:159-171.
- Davis, G. E., M. F. Baumgartner, J. M. Bonnell, J. Bell, C. Berchok, J. B. Thornton, S. Brault, G. Buchanan, R. A. Charif, D. Cholewiak, C. W. Clark, P. Corkeron, J. Delarue, K. Dudzinski, L. Hatch, J. Hildebrand, L. Hodge, H. Klinck, S. Kraus, B. Martin, D. K. Mellinger, H. Moors-Murphy, S. Nieu Kirk, D. P. Nowacek, S. Parks, A. J. Read, A. N. Rice, D. Risch, A. Sirovic, M. Soldevilla, K. Stafford, J. E. Stanistreet, E. Summers, S. Todd, A. Warde, and S. M. Van Parijs. 2017. Long-term passive acoustic recordings track the changing distribution of North Atlantic right whales (*Eubalaena glacialis*) from 2004 to 2014. *Scientific Reports* **7**.
- Drucker, E. G., and G. V. Lauder. 2000. A hydrodynamic analysis of fish swimming speed: wake structure and locomotor force in slow and fast labriform swimmers. *Journal of Experimental Biology* **203**:2379-2393.
- Drucker, E. G., and G. V. Lauder. 2002. Experimental hydrodynamics of fish locomotion: functional insights from wake visualization. *Integrative and Comparative Biology* **42**:243-257.
- Feldkamp, S. D. 1987. Swimming in the California sea lion: morphometrics, drag and energetics. *Journal of Experimental Biology* **131**:117-135.
- Fish, F. E. 1993a. Influence of hydrodynamic: design and propulsive mode on mammalian swimming energetics. *Australian Journal of Zoology* **42**:79-101.

- Fish, F. E. 1993b. Power output and propulsive efficiency of swimming bottlenose dolphins (*Tursiops truncatus*). *Journal of Experimental Biology* **185**:179-193.
- Fish, F. E. 1996. Transitions from drag-based to lift-based propulsion in mammalian swimming. *American Zoologist* **36**:628-641.
- Fish, F. E. 1998. Comparative kinematics and hydrodynamics of odontocete cetaceans: morphological and ecological correlates with swimming performance. *Journal of Experimental Biology* **201**:2867-2877.
- Fish, F. E. 2000. Biomechanics and energetics in aquatic and semiaquatic mammals: platypus to whale. *Physiological and Biochemical Zoology* **73**:683-698.
- Fish, F. E. 2002. Balancing requirements for stability and maneuverability in cetaceans. *Integrative and Comparative Biology* **42**:85-93.
- Fish, F. E., K. T. Goetz, D. J. Rugh, and L. Vate Brattström. 2012. Hydrodynamic patterns associated with echelon formation swimming by feeding bowhead whales (*Balaena mysticetus*). *Marine Mammal Science* **29**:E498–E507.
- Fish, F. E., L. E. Howle, and M. M. Murray. 2008. Hydrodynamic flow control in marine mammals. *Integrative and Comparative Biology* **48**:788-800.
- Fish, F. E., and C. A. Hui. 1991. Dolphin swimming – a review. *Mammal Review* **21**:181-195.
- Fish, F. E., S. Innes, and K. Ronald. 1988. Kinematics and estimated thrust production of swimming harp and ringed seals. *Journal of Experimental Biology* **137**:157-173.
- Fish, F. E., and G. V. Lauder. 2006. Passive and active flow control by swimming fishes and mammals. *Annual Review of Fluid Mechanics* **38**:193-224.
- Fish, F. E., and G. V. Lauder. 2017. Control surfaces of aquatic vertebrates: active and passive design and function. *Journal of Experimental Biology* **220**:4351-4363.
- Fish, F. E., P. Legac, T. M. Williams, and T. Wei. 2014. Measurement of hydrodynamic force generation by swimming dolphins using bubble DPIV. *Journal of Experimental Biology* **217**:252-260.
- Fish, F. E., and L. D. Shannahan. 2000. The role of the pectoral fins in body trim of sharks. *Journal of Fish Biology* **56**:1062-1073.

- Floryana, D., T. Van Burena, and A. J. Smitsa. 2018. Efficient cruising for swimming and flying animals is dictated by fluid drag. *Proceedings of the National Academy of Sciences of the United States of America* **115**:8116-8118.
- Fortune, S. M. E., A. W. Trites, C. Mayo, D. A. S. Rosen, and P. Hamilton. 2013. Energetic requirements of North Atlantic right whales and the implications for species recovery. *Marine Ecology Progress Series* **478**:253–272.
- Gazzola, M., M. Argentina, and L. Mahadevan. 2014. Scaling macroscopic aquatic locomotion. *Nature Physics* **10**:758–761.
- Gingerich, P. D., B. H. Smith, and E. L. Simons. 1990. Hind limbs of Eocene *Basilosaurus*: evidence of feet in whales. *Science* **249**:154-157.
- Goldbogen, J. A., J. Calambokidis, D. A. Croll, M. F. McKenna, E. Oleson, J. Potvin, N. D. Pyenson, G. Schorr, R. E. Shadwick, and B. R. Tershy. 2012. Scaling of lunge-feeding performance in rorqual whales: mass-specific energy expenditure increases with body size and progressively limits diving capacity. *Functional Ecology* **26**:216-226.
- Goldbogen, J. A., J. Calambokidis, R. E. Shadwick, E. M. Oleson, M. A. McDonald, and J. A. Hildebrand. 2006. Kinematics of foraging dives and lunge-feeding in fin whales. *Journal of Experimental Biology* **209**:1231-1244.
- Goldbogen, J. A., N. D. Pyenson, and R. E. Shadwick. 2007. Big gulps require high drag for fin whale lunge feeding. *Marine Ecology Progress Series* **349**:289-301.
- Hain, J. H., J. D. Hampp, S. A. McKenney, J. A. Albert, and R. D. Kenney. 2013. Swim speed, behavior, and movement of North Atlantic right whales (*Eubalaena glacialis*) in coastal waters of northeastern Florida, USA. *PLoS One* **8**:e54340.
- Hall, K. C., and S. R. Hall. 1996. Minimum induced power requirements for flapping flight. *Journal of Fluid Mechanics* **323**:285-315.
- Hall, K. C., and L. E. Howle. 2005. The mechanics of flapping flight. Final report on research funded by NASA Langley Research Center (NASA Grant NAG 1-01062).
- Hoerner, S. F. 1965. Fluid-dynamic drag: practical information on aerodynamic drag and hydrodynamic resistance. Second edition. Hoerner Fluid Dynamics, Midland Park, N.J.

- Howle, L. E., S. Kraus, T. Werner, and D. P. Nowacek. 2018. Simulation of the entanglement of a North Atlantic right whale (*Eubalaena glacialis*) with fixed fishing gear. *Marine Mammal Science* **35**:760-778.
- Jefferson, T. A., M. A. Webber, and R. L. Pitman. 2008. *Marine mammals of the world: a comprehensive guide to their identification*. Elsevier.
- Johnson, A., G. Salvador, J. Kenney, J. Robbins, S. Landry, and P. Clapham. 2005. Fishing gear involved in entanglements of right and humpback whales. *Marine Mammal Science* **21**:635-645.
- Jones, T. T., K. S. Van Houtan, B. L. Bostrom, P. Ostafichuk, J. Mikkelsen, E. Tezcan, M. Carey, B. Imlach, and J. A. Seminoff. 2013. Calculating the ecological impacts of animal-borne instruments on aquatic organisms. *Methods in Ecology and Evolution* **4**:1178-1186.
- Kenney, R. D., M. A. M. Hyman, R. E. Owen, G. P. Scott, and H. E. Winn. 1986. Estimation of prey densities required by western North Atlantic right whales. *Marine Mammal Science* **2**:1-13.
- Knowlton, A. R., P. K. Hamilton, M. K. Marx, H. M. Pettis, and S. D. Kraus. 2012. Monitoring North Atlantic right whale *Eubalaena glacialis* entanglement rates: a 30 yr retrospective. *Marine Ecology Progress Series* **466**:293-302.
- Knowlton, A. R., and S. D. Kraus. 2001. Mortality and serious injury of northern right whales (*Eubalaena glacialis*) in the western North Atlantic Ocean. *Journal of Cetacean Research and Management* **2**:193-208.
- Knowlton, A. R., J. Robbins, S. Landry, H. A. McKenna, S. D. Kraus, and T. B. Werner. 2016. Effects of fishing rope strength on the severity of large whale entanglements. *Conservation Biology* **30**:318-328.
- Koopman, H. 1998. Topographical distribution of the blubber of harbor porpoises (*Phocoena phocoena*). *Journal of Mammalogy* **79**:260-270.
- Koopman, H., D. A. Pabst, W. McLellan, R. M. Dillaman, and A. J. Read. 2002. Changes in blubber distribution and morphology associated with starvation in the harbor porpoise (*Phocoena phocoena*): evidence for regional differences in blubber structure and function. *Physiological and Biochemical Zoology* **75**:498-512.
- Kraus, S., P. Hamilton, R. D. Kenney, A. Knowlton, and C. Slay. 2001. Reproductive parameters of the North Atlantic right whale. *Journal of Cetacean Research and Management (Special Issue)* **2**:231-236.

- Kraus, S. D., M. W. Brown, H. Caswell, C. W. Clark, M. Fujiwara, P. K. Hamilton, R. D. Kenney, A. R. Knowlton, S. Landry, C. A. Mayo, W. A. McLellan, M. J. Moore, D. P. Nowacek, D. A. Pabst, A. J. Read, and R. M. Rolland. 2005. Ecology. North Atlantic right whales in crisis. *Science* **309**:561-562.
- Kraus, S. D., R. D. Kenney, C. A. Mayo, W. A. McLellan, M. J. Moore, and D. P. Nowacek. 2016. Recent scientific publications cast doubt on North Atlantic right whale future. *Frontiers in Marine Science* **3**:137.
- Kraus, S. D., J. H. Prescott, A. R. Knowlton, and G. S. Stone. 1986. Migration and calving of right whales (*Eubalaena glacialis*) in the Western North Atlantic. Reports of the International Whaling Commission Special Issue **10**:139-144.
- Kraus, S. D., and R. M. Rolland. 2007. Right whales in the urban ocean. Pages 1-38 in S. D. Kraus and R. M. Rolland, editors. *The Urban Whale: North Atlantic Right Whales at the Crossroads*. Harvard University Press, Cambridge, MA.
- Laist, D. W., A. R. Knowlton, and D. Pendleton. 2014. Effectiveness of mandatory vessel speed limits for protecting North Atlantic right whales. *Endangered Species Research* **23**:133-147.
- Lambertsen, R. H., K. J. Rasmussen, W. C. Lancaster, and R. J. Hintz. 2005. Functional morphology of the mouth of the bowhead whale and its implications for conservation. *Journal of Mammalogy* **86**:342-352.
- Lang, T. G., and D. A. Daybell. 1963. Porpoise performance tests in a seawater tank. NAVWEPS Report 8060 (NOTS Technology Publication 3063).
- Lang, T. G., and K. Pryor. 1966. Hydrodynamic performance of porpoises (*Stenella attenuate*). *Science* **152**:531-533.
- Lauder, G. V. 2011. Swimming hydrodynamics: ten questions and the technical approaches needed to resolve them. *Experiments in Fluids* **51**:23-35.
- Lauder, G. V., and E. G. Drucker. 2002. Forces, fishes, and fluids: hydrodynamic mechanisms of aquatic locomotion. *News in Physiological Sciences* **17**:235-240.
- Liao, J. C. 2007. A review of fish swimming mechanics and behaviour in altered flows. *Philosophical Transactions of the Royal Society B* **362**:1973-1993.
- Lighthill, M. J. 1969. Hydromechanics of aquatic animal propulsion. *Annual Review of Fluid Mechanics* **1**:413-446.

- Lissaman, P. B., and C. A. Shollenberger. 1970. Formation flight of birds. *Science* **168**:1003-1005.
- Lockyer, C. 1984. Review of baleen whale (Mysticeti) reproduction and implications for management. Report - International Whaling Commission:27-50.
- Lockyer, C. 1986. Body fat condition in northeast Atlantic fin whales, *Balaenoptera physalus*, and its relationship with reproduction and food resource. *Canadian Journal of Fisheries and Aquatic Sciences* **43**:142-147.
- Mate, B. R., S. L. Niekirk, and S. D. Kraus. 1997. Satellite-monitored movements of the northern right whale. *Journal of Wildlife Management* **61**:1393-1405.
- Mayo, C. A., B. H. Letcher, and S. Scott. 2001. Zooplankton filtering efficiency of the baleen of a North Atlantic right whale, *Eubalaena glacialis*. *Journal of Cetacean Research and Management (Special Issue)* **2**:225-229.
- Mayo, C. A., and M. K. Marx. 1990. Surface foraging behavior of the North Atlantic right whale, *Eubalaena glacialis*, and associated zooplankton characteristics. *Canadian Journal of Zoology* **68**:2214-2220.
- McIntyre, T. 2015. Animal telemetry: tagging effects. *Science* **349**:596-597.
- Miller, C. A., P. B. Best, W. L. Perryman, M. F. Baumgartner, and M. J. Moore. 2012. Body shape changes associated with reproductive status, nutritive condition and growth in right whales *Eubalaena glacialis* and *E. australis*. *Marine Ecology Progress Series* **459**:135-156.
- Miller, C. A., D. Reeb, P. B. Best, A. R. Knowlton, M. W. Brown, and M. J. Moore. 2011. Blubber thickness in right whales *Eubalaena glacialis* and *Eubalaena australis* related with reproduction, life history status and prey abundance. *Marine Ecology Progress Series* **438**:267-283.
- Miller, P. J. O., M. P. Johnson, P. L. Tyack, and E. A. Terray. 2004. Swimming gaits, passive drag and buoyancy of diving sperm whales *Physeter macrocephalus*. *Journal of Experimental Biology* **207**:1953-1967.
- Moore, M., A. Knowlton, S. Kraus, W. McLellan, and R. Bode. 2005. Morphometry, gross morphology and available histopathology in North Atlantic right whale (*Eubalaena glacialis*) mortalities (1970-2002). *Journal of Cetacean Research and Management* **63**.
- Moore, M., M. Walsh, J. Bailey, D. Brunson, F. Gulland, S. Landry, D. Mattila, C. Mayo, C. Slay, J. Smith, and T. Rowles. 2010. Sedation at sea of entangled

- North Atlantic right whales (*Eubalaena glacialis*) to enhance disentanglement. PLoS One **5**:e9597.
- Moore, M. J. 2014. How we all kill whales. Ices Journal of Marine Science **71**:760-763.
- Moore, M. J., J. van der Hoop, S. G. Barco, A. M. Costidis, F. M. Gulland, P. D. Jepson, K. T. Moore, S. Raverty, and W. A. McLellan. 2013. Criteria and case definitions for serious injury and death of pinnipeds and cetaceans caused by anthropogenic trauma. Diseases of Aquatic Organisms **103**:229-264.
- Moore, M. J., and J. M. van der Hoop. 2012. The painful side of trap and fixed net fisheries: chronic entanglement of large whales. Journal of Marine Biology **2012**.
- Munson, B. R., D. F. Young, T. H. Okiishi, and W. W. Huebsch. 2010. Fundamentals of fluid mechanics. 6th edition. Wiley, Chichester, United Kingdom.
- NMFS. 2017. North Atlantic right whale (*Eubalaena glacialis*) 5-year review: summary and evaluation.
- Nousek-McGregor, A. E. 2010. The cost of locomotion in North Atlantic right whales (*Eubalaena glacialis*). Duke University, Beaufort, NC.
- Nousek-McGregor, A. E., C. A. Miller, M. J. Moore, and D. P. Nowacek. 2014. Effects of body condition on buoyancy in endangered North Atlantic right whales. Physiol Biochem Zool **87**:160-171.
- Nowacek, D. P., M. P. Johnson, P. L. Tyack, K. A. Shorter, W. A. McLellan, and D. A. Pabst. 2001. Buoyant balaenids: the ups and downs of buoyancy in right whales. Proceedings of the Royal Society B-Biological Sciences **268**:1811-1816.
- Pace, R. M., P. J. Corkeron, and S. D. Kraus. 2017. State-space mark-recapture estimates reveal a recent decline in abundance of North Atlantic right whales. Ecology and Evolution **7**:8730-8741.
- Payne, N. L., G. Iosilevskii, A. Barnett, C. Fischer, R. T. Graham, A. C. Gleiss, and Y. Y. Watanabe. 2016. Great hammerhead sharks swim on their side to reduce transport costs. Nature Communications **7**:12289.
- Perryman, W. L., and M. S. Lynn. 2002. Evaluation of nutritive condition and reproductive status of migrating gray whales (*Eschrichtius robustus*) based

- on analysis of photogrammetric data. *Journal of Cetacean Research and Management* **4**:155-164.
- Pettis, H. M., R. M. I. Pace, and P. K. Hamilton. 2020. North Atlantic Right Whale Consortium 2019 Annual Report Card.
- Pettis, H. M., R. M. I. Pace, R. S. Schick, and P. K. Hamilton. 2017a. North Atlantic Right Whale Consortium 2017 Annual Report Card.
- Pettis, H. M., R. M. Rolland, P. K. Hamilton, S. Brault, A. R. Knowlton, and S. D. Kraus. 2004. Visual health assessment of North Atlantic right whales (*Eubalaena glacialis*) using photographs. *Canadian Journal of Zoology-Revue Canadienne De Zoologie* **82**:8-19.
- Pettis, H. M., R. M. Rolland, P. K. Hamilton, A. R. Knowlton, E. A. Burgess, and S. D. Kraus. 2017b. Body condition changes arising from natural factors and fishing gear entanglements in North Atlantic right whales *Eubalaena glacialis*. *Endangered Species Research* **32**:237-249.
- Record, N. R., J. A. Runge, D. E. Pendleton, W. M. Balch, K. T. A. Davies, A. J. Pershing, C. L. Johnson, K. Stamieszkin, R. B. Ji, Z. X. Feng, S. D. Kraus, R. D. Kenney, C. A. Hudak, C. A. Mayo, C. Chen, J. E. Salisbury, and C. R. S. Thompson. 2019. Rapid climate-driven circulation changes threaten conservation of endangered North Atlantic right whales. *Oceanography* **32**:162-169.
- Reeves, R., and E. Mitchell. 1986a. American pelagic whaling for right whales in the North Atlantic. *Reports of the International Whaling Commission Special Issue* **10**:221-254.
- Reeves, R., and E. Mitchell. 1986b. The Long Island, New York, right whale fishery: 1650-1924. *Reports of the International Whaling Commission Special Issue* **10**:201-220.
- Reeves, R. R., T. D. Smith, and E. A. Josephson. 2007. Near-annihilation of a species: right whaling in the North Atlantic. Pages 39-74 in S. D. Kraus and R. M. Rolland, editors. *The Urban Whale: North Atlantic Right Whales at the Crossroads*. Harvard University Press, Cambridge, MA.
- Robbins, J., A. Knowlton, and S. Landry. 2015. Apparent survival of North Atlantic right whales after entanglement in fishing gear. *Biological Conservation* **191**:421-427.
- Rohr, J. J., and F. E. Fish. 2004. Strouhal numbers and optimization of swimming by odontocete cetaceans. *Journal of Experimental Biology* **207**:1633-1642.

- Rolland, R. M., W. A. McLellan, M. J. Moore, C. A. Harms, E. A. Burgess, and K. E. Hunt. 2017. Fecal glucocorticoids and anthropogenic injury and mortality in North Atlantic right whales *Eubalaena glacialis*. *Endangered Species Research* **34**:417-429.
- Sharp, S. M., W. A. McLellan, D. S. Rotstein, A. M. Costidis, S. G. Barco, K. Durham, T. D. Pitchford, K. A. Jackson, P. Y. Daoust, T. Wimmer, E. L. Couture, L. Bourque, T. Frasier, B. Frasier, D. Fauquier, T. K. Rowles, P. K. Hamilton, H. Pettis, and M. J. Moore. 2019. Gross and histopathologic diagnoses from North Atlantic right whale *Eubalaena glacialis* mortalities between 2003 and 2018. *Diseases of Aquatic Organisms* **135**:1-31.
- Shorter, K. A., M. M. Murray, M. Johnson, M. Moore, and L. E. Howle. 2014. Drag of suction cup tags on swimming animals: modeling and measurement. *Marine Mammal Science* **30**:726-746.
- Solvang, H. K., H. Yanagihara, N. Øien, and T. Haug. 2017. Temporal and geographical variation in body condition of common minke whales (*Balaenoptera acutorostrata acutorostrata*) in the Northeast Atlantic. *Polar Biology* **40**:667-683.
- Sumich, J. L. 1983. Swimming velocities, breathing patterns, and estimated costs of locomotion in migrating gray whales, *Eschrichtius robustus*. *Canadian Journal of Zoology* **61**:647-652.
- Taylor, G. K., R. L. Nudds, and A. L. R. Thomas. 2003. Flying and swimming animals cruise at a Strouhal number tuned for high power efficiency. *Nature* **425**:707-711.
- Triantafyllou, G. S., M. S. Triantafyllou, and M. A. Grosenbaugh. 1993. Optimal Thrust Development in Oscillating Foils with Application to Fish Propulsion. *Journal of Fluids and Structures* **7**:205-224.
- Triantafyllou, M. S. 2017. Tuna fin hydraulics inspire aquatic robotics. *Science* **357**:251-252.
- Triantafyllou, M. S., G. S. Triantafyllou, and D. K. P. Yue. 2000. Hydrodynamics of fishlike swimming. *Annual Review of Fluid Mechanics* **32**:33-53.
- Tucker, V. A. 1975. The energetic cost of moving about: walking and running are extremely inefficient forms of locomotion. Much greater efficiency is achieved by birds, fish—and bicyclists. *American Scientist* **63**:413-419.
- Uhen, M. D. 2010. The origin(s) of whales. *Annual Review of Earth and Planetary Sciences* **38**:189-219.

- van der Hoop, J., P. Corkeron, A. Henry, A. Knowlton, and M. Moore. 2017a. Predicting lethal entanglements as a consequence of drag from fishing gear. *Marine Pollution Bulletin* **115**:91-104.
- van der Hoop, J., P. Corkeron, and M. Moore. 2017b. Entanglement is a costly life-history stage in large whales. *Ecology and Evolution* **7**:92-106.
- van der Hoop, J., A. Fahlman, T. Hurst, J. Rocho-Levine, K. A. Shorter, V. Petrov, and M. Moore. 2014a. Bottlenose dolphins modify behavior to reduce metabolic effect of tag attachment. *Journal of Experimental Biology* **217**:4229-4236.
- van der Hoop, J., M. Moore, A. Fahlman, A. Bocconcelli, C. George, K. Jackson, C. Miller, D. Morin, T. Pitchford, T. Rowles, J. Smith, and B. Zoodsma. 2014b. Behavioral impacts of disentanglement of a right whale under sedation and the energetic cost of entanglement. *Marine Mammal Science* **30**:282-307.
- van der Hoop, J., A. E. Nousek-McGregor, D. P. Nowacek, S. Parks, P. Tyack, and P. T. Madsen. 2019. Foraging rates of ram-filtering North Atlantic right whales. *Functional Ecology* **33**:1290–1306.
- van der Hoop, J. M., P. Corkeron, J. Kenney, S. Landry, D. Morin, J. Smith, and M. J. Moore. 2016. Drag from fishing gear entangling North Atlantic right whales. *Marine Mammal Science* **32**:619-642.
- van der Hoop, J. M., A. Fahlman, K. A. Shorter, J. Gabaldon, J. Rocho-Levine, V. Petrov, and M. J. Moore. 2018. Swimming energy economy in bottlenose dolphins under variable drag loading. *Frontiers in Marine Science* **5**:465.
- van der Hoop, J. M., D. P. Nowacek, M. J. Moore, and M. S. Triantafyllou. 2017c. Swimming kinematics and efficiency of entangled North Atlantic right whales. *Endangered Species Research* **32**:1-17.
- Vogel, S. 1994. *Life in moving fluids: the physical biology of flow*. 2nd edition. Princeton University Press, Princeton, NJ.
- Vogel, S. 2008. Modes and scaling in aquatic locomotion. *Integrative and Comparative Biology* **48**:702-712.
- Waring, G. T., E. Josephson, K. Maze-Foley, and P. E. Rosel. 2016. US Atlantic and Gulf of Mexico. *Marine mammal stock assessments – 2015*.
- Watkins, W. A., and W. E. Schevill. 1976. Right whale feeding and baleen rattle. *Journal of Mammalogy* **57**:58-66.

- Watson, K. P., and R. A. Granger. 1998. Hydrodynamic effect of a satellite transmitter on a juvenile green turtle (*Chelonia mydas*). *Journal of Experimental Biology* **201**:2497-2505.
- Webb, P. W. 1975. Hydrodynamics and energetics of fish propulsion. Pages 1–159 *Bulletin of the Fisheries Research Board of Canada*. Information Canada, Ottawa, Canada.
- Webb, P. W. 1984. Form and function in fish swimming. *Scientific American* **251**:72-83.
- Webb, P. W. 1988. Simple physical principles and vertebrate aquatic locomotion. *American Zoologist* **28**:709-725.
- Webb, P. W. 2002. Control of posture, depth, and swimming trajectories of fishes. *Integrative and Comparative Biology* **42**:94-101.
- Webb, P. W. 2004. Maneuverability - general issues. *Ieee Journal of Oceanic Engineering* **29**:547-555.
- Webb, P. W., and D. Weihs. 2015. Stability versus maneuvering: challenges for stability during swimming by fishes. *Integrative and Comparative Biology* **55**:753-764.
- Weber, P. W., L. E. Howle, M. M. Murray, and F. E. Fish. 2009. Lift and drag performance of odontocete cetacean flippers. *Journal of Experimental Biology* **212**:2149-2158.
- Weber, P. W., L. E. Howle, M. M. Murray, and D. S. Miklosovic. 2011. Computational evaluation of the performance of lifting surfaces with leading-edge protuberances. *Journal of Aircraft* **48**:591-600.
- Weber, P. W., L. E. Howle, M. M. Murray, J. S. Reidenberg, and F. E. Fish. 2014. Hydrodynamic performance of the flippers of large-bodied cetaceans in relation to locomotor ecology. *Marine Mammal Science* **30**:413–432.
- Weihs, D. 2004. The hydrodynamics of dolphin drafting. *Journal of Biology* **3**:Article number: 8.
- Weihs, D., and E. Farhi. 2017. Passive forces aiding coordinated groupings of swimming animals. *Theoretical and Applied Mechanics Letters* **7**:276-279.
- Weimerskirch, H., J. Martin, Y. Clerquin, P. Alexandre, and S. Jiraskova. 2001. Energy saving in flight formation. *Nature* **413**:697-698.

- Werth, A. J. 2001. How do mysticetes remove prey trapped in baleen? *Bulletin of the Museum of Comparative Zoology* **156**:189-203.
- Werth, A. J. 2004. Models of hydrodynamic flow in the bowhead whale filter feeding apparatus. *Journal of Experimental Biology* **207**:3569-3580.
- Williams, R., and D. P. Noren. 2009. Swimming speed, respiration rate, and estimated cost of transport in adult killer whales. *Marine Mammal Science* **25**:327-350.
- Williams, T. M. 1999. The evolution of cost efficient swimming in marine mammals: limits to energetic optimization. *Philosophical Transactions of the Royal Society B-Biological Sciences* **354**:193-201.
- Williams, T. M., R. W. Davis, L. A. Fuiman, J. Francis, B. J. Le Boeuf, M. Horning, J. Calambokidis, and D. A. Croll. 2000. Sink or swim: strategies for cost-efficient diving by marine mammals. *Science* **288**:133-136.
- Williams, T. M., W. A. Friedl, M. L. Fong, R. M. Yamada, P. Sedivy, and J. E. Haun. 1992a. Travel at Low Energetic Cost by Swimming and Wave-Riding Bottlenosed Dolphins. *Nature* **355**:821-823.
- Williams, T. M., W. A. Friedl, M. L. Fong, R. M. Yamada, P. Sedivy, and J. E. Haun. 1992b. Travel at low energetic cost by swimming and wave-riding bottlenose dolphins. *Nature* **355**:821-823.
- Williams, T. M., L. A. Fuiman, M. Horning, and R. W. Davis. 2004. The cost of foraging by a marine predator, the Weddell seal *Leptonychotes weddellii*: pricing by the stroke. *Journal of Experimental Biology* **207**:973-982.
- Williams, T. M., and J. L. Maresh. 2015. Exercise energetics. Pages 47-68 in M. A. Castellini and J.-A. Mellish, editors. *Marine Mammal Physiology: Requisites for Ocean Living*. CRC Press, Boca Raton, FL.
- Woodward, B. L., J. P. Winn, and F. E. Fish. 2006a. Morphological specializations of baleen whales associated with hydrodynamic performance and ecological niche. *Journal of Morphology* **267**:1284-1294.
- Woodward, B. L., J. P. Winn, M. J. Moore, and M. L. Peterson. 2006b. Experimental modeling of large whale entanglement injuries. *Marine Mammal Science* **22**:299-310.
- Zhang, D., J. M. van der Hoop, V. Petrov, J. Rocho-Levine, M. J. Moore, and K. A. Shorter. 2019. Simulated and experimental estimates of hydrodynamic drag from bio-logging tags. *Marine Mammal Science* **36**:136-157.

## **Biography**

Chen-Yi Wu was born in Taiwan. She obtained her dual B.S. in hydraulic and ocean engineering and life science (biology) at the National Cheng Kung University in Tainan, Taiwan in 2015. During her undergraduate study, Chen-Yi learned the applications of fluid mechanics to civil and ecological engineering. In addition, Chen-Yi completed an internship at the Cetacean Laboratory at the National Taiwan University. Her responsibilities include investigating the distribution and population ecology of the Indo-Pacific humpback dolphin (*Sousa chinensis taiwanensis*) in Taiwanese waters, examining the performance of unmanned aerial vehicles (UAVs) in the designed field sites, and writing manuscripts and annual reports on the research projects sponsored by Forestry Bureau of Taiwan.

Recently, she investigated the hydrodynamic properties of the North Atlantic right whales with numerical methods. Her graduate research project provided the baseline estimations of hydrodynamic loads on this species and highlighted the applications of computer solution to marine mammal research. Chen-Yi finished her Ph.D. in marine science and conservation at Duke University, Durham, North Carolina, U.S.A. in 2020.